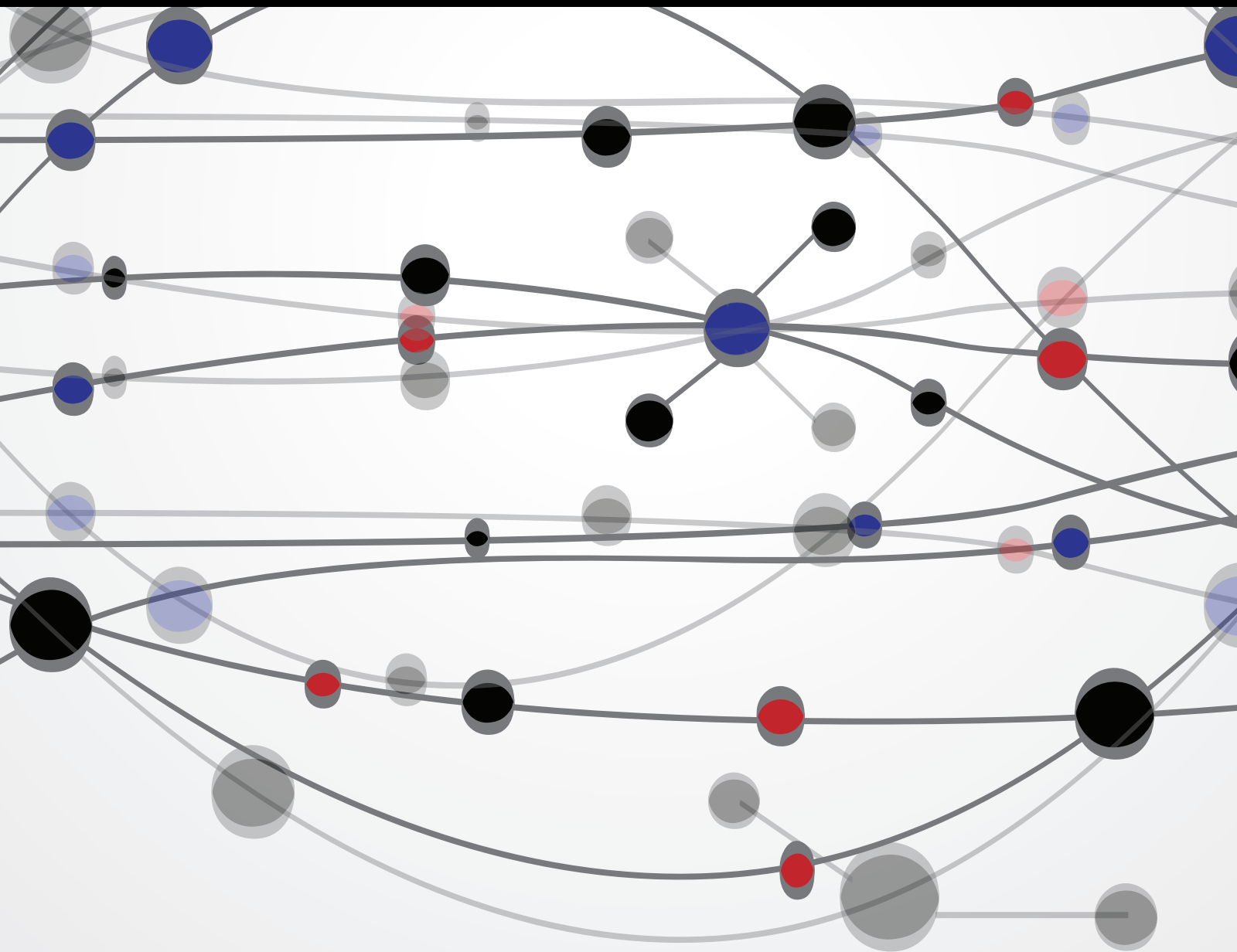


Nanomaterials and Nanodevices

Guest Editors: Xiao-Feng Zhao, Mu-Chun Wang, Jen-Ching Huang,
You Qiang, and In-Seok Yoon





Nanomaterials and Nanodevices

The Scientific World Journal

Nanomaterials and Nanodevices

Guest Editors: Xiao-Feng Zhao, Mu-Chun Wang,
Jen-Ching Huang, You Qiang, and In-Seok Yoon



Copyright © 2015 Hindawi Publishing Corporation. All rights reserved.

This is a special issue published in “The Scientific World Journal.” All articles are open access articles distributed under the Creative Commons Attribution License, which permits unrestricted use, distribution, and reproduction in any medium, provided the original work is properly cited.

Contents

Nanomaterials and Nanodevices, Xiao-Feng Zhao, Mu-Chun Wang, Jen-Ching Huang, You Qiang, and In-Seok Yoon
Volume 2015, Article ID 250401, 2 pages

Nanoparticle Properties and Synthesis Effects on Surface-Enhanced Raman Scattering Enhancement Factor: An Introduction, Nathan D. Israelsen, Cynthia Hanson, and Elizabeth Vargis
Volume 2015, Article ID 124582, 12 pages

Photocatalytic Removal of Microcystin-LR by Advanced WO_3 -Based Nanoparticles under Simulated Solar Light, Chao Zhao, Dawei Li, Yonggang Liu, Chuanping Feng, Zhenya Zhang, Norio Sugiura, and Yingnan Yang
Volume 2015, Article ID 720706, 9 pages

Recent Trends in Rapid Environmental Monitoring of Pathogens and Toxicants: Potential of Nanoparticle-Based Biosensor and Applications, Preeyaporn Koedrith, Thalisa Thasiphu, Jong-Il Weon, Rattana Boonprasert, Kooranee Tuitemwong, and Pravate Tuitemwong
Volume 2015, Article ID 510982, 12 pages

Self-Consolidation Mechanism of Nanostructured Ti_5Si_3 Compact Induced by Electrical Discharge, W. H. Lee, Y. W. Cheon, Y. H. Jo, J. G. Seong, Y. J. Jo, Y. H. Kim, M. S. Noh, H. G. Jeong, C. J. Van Tyne, and S. Y. Chang
Volume 2015, Article ID 815084, 8 pages

Vacuum Ultraviolet Field Emission Lamp Consisting of Neodymium Ion Doped Lutetium Fluoride Thin Film as Phosphor, Masahiro Yanagihara, Takayuki Tsuji, Mohd Zamri Yusop, Masaki Tanemura, Shingo Ono, Tomohito Nagami, Kentaro Fukuda, Toshihisa Suyama, Yuui Yokota, Takayuki Yanagida, and Akira Yoshikawa
Volume 2014, Article ID 309091, 5 pages

Synthesis of Silver Nanoparticles Dispersed in Various Aqueous Media Using Laser Ablation, M. Tajdidzadeh, B. Z. Azmi, W. Mahmood M. Yunus, Z. Abidin Talib, A. R. Sadrollhosseini, K. Karimzadeh, S. A. Gene, and M. Dorraj
Volume 2014, Article ID 324921, 7 pages

Green Nanoparticles for Mosquito Control, Namita Soni and Soam Prakash
Volume 2014, Article ID 496362, 6 pages

Development of a Highly Biocompatible Antituberculosis Nanodelivery Formulation Based on Para-Aminosalicylic Acid—Zinc Layered Hydroxide Nanocomposites, Bullo Saifullah, Palanisamy Arulselvan, Mohamed Ezzat El Zowalaty, Sharida Fakurazi, Thomas J. Webster, Benjamin Geilich, and Mohd Zobir Hussein
Volume 2014, Article ID 401460, 12 pages

Review Article

Nanoparticle Properties and Synthesis Effects on Surface-Enhanced Raman Scattering Enhancement Factor: An Introduction

Nathan D. Israelsen, Cynthia Hanson, and Elizabeth Vargis

Department of Biological Engineering, Utah State University, 4105 Old Main Hill, Logan, UT 84322, USA

Correspondence should be addressed to Elizabeth Vargis; vargis@usu.edu

Received 29 August 2014; Revised 1 November 2014; Accepted 2 November 2014

Academic Editor: Xiao-Feng Zhao

Copyright © 2015 Nathan D. Israelsen et al. This is an open access article distributed under the Creative Commons Attribution License, which permits unrestricted use, distribution, and reproduction in any medium, provided the original work is properly cited.

Raman spectroscopy has enabled researchers to map the specific chemical makeup of surfaces, solutions, and even cells. However, the inherent insensitivity of the technique makes it difficult to use and statistically complicated. When Raman active molecules are near gold or silver nanoparticles, the Raman intensity is significantly amplified. This phenomenon is referred to as surface-enhanced Raman spectroscopy (SERS). The extent of SERS enhancement is due to a variety of factors such as nanoparticle size, shape, material, and configuration. The choice of Raman reporters and protective coatings will also influence SERS enhancement. This review provides an introduction to how these factors influence signal enhancement and how to optimize them during synthesis of SERS nanoparticles.

1. Introduction

Raman spectroscopy is a vibrational spectroscopy technique that has great promise for the identification of solids, liquids, and gases. Similar to infrared (IR) spectroscopy, Raman spectroscopy is a technique used to study molecular vibrations. One advantage that Raman spectroscopy has over traditional IR spectroscopy is that it avoids elaborate sample preparation. Despite this advantage, Raman spectroscopy was not initially as popular as IR spectroscopy due to difficulty in detecting Raman scattering. Statistically, for every 1–10 million photons bombarding a sample, only one will result in Raman scattering [1, 2]. Thanks to technological advances such as mercury lamps, lasers, spectrometers, and charge-coupled devices (CCDs), Raman has gained popularity as a means of chemical identification [3]. Raman continued to gain traction with the aid of signal enhancement methods. In 1974, three scientists from Southampton University (Fleischmann, Hendra, and McQuillan) observed that the Raman spectrum of pyridine on a roughened silver electrode showed unusually large inelastic light scattering [4]. The phenomenon, later termed surface-enhanced Raman spectroscopy (SERS), can enhance the inelastic light scattering events by a factor of 10^6 or more [5]. This enhancement allows researchers to

develop extremely sensitive methods for quantification and identification of small molecules and molecular biomarkers.

Two mechanisms are behind the increased inelastic light scattering seen in SERS, electromagnetic and chemical enhancement. The electromagnetic enhancement is the dominant effect and is due to localized surface plasmon resonance (LSPR). LSPR is an optically excited electron wave resonance state on the surface of a nanostructure, which can increase both elastic (Rayleigh) and inelastic (Raman) light scattering from the sample [6]. The chemical enhancement mechanism is caused by molecular charge-transfer interactions between the molecule and the metallic surface [7, 8]. Together, these mechanisms of enhancement increase the Raman intensity to a point where SERS can be used for applications which require greater molecular sensitivity.

There are two SERS methodologies, intrinsic and extrinsic SERS. Intrinsic SERS involves the direct measurement of the target molecule. In this process, a unique spectrum of the molecular vibration is acquired, which is referred to as a Raman signature. Intrinsic SERS is advantageous in understanding structural information about the target molecule and providing qualitative differences between similar samples. Intrinsic SERS has been used for many biological

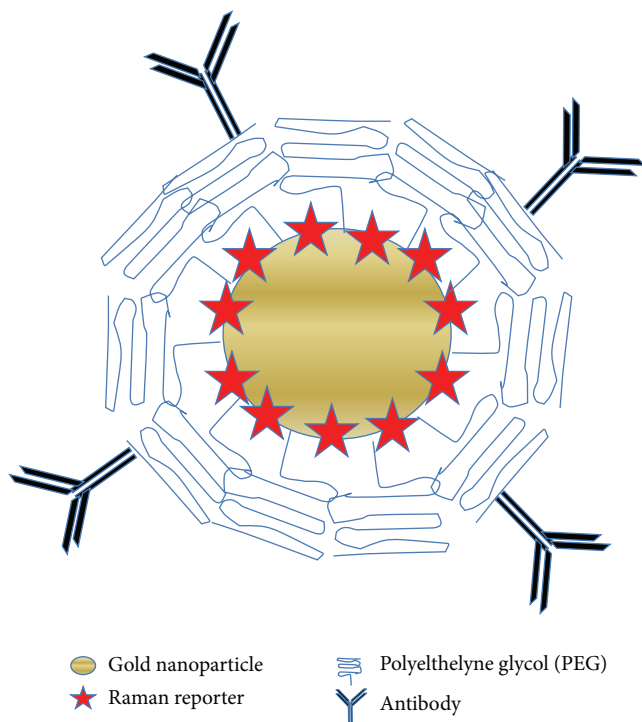


FIGURE 1: An illustration of an extrinsic SERS nanoparticle for targeting of a specific antigen.

applications such as detecting small molecules like glucose [9, 10], antioxidants [11], and amino acids [12]. It has also been used to detect macromolecules such as proteins [13] and DNA [14]. Drawbacks to intrinsic SERS include insensitivities of the molecule to Raman shifts and difficulty in detecting low concentrations. In cases of very dilute samples or where the sample is fairly Raman insensitive, extrinsic SERS provides an alternative mode of detection.

Extrinsic SERS is an indirect method of measuring target molecules because the acquired spectrum is of a Raman reporter rather than the target itself. A Raman reporter is a molecule that has inherently strong Raman active modes. An illustration of a nanoparticle used for extrinsic SERS is provided in Figure 1, where a Raman reporter molecule is bound to the metal surface and encased in a protective layer. This protective layer prevents nanoparticle aggregation and reporter leaching by steric hindrance and charge neutralization. The nanoparticle is then functionalized with an antibody or other ligand to target specific molecular sites. Nanoparticles for extrinsic SERS can be applied in a variety of situations where it is difficult to take intrinsic SERS measurements. For example, nanoparticles used for extrinsic SERS can target specific cell biomarkers [15] and cancer cells [16], while intrinsic SERS applications do not have targeting capabilities. In addition, nanoparticles for extrinsic SERS are synthesized to prevent aggregation in a variety of environments [17]. This trait accommodates *in vivo* measurements. For example, extrinsic SERS has been used to measure *in vivo* liver function [18]. In contrast, nanoparticles used in intrinsic SERS applications are susceptible to aggregation, preventing analysis in certain environments.

Regardless of the SERS method employed, the SERS enhancement factor (EF) is calculated in a variety of ways [19]. However, the simplest and most used definition relies on an estimate of the number of adsorbed reporter molecules and is calculated as follows:

$$EF = \frac{I_{\text{SERS}}/N_{\text{SERS}}}{I_{\text{Normal}}/N_{\text{Normal}}}, \quad (1)$$

where I_{SERS} is the SERS intensity, N_{SERS} is the number of molecules adsorbed to the metal surface in the SERS excitation volume, I_{Normal} is the non-SERS intensity of the solution, and N_{Normal} is the number of molecules in the non-SERS excitation volume. There has been some debate about this formula as it depends on several experimental conditions such as excitation wavelength, molecular species being evaluated, and molecular adsorption properties. Due to variations in these experimental conditions, it is difficult to make an accurate comparison of SERS EFs [19]. EFs are also difficult to compare as there are different types of EF measurements, the maximum EF and the average EF. The maximum EF, although larger, is seldom used in practice because it is difficult to locate SERS hot spots (locations of maximum SERS enhancement). The average SERS EF is the average enhancement for the scattering volume and is more repeatable. Maximum SERS EFs are typically on the order of 10^{10} while average SERS EFs are typically between 10^4 and 10^6 [19].

The lack of a rigorous definition of SERS EF and calculation errors has resulted in SERS EFs which have been reported as high as 10^{14} [5]. For example, in a study on single molecule detection of crystal violet, the SERS intensity of crystal violet is compared to the non-SERS intensity of methanol. This comparison resulted in a high SERS EF which is inaccurate because the author failed to account for the non-SERS intensity of crystal violet [19]. Other sources of error include failing to account for the following parameters: molecule orientation and surface selection rules [20], differentiation between average and maximum EF [21], and photobleaching [22]. In addition, errors can result from inaccurate measurements of metal bound analyte concentration due to shape irregularity and surface roughness [23]. A detailed discussion and rigorous definition of EF has been presented by Le Ru et al., and further details will not be discussed here [19].

The SERS enhancement effect has been observed with alkaline metals [24], various transition and noble metals [24, 25], metals oxides [25] and even semiconductor materials like silicone and graphene [25, 26]. The SERS enhancement of semiconductors is primarily due to chemical mechanisms and is weaker than the enhancement observed with noble metals [25]. Despite the lower enhancement, semiconductors have potential applications in the development of photodetectors and biosensors [27].

Typically, SERS is observed with coinage metals such as gold, silver, and copper due to the large SERS enhancement they produce. Of these metals, silver provides the highest enhancement factor due to its absorption properties. Optical absorption in metals is increased by interband transitions. The interband transition of silver is found in the ultraviolet range. As a result, there will be less absorption in the visible

or near-IR Raman wavelengths resulting in large SERS intensities. In contrast, gold and copper have interband transitions in the visible wavelength range which results in a decrease in the maximum SERS intensity [28, 29]. Despite the greater enhancement capability of silver, gold is often used as it is more stable, is biocompatible, and has an easier surface chemistry than silver [30]. The decision to use gold or silver will depend on several factors such as application, excitation wavelength, LSPR wavelength, and experimental setup.

It has been reported that SERS enhancement is dependent on the distance between the SERS surface and the molecule of interest [31]. Although the target molecule does not need to be touching the surface for SERS enhancement to occur, literature suggests that it needs to be within 1–30 nm for reasonable SERS enhancement [32–34]. The actual distance for SERS enhancement is highly dependent on the nanoparticle surface. Calculations for metallic spherical nanoparticles have predicted that the SERS intensity will decay with increasing distance, r , between the target molecule and particle surface. The distance for electromagnetic enhancement is proportional to r^{-12} . Due to the addition of surface molecules, the decay relationship increases slightly and is proportional to r^{-10} [31, 33].

To effectively optimize nanoparticle EF, the LSPR peak should be taken into account. Initially, it was proposed that the largest amount of Raman scattering should be observed when the particle was excited at its LSPR peak [35]. Experimental studies have found that the optimal excitation wavelength will be slightly blue-shifted from the nanoparticle LSPR peak [36]. One approach to estimating the optimal excitation wavelength for SERS enhancement is to design nanoparticles with an LSPR peak (λ_{LSPR}) between the excitation wavelength (λ_0) and the Raman wavelength of the interest (λ_R). This can be expressed as $\lambda_{\text{LSPR}} = (\lambda_0 + \lambda_R)/2$ [37]. This approach has been validated by a number of independent researchers and appears to apply to many nanostructures investigated [37–39]. However, there are deviations from this rule due to the excitation wavelength used as well as the shape of the nanoparticle [40]. As a general guideline, SERS enhancement has been observed for excitation wavelengths from 600 nm to 1200 nm for gold and from 400 nm to 1000 nm for silver [41].

To synthesize SERS nanoparticles with an optimal EF for intrinsic applications, it is requisite to understand how a nanoparticle's material, size, shape, and configuration influence EFs. Synthesis of nanoparticles for extrinsic SERS applications requires additional understanding of how Raman reporters and protective layers influence EF. This paper provides an introduction to how these factors influence EF (Sections 2 and 3) and how to control them during synthesis (Sections 4 and 5).

2. Enhancement Dependency on Nanoparticle Properties for Intrinsic SERS

2.1. Enhancement Dependency on Nanoparticle Size. Enhancement and LSPR dependency on size is demonstrated in Figure 2, which shows the theoretical (Mie theory) extinction

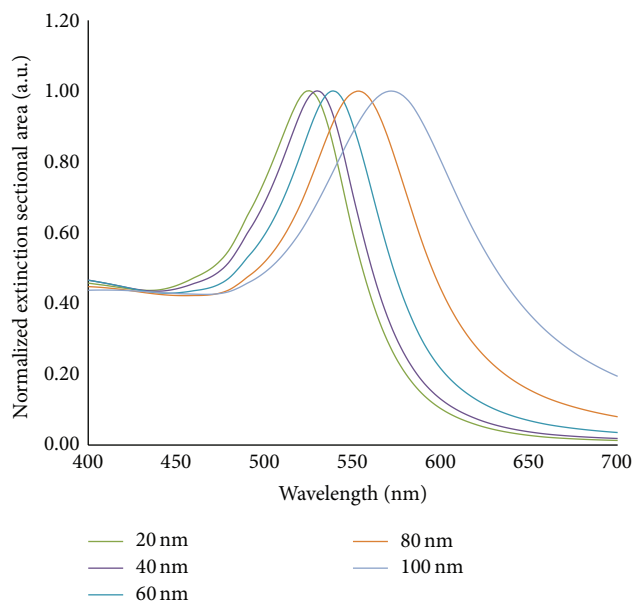


FIGURE 2: Normalized extinction cross-sectional area for spherical gold nanoparticles of diameters ranging from 20–100 nm. Data was obtained from a Mie theory simulation available online [42].

cross section for gold spheres ranging from 20 to 100 nms in diameter. The Mie theory is the solution to the Maxwell equations for how light interacts with a spherical particle. The theory predicts that the smallest spheres have a maximum LSPR at shorter wavelengths. Details concerning the Mie theory can be found in literature and will not be covered here [43, 44]. The relationship between LSPR wavelength and particle size has also been demonstrated experimentally [45–47].

The effect of nanoparticle size on SERS enhancement has been studied by several researchers [48–52]. Previous studies show that spherical gold particles with a 50 nm diameter produced the maximum SERS EF [48, 51]. Others have reported the optimal size particles for SERS enhancement to be in a range from 30 to 100 nm [50, 52]. Regardless of the exact size for optimal enhancement, there is an effective SERS range. When particles are too small, the effective conductivity and light scattering properties, which are needed for SERS enhancement, diminish [50]. As particles increase in size, the SERS effect increases as it depends on the number of electrons available [53]. When the particle size approaches the scale of the excitation wavelength, the particles become preferentially excited in nonradiative modes, leading to a diminished SERS effect [50].

2.2. Enhancement Dependency on Shape. Variations in particle shape can expand the LSPR range. For example, gold nanorods with aspect ratios from 1 to 19 have a LSPR peak range from 508 nm to 2135 nm [54]. Controlling particle shape and size allows researchers to accurately tune nanoparticles for a specific LSPR peak and optimize EF. Shape also influences SERS enhancement due to locations of high curvature such as sharp corners or tips. These locations

produce unusually large electromagnetic enhancement. This enhancement is referred to as the lightning rod effect because similar to a pointed lightning rod, the electric field induced at the tip will be much stronger than other areas on the surface [55]. The influence of the lightning rod effect can be observed near high curvature points on many different shapes [56, 57]. The lightning rod effect allows nanostructures to act as an optical antenna providing an enhanced electromagnetic field [58–60]. More details about the lightning rod effect can be found in literature [61, 62].

2.3. Enhancement Dependency on Material and Configuration. SERS core-shell configurations can be made by coating a nanoparticle with gold or silver. Some common core materials include organic polymers [63–65], silica [66–68], iron oxide (Fe_3O_4) [69, 70], or other metals [71–73]. In core shell configurations, the materials used [73], the overall particle size [74], the shell thickness [75], and the core/shell ratio [74] will influence SERS EF due to shifts in the LSPR peak. For the purpose of this paper, only the influence of core-shell materials and shell thickness on SERS enhancement factor will be covered.

When two metals with different dielectric constants are placed next to each other in a core shell configuration, a LSPR shift will occur. By using the Mie theory, researchers have predicted that increasing the shell thickness of a nanoparticle will shift the LSPR peak to shorter wavelengths [75, 76]. This shift has been confirmed experimentally in a number of cases [75–77]. For example, Oldenburg et al. [75] observed a blue shift in the extinction peak as the gold shell thickness increased over a silica core once the shell was fully formed. The same trend can be seen in nanorods with a core-shell configuration. Ma et al. [76] observed how the LSPR peak shifted to lower wavelengths as the shell thickness increased for silver coated gold nanorods. Not only was there a blue shift, but the intensity also increased according to shell thickness. In the case of silver-gold core-shell arrangements, there will be a red shift as gold has a plasmon resonance peak at a longer wavelength than silver. As the gold shell thickness increases, the absorbance peak also diminishes [78, 79]. In addition to these changes, silver-gold or gold-silver core-shell arrangements create two plasmon resonance peaks [76, 78, 80] corresponding to silver and gold. Changes in LSPR wavelengths can be modified using core-shell nanoparticles by controlling composition materials and shell thickness among other parameters. The LSPR can be tuned to a position to create a maximum enhancement factor by proper placement in relationship to the excitation and emission wavelengths [40].

Another approach to SERS enhancement is due to SERS hot spots. They are locations between particle aggregates which amplify the electromagnetic field near the particle. Researchers have often used nanoparticle junctions or aggregates to create repeatable hot spot locations for single molecule SERS measurements [81–83]. By carefully controlling the placement of the reporter molecule within the particle junction, a maximum SERS EF is observed because hot spot locations are known in advance [84].

TABLE 1: A list of molecules used for SERRS enhancement for excitation wavelengths (λ_0) from 514–785 nm and their associated absorption maximums (λ_{max}).

Raman reporter	λ_{max} (nm)	λ_0 (nm)	Reference
Carboxyfluorescein (FAM)	494	514.5	[85]
Rhodamine 6 G (R6G)	524	514.5, 532	[85–88]
TRITC-DHPE	540	514.5	[89]
Carboxy-X-rhodamine (ROX)	585	514.5, 632.8	[85]
BIODIPY TR-X	588	632.8	[85]
Crystal violet (CV)	590	514.5, 647.1	[86, 90]
Malachite green (MG)	618	632.8	[91]
Malachite green isothiocyanate (MGITC)	625	632.8	[91]
Methylene blue	570–760 [†]	785	[92, 93]
Cy5.5	683	632.8	[85]
3,3'-diethylthiatricarbocyanine iodide (DTTC)	765	785	[94]

[†]Methylene blue (MB) has various different maximum absorption points due to the formation of molecular aggregates and protonation states. The formation of dimer and trimer aggregates and MB protonation causes a shift in the maximum absorption. As a result, the maximum absorption is directly related to the state of the MB molecule during measurement [93].

3. Enhancement Dependency on Nanoparticle Properties for Extrinsic SERS

3.1. Enhancement Dependency on Raman Reporter Properties. Fluorescent dyes and other chromophores are often used as Raman reporters because they have large Raman scattering cross sections, are photostable, and have resonance Raman capabilities. In resonance Raman scattering, the laser excitation wavelength is matched to the reporter molecule's absorption maximum and an approximate 10^3 – 10^6 increase in Raman scattering occurs [95]. By carefully matching the excitation wavelength and nanoparticle composition, surface-enhanced resonance Raman scattering (SERRS) can be observed. SERRS is especially suited for extrinsic measurements if the reporter molecule and excitation wavelengths are known before analysis and can be selected to provide the highest enhancement possible. Table 1 shows molecules that have been used for SERRS studies.

Other characteristics which are important when selecting a Raman reporter molecule are its polarizability, photostability, and binding affinity. Polarizability is the ability of an external electromagnetic field to produce a change in the electron distribution in the molecule. Polarizable molecules have bond configurations which allow an excitation of the vibrational modes of the molecule in response to incident light. A Raman active molecule has a net change in its polarizability when excited by light which causes a shift in the wavelength of the scattered light [96]. Raman reporters should be highly Raman active.

The photostability of a Raman reporter molecule plays an important role in the SERS EF and in determining

the maximum laser power to use. Photobleaching effects can account for SERS EF differences on the order of 10^2 – 10^3 , which is comparable to the EF contribution due to chemical enhancement [97]. Photobleaching effects are related not only to the power of the incident light but also to the actual electromagnetic enhancement experienced by the reporter. As a result, even non-resonant molecules may experience photobleaching [98]. Due to the photobleaching effect, SERS nanoparticles experience a laser power dependent SERS EF. Lower laser power will reduce photobleaching effects and result in more consistent SERS measurements [97]. The use of near IR or IR lasers for excitation will also reduce the photobleaching effect and is recommended for photosensitive reporters [99].

Molecules with strong binding affinities to a gold or silver surface give stronger enhancement due to the chemical enhancement mechanism [91]. High binding affinity molecules that are frequently used are thiol or amine containing molecules because they will easily bind to the gold surface through the gold thiolate bond. Also, positively charged molecules such as crystal violet can associate with the negatively charged nanoparticle surface and are frequently used as Raman reporters [90]. Qian et al. showed how strong binding affinity affects the SERS enhancement factor when using two very similar Raman reporters: malachite green and malachite green isothiocyanate (MGITC) [91]. Although both molecules have similar Raman scattering cross sections and vibrational modes, MGITC showed an approximate 200-fold higher SERS EF under identical measurement conditions. They attributed this EF increase to stable anchoring of the MGITC molecule (by the isothiocyanate group) which enabled charge transfer and chemical enhancement to occur [91].

3.2. Enhancement Dependency on Protective Coating. The SERS protective coating can influence the enhancement effect due to its laser transparency and binding affinity. Coating materials must allow laser light to penetrate the coating and interact with the Raman reporters. Many materials have been used and include polymers [100], silica [101], or proteins [102]. Some coating materials can have an adverse effect on SERS response. For example, Huang et al. [103] observed a 60% decrease in the SERS signal due to the silica coating. Often, (3-mercaptopropyl)trimethoxysilane (MPTMS) is used as a silane functionalizing group because of its ability to bind to the gold surface through a thiolate bond. When the reporter and MPTMS are added simultaneously, the sulfur group binds preferentially, decreasing reporter density and the resulting SERS intensity [104]. This effect highlights the importance of controlling the reporter density on the particle surface as this will have an impact on the SERS enhancement.

4. Controlling Nanoparticle Geometry

The two main approaches for nanoparticle synthesis are the top-down and bottom-up approaches. The top-down approach starts with larger particles and disperses them to smaller particles. The bottom-up approach starts with smaller

particles which build upon each other to form nanoparticles [105]. Top-down approaches typically produce particles in solution that are not as stable or reproducible as those produced from bottom-up approaches [105]. Therefore, this section will focus on bottom-up methods. Some examples of bottom-up approaches include chemical reduction [106–109], sonochemical synthesis [63, 110, 111], photochemical reduction [112], and radiolytic reduction [113]. As this is an introduction to optimal SERS nanoparticle synthesis, the most common chemical reduction methods will be covered.

Chemical reduction methods for synthesis of gold or silver nanoparticles incorporate the use of capping and reducing agents. A capping agent binds to the surface of the nanoparticle and prevents aggregation by repulsive or steric forces. It can also be used to functionalize nanoparticles in extrinsic SERS applications by providing a link to bind the nanoparticle to reporters and antibodies. Some examples include sodium citrate [106], dodecanethiol [107], thiol polyethylene-glycol (PEG) [114], cetrimonium bromide (CTAB) [115], tannic acid [116], hydroxylamine hydrochloride [117], and polyvinylpyrrolidone (PVP) [118]. A reducing agent changes a metal ion in solution to a solid particle. For example, sodium borohydride (NaBH_4) reduces Au^{+3} to solid Au in the Brust-Schiffrin method of gold nanoparticle synthesis [107]. Some common reducing agents used for gold nanoparticle synthesis include sodium citrate [106], NaBH_4 [107], and hydroxylamine [69].

A common chemical reduction method is the Turkevich method. It was introduced in the early 1950s [106] and was a modification of a previous method to synthesize gold nanoparticles by Hauser and Lynn [119]. Although the Turkevich method was introduced over 60 years ago, it is one of the most commonly used methods today and elements of this method can be seen in many techniques to coat particles and surfaces with gold or silver. In this method, sodium citrate is added to a boiling aqueous solution of chloroauric acid (HAuCl_4). Sodium citrate acts as the capping and reducing agent. The Lee-Meisel method [108] uses the same concept to form silver nanoparticles by reducing silver using sodium citrate. The Turkevich and Lee-Meisel methods produce irregularly shaped nanoparticles [120, 121] with diameters ranging from 10 to 150 nm [122] and 60 to 200 nm [120], respectively. It should be noted that several adaptations have been incorporated to these methods to improve control of nanoparticle size and shape [120, 123].

Nanoparticle size is most affected by the strength and concentration of the reducing agent. Stronger reducing agents produce smaller nanoparticles and weaker reducing agents producing larger particles [124]. Sodium citrate is a weak reducing agent, and as such, the Turkevich and Lee-Meisel methods produce relatively large nanoparticles. The Brust-Schiffrin method [107] uses sodium borohydride as a reducing agent, which is much stronger. As a result, this method creates well-dispersed gold nanoparticles ranging from 1 to 3 nm [107].

The size distribution of particles can be refined by controlling the nucleation and growth stages during chemical reduction. In the nucleation process, metal atoms combine to

form clusters and finally crystal nuclei. In the growth step, the crystal nuclei or “seeds” grow in size to form nanoparticles. These steps can be separated for greater control of size and shape and the process is referred to as seed-mediated growth. In these methods, direct synthesis is used to produce the seeds. Consistent seeds are vital to control subsequent nanoparticle shape and size [115, 125, 126]. Several journal articles give further details of seeding methods [115, 120, 125–129] and will not be covered here.

Nanoparticle shape can be controlled by adding surfactants during synthesis which will cause a change in surface energy and control particle aggregation. The surfactant will stabilize specific crystal planes in the growing nanostructure, allowing controlled growth on that plane [130]. By carefully choosing a surfactant and particle material, multiple nanoparticle shapes have been created including nanorods [111, 131], nanocubes [132], nanostars [92, 133], nanotriangles [36, 134], nanoplates [135], nanowires [136], and nanoshells [137–139].

5. Tailoring Nanoparticles for Extrinsic SERS Applications

5.1. Coating Extrinsic Nanoparticles. A common approach for coating Raman reporter encoded gold nanoparticles is to bind a thiol PEG molecule to the gold nanoparticle surface by a gold thiolate bond. For citrate stabilized gold nanoparticles, the thiol group will easily replace the citrate molecule and will provide stabilization [140]. The surface charge of the particles can be controlled by varying the molecular weight of PEG. A simple one-step method to synthesize PEG coated gold nanoparticles has recently been developed [141]. Briefly, it involves heating an aqueous PEG and NaOH solution at 50°C. An aqueous solution of H₂AuCl₄ is then added rapidly while slowly increasing the temperature to 80°C. This method avoids the two-step process of making the gold nanoparticles and then coating with PEG. It also avoids the use of additional chemicals as reduction agents.

The use of a silica shell for coating Raman reporter encoded nanoparticles provides increased stability even in the presence of multiple solvents [142]. To coat the Raman reporter labeled nanoparticles, aminosilanes, such as (3-aminopropyl)triethoxysilane (APTES) or (3-aminopropyl)trimethoxysilane (APTMS), are used to functionalize the particle surface. Tetraethyl orthosilicate (TEOS) or another activated cross-linking agent is used to form the silica shell. TEOS is highly sensitive to water and forms silica dioxide when added to the aminosilane activated gold nanoparticles [143]. Upon formation of the silica shell, these particles are extremely stable and have been used for *in vivo* SERS measurements without loss of the SERS response [16].

5.2. Addition of Antibodies or Other Affinity Ligands. An important factor in the design of extrinsic SERS nanoparticles' is the ability for targeting of specific recognition sites through antibody antigen interactions [15] or DNA hybridization [143]. To bind these ligands to the particle shell,

multiple techniques have been used [138, 143–145]. A common approach is the use of a PEG N-hydroxysuccinimide (NHS) ester for covalent linkage to primary amines in the N terminus or lysine residues. For additional information see [146]. Ligands can be bound to silica coated particles using (3-glycidioxypropyl)methyldiethoxysilane (GPTMS). Li et al. [143] used GPTMS to provide a link between a silica surface and DNA. This binding is due to a highly reactive epoxide group associated with GPTMS. Another approach of surface functionalization involves the addition of a carboxyl group to the surface of the silica shell for further bioconjugation through EDC carbodiimide and NHS chemistry. In this approach, the nanoparticles are first suspended in dimethylformamide (DMF) and then 3-(triethoxysilylpropylcarbonyl)butyric acid is added to the nanoparticles' silica surface. The resulting COOH functionalized silica particles can be used for bioconjugation of oligonucleotides or antibodies [147].

6. Future Applications

6.1. Hybrid Intrinsic/Extrinsic SERS. A potential application of SERS nanoparticles is the development of hybrid nanoparticles. Extrinsic methods generally use Raman reporters and antibodies for indirect sensing of the target molecule, while intrinsic methods directly enhance the target molecules' Raman spectrum. Hybrid applications combine elements of both intrinsic and extrinsic methods. This results in a nanoparticle which can target and enhance the Raman signature of a molecule providing structural information. An approach to develop hybrid SERS nanoparticles is to expose parts of the nanoparticle surface so that it can interact with the target molecule. Kneipp et al. [148] used unprotected nanoparticles with bound reporter molecules to investigate cellular uptake and endosome formation inside various different cells [148–150]. The presence of the reporter molecule enabled multiplexing and specific particle localization. Additionally, the unprotected particle surface allowed the detection of Raman bands related to intracellular components such as lipids, nucleotides, and proteins [149].

A critical factor in the design of hybrid nanoparticles is minimizing the distance between the particle and the target molecule. As mentioned previously, the target molecule must be within approximately 1–30 nm for SERS enhancement to occur. Several researchers have applied different techniques to minimize the distance between the nanoparticle and the target using hybrid SERS applications. For example, Hodges et al., used antibody conjugated gold nanoparticles to bind to specific cell surface regions for targeted SERS enhancement [151]. The large size of the antibody resulted in a large separation between the nanoparticle and the target molecule which limited the SERS enhancement. In order to increase the SERS enhancement, the distance between the metal surface and the target molecule was reduced by using the gold nanoparticles as nucleation centers for silver deposition. The deposited silver allowed for SERS enhancement of only the region around the antibody binding site [151]. Another technique to minimize the distance between the nanoparticle and the target molecule is through the use of antibody

fragments. An antibody fragment is composed of the antigen binding site but does not contain the tail region. As a result the binding capacity is preserved but the total distance occupied by the fragment is less than that of a full antibody. Wang et al. demonstrated that nanoparticles with conjugated antibody fragments can significantly increase the SERS intensity while still maintaining targeting capabilities [152].

7. Summary

The optimization of SERS nanoparticles to achieve the highest enhancement factor is a complex process that incorporates multiple variables which must be precisely controlled by synthesis methods. Nanoparticles for intrinsic SERS applications can be synthesized to control composition, size, shape, and configuration which will affect the LSPR peak location and SERS EF. Smaller particles result in a shorter LSPR wavelength in accordance with the Mie theory. Size can be set during chemical synthesis by proper control of nucleation and growth steps as well as the strength of the reducing agent. Stronger reducing agents will result in smaller particles. Shape will also influence SERS enhancement due to electromagnetic enhancement at edges or sharp corners. Shape can be controlled during synthesis by the addition of surfactants. The proper choice of Raman reporters and protective coatings will determine the enhancement associated with extrinsic SERS. An appropriate Raman reporter will have a strong binding affinity to the nanoparticle surface and allow for resonance Raman enhancement. Care must be taken in the synthesis of the protective layer to prevent loss of the SERS signal. Controlled synthesis of intrinsic and extrinsic SERS nanoparticles can be tuned for specific systems and applications providing optimal SERS enhancement.

Conflict of Interests

The authors declare that there is no conflict of interests regarding the publication of this paper.

Authors' Contribution

Nathan D. Israelsen and Cynthia Hanson contributed equally to this work.

References

- [1] C. L. Zavaleta, M. F. Kircher, and S. S. Gambhir, "Raman's "effect" on molecular imaging," *Journal of Nuclear Medicine*, vol. 52, no. 12, pp. 1839–1844, 2011.
- [2] E. Le Ru and P. G. Etchegoin, "Basic principles," in *Principles of Surface-Enhanced Raman Spectroscopy: And Related Plasmonic Effects*, pp. 7–25, Elsevier Science, Boston, Mass, USA.
- [3] W. H. Nelson and J. F. Sperry, "UV resonance Raman spectroscopic detection and identification of bacteria and other microorganisms," in *Modern Techniques for Rapid Microbiological Analysis*, pp. 97–143, VCH, New York, NY, USA, 1991.
- [4] M. Fleischmann, P. J. Hendra, and A. J. McQuillan, "Raman spectra of pyridine adsorbed at a silver electrode," *Chemical Physics Letters*, vol. 26, no. 2, pp. 163–166, 1974.
- [5] K. Kneipp, Y. Wang, H. Kneipp et al., "Single molecule detection using surface-enhanced Raman scattering (SERS)," *Physical Review Letters*, vol. 78, no. 9, pp. 1667–1670, 1997.
- [6] P. Alonso-González, P. Albella, M. Schnell et al., "Resolving the electromagnetic mechanism of surface-enhanced light scattering at single hot spots," *Nature Communications*, vol. 3, article 684, 2012.
- [7] L. Jensen, C. M. Aikens, and G. C. Schatz, "Electronic structure methods for studying surface-enhanced Raman scattering," *Chemical Society Reviews*, vol. 37, no. 5, pp. 1061–1073, 2008.
- [8] A. Campion, J. E. Ivanecky, C. M. Child, and M. Foster, "On the mechanism of chemical enhancement in surface-enhanced Raman scattering," *Journal of the American Chemical Society*, vol. 117, no. 47, pp. 11807–11808, 1995.
- [9] O. Lyandres, J. M. Yuen, N. C. Shah, R. P. VanDuyne, J. T. Walsh Jr., and M. R. Glucksberg, "Progress toward an in vivo surface-enhanced Raman spectroscopy glucose sensor," *Diabetes Technology and Therapeutics*, vol. 10, no. 4, pp. 257–265, 2008.
- [10] C. R. Yonzon, C. L. Haynes, X. Zhang, J. T. Walsh Jr., and R. P. Van Duyne, "A glucose biosensor based on surface-enhanced Raman scattering: improved partition layer, temporal stability, reversibility, and resistance to serum protein interference," *Analytical Chemistry*, vol. 76, no. 1, pp. 78–85, 2004.
- [11] M. Dendisova-Vyskovska, G. Broncova, M. Clupek, V. Prokopec, and P. Matejka, "In situ SERS spectroelectrochemical analysis of antioxidants deposited on copper substrates: what is the effect of applied potential on sorption behavior?" *Spectrochimica Acta—Part A: Molecular and Biomolecular Spectroscopy*, vol. 99, pp. 196–204, 2012.
- [12] E. Podstawka, Y. Ozaki, and L. M. Proniewicz, "Part III: surface-enhanced Raman scattering of amino acids and their homodipeptide monolayers deposited onto colloidal gold surface," *Applied Spectroscopy*, vol. 59, no. 12, pp. 1516–1526, 2005.
- [13] L.-J. Xu, C. Zong, X.-S. Zheng, P. Hu, J.-M. Feng, and B. Ren, "Label-free detection of native proteins by surface-enhanced Raman spectroscopy using iodide-modified nanoparticles," *Analytical Chemistry*, vol. 86, no. 4, pp. 2238–2245, 2014.
- [14] A. Barhoumi, D. Zhang, F. Tam, and N. J. Halas, "Surface-enhanced Raman spectroscopy of DNA," *Journal of the American Chemical Society*, vol. 130, no. 16, pp. 5523–5529, 2008.
- [15] C. T. Nguyen, J. T. Nguyen, S. Rutledge, J. Zhang, C. Wang, and G. C. Walker, "Detection of chronic lymphocytic leukemia cell surface markers using surface enhanced Raman scattering gold nanoparticles," *Cancer Letters*, vol. 292, no. 1, pp. 91–97, 2010.
- [16] X. Qian, X.-H. Peng, D. O. Ansari et al., "In vivo tumor targeting and spectroscopic detection with surface-enhanced Raman nanoparticle tags," *Nature Biotechnology*, vol. 26, no. 1, pp. 83–90, 2008.
- [17] J. Manson, D. Kumar, B. J. Meenan, and D. Dixon, "Polyethylene glycol functionalized gold nanoparticles: the influence of capping density on stability in various media," *Gold Bulletin*, vol. 44, no. 2, pp. 99–105, 2011.
- [18] C. L. Zavaleta, B. R. Smith, I. Walton et al., "Multiplexed imaging of surface enhanced Raman scattering nanotags in living mice using noninvasive Raman spectroscopy," *Proceedings of the National Academy of Sciences of the United States of America*, vol. 106, no. 32, pp. 13511–13516, 2009.
- [19] E. C. Le Ru, E. Blackie, M. Meyer, and P. G. Etchegoin, "Surface enhanced Raman scattering enhancement factors: a comprehensive study," *The Journal of Physical Chemistry C*, vol. 111, no. 37, pp. 13794–13803, 2007.

- [20] D. V. Chulhai and L. Jensen, "Determining molecular orientation with surface-enhanced Raman scattering using inhomogeneous electric fields," *Journal of Physical Chemistry C*, vol. 117, no. 38, pp. 19622–19631, 2013.
- [21] C. J. Choi, Z. Xu, H.-Y. Wu, G. L. Liu, and B. T. Cunningham, "Surface-enhanced Raman nanodomains," *Nanotechnology*, vol. 21, no. 41, Article ID 415301, 2010.
- [22] P. G. Etchegoin, E. C. Le Ru, R. C. Maher, and L. F. Cohen, "Enhancement factor averaging and the photostability of probes in SERS vibrational pumping," *Physical Chemistry Chemical Physics*, vol. 9, no. 35, pp. 4923–4929, 2007.
- [23] P. H. C. Camargo, L. Au, M. Rycenga, W. Li, and Y. Xia, "Measuring the SERS enhancement factors of dimers with different structures constructed from silver nanocubes," *Chemical Physics Letters*, vol. 484, no. 4–6, pp. 304–308, 2010.
- [24] R. P. Van Duyne, J. C. Hulthen, and D. A. Treichel, "Atomic force microscopy and surface-enhanced Raman spectroscopy. I. Ag island films and Ag film over polymer nanosphere surfaces supported on glass," *Journal of Chemical Physics*, vol. 99, no. 3, pp. 2101–2115, 1993.
- [25] X. Wang, W. Shi, G. She, and L. Mu, "Surface-Enhanced Raman Scattering (SERS) on transition metal and semiconductor nanostructures," *Physical Chemistry Chemical Physics*, vol. 14, no. 17, pp. 5891–5901, 2012.
- [26] Y. B. Wu, Y. F. Wang, and X. W. Cao, "On the enhanced Raman scattering of the nanosized semiconductor: a couple of cylinders (silicon and silver)," *Journal of Applied Physics*, vol. 106, no. 5, Article ID 053106, 2009.
- [27] A. K. Pradhan, R. B. Konda, H. Mustafa et al., "Surface plasmon resonance in CdSe semiconductor coated with gold nanoparticles," *Optics Express*, vol. 16, no. 9, pp. 6202–6208, 2008.
- [28] K. C. See, J. B. Spicer, J. Brupbacher, D. Zhang, and T. G. Vargo, "Modeling interband transitions in silver nanoparticle-fluoropolymer composites," *Journal of Physical Chemistry B*, vol. 109, no. 7, pp. 2693–2698, 2005.
- [29] P. R. West, S. Ishii, G. V. Naik, N. K. Emani, V. M. Shalae, and A. Boltasseva, "Searching for better plasmonic materials," *Laser and Photonics Reviews*, vol. 4, no. 6, pp. 795–808, 2010.
- [30] E. Le Ru and P. Etchegoin, "Appendix E: dielectric function of gold and silver," in *Principles of Surface-Enhanced Raman Spectroscopy: and Related Plasmonic Effects*, pp. 529–535, Elsevier, New York, NY, USA, 2009.
- [31] B. J. Kennedy, S. Spaeth, M. Dickey, and K. T. Carron, "Determination of the distance dependence and experimental effects for modified SERS substrates based on self-assembled monolayers formed using alkanethiols," *The Journal of Physical Chemistry B*, vol. 103, no. 18, pp. 3640–3646, 1999.
- [32] A. K. Singh, S. A. Khan, Z. Fan et al., "Development of a long-range surface-enhanced Raman spectroscopy ruler," *Journal of the American Chemical Society*, vol. 134, no. 20, pp. 8662–8669, 2012.
- [33] J. A. Dieringer, A. D. McFarland, N. C. Shah et al., "Surface enhanced Raman spectroscopy: new materials, concepts, characterization tools, and applications," *Faraday Discussions*, vol. 132, pp. 9–26, 2006.
- [34] V. I. Kukushkin, A. B. Van'kov, and I. V. Kukushkin, "Long-range manifestation of surface-enhanced Raman scattering," *JETP Letters*, vol. 98, no. 2, pp. 64–69, 2013.
- [35] K. Kneipp, M. Moskovits, and H. Kneipp, *Surface-Enhanced Raman Scattering: Physics and Applications*, Springer Science & Business Media, Berlin, Germany, 2006.
- [36] A. D. McFarland, M. A. Young, J. A. Dieringer, and R. P. Van Duyne, "Wavelength-scanned surface-enhanced Raman excitation spectroscopy," *The Journal of Physical Chemistry B*, vol. 109, no. 22, pp. 11279–11285, 2005.
- [37] N. Féliđj, J. Aubard, G. Lévi et al., "Optimized surface-enhanced Raman scattering on gold nanoparticle arrays," *Applied Physics Letters*, vol. 82, no. 18, pp. 3095–3097, 2003.
- [38] C. L. Haynes and R. P. Van Duyne, "Plasmon-sampled surface-enhanced Raman excitation spectroscopy," *Journal of Physical Chemistry B*, vol. 107, no. 30, pp. 7426–7433, 2003.
- [39] J. Grand, M. L. de la Chapelle, J.-L. Bijeon, P.-M. Adam, A. Vial, and P. Royer, "Role of localized surface plasmons in surface-enhanced Raman scattering of shape-controlled metallic particles in regular arrays," *Physical Review B: Condensed Matter and Materials Physics*, vol. 72, no. 3, Article ID 033407, 2005.
- [40] N. Guillot and M. L. de la Chapelle, "The electromagnetic effect in surface enhanced Raman scattering: enhancement optimization using precisely controlled nanostructures," *Journal of Quantitative Spectroscopy and Radiative Transfer*, vol. 113, no. 18, pp. 2321–2333, 2012.
- [41] B. Sharma, R. R. Frontiera, A. I. Henry, E. Ringe, and R. P. Van Duyne, "SERS: materials, applications, and the future," *Materials Today*, vol. 15, no. 1-2, pp. 16–25, 2012.
- [42] NanoComposix, "Tools," NanoComposix, 2014, <http://nanocomposix.com/pages/tools>.
- [43] M. Quinten, *Optical Properties of Nanoparticle Systems: Mie and Beyond*, Wiley-VCH, Weinheim, Germany, 2011.
- [44] E. Le Ru and P. Etchegoin, "Appendix H: Mie theory and its implementation," in *Principles of Surface-Enhanced Raman Spectroscopy: and Related Plasmonic Effects*, pp. 589–628, Elsevier, 2009.
- [45] L. Qiao, D. Wang, L. Zuo et al., "Localized surface plasmon resonance enhanced organic solar cell with gold nanospheres," *Applied Energy*, vol. 88, no. 3, pp. 848–852, 2011.
- [46] T. A. El-Brolosy, T. Abdallah, M. B. Mohamed et al., "Shape and size dependence of the surface plasmon resonance of gold nanoparticles studied by Photoacoustic technique," *The European Physical Journal: Special Topics*, vol. 153, no. 1, pp. 361–364, 2008.
- [47] E. Ringe, J. Zhang, M. R. Langille et al., "Effect of size, shape, composition, and support film on localized surface plasmon resonance frequency: a single particle approach applied to silver bipyramids and gold and silver nanocubes," in *Proceedings of the Materials Research Society Fall Meeting*, vol. 1208, 2010.
- [48] S. Hong and X. Li, "Optimal size of gold nanoparticles for surface-enhanced Raman spectroscopy under different conditions," *Journal of Nanomaterials*, vol. 2013, Article ID 790323, 9 pages, 2013.
- [49] V. Joseph, A. Matschulat, J. Polte, S. Rolf, F. Emmerling, and J. Kneipp, "SERS enhancement of gold nanospheres of defined size," *Journal of Raman Spectroscopy*, vol. 42, no. 9, pp. 1736–1742, 2011.
- [50] M. Moskovits, "Surface-enhanced Raman spectroscopy: a brief retrospective," *Journal of Raman Spectroscopy*, vol. 36, no. 6-7, pp. 485–496, 2005.
- [51] K. G. Stamplecoskie, J. C. Scaiano, V. S. Tiwari, and H. Anis, "Optimal size of silver nanoparticles for surface-enhanced Raman spectroscopy," *Journal of Physical Chemistry C*, vol. 115, no. 5, pp. 1403–1409, 2011.
- [52] P. N. Njoki, I.-I. S. Lim, D. Mott et al., "Size correlation of optical and spectroscopic properties for gold nanoparticles," *The*

- Journal of Physical Chemistry C*, vol. 111, no. 40, pp. 14664–14669, 2007.
- [53] S. Abalde-Cela, P. Aldeanueva-Potel, C. Mateo-Mateo, L. Rodríguez-Lorenzo, R. A. Alvarez-Puebla, and L. M. Liz-Marzán, “Surface-enhanced Raman scattering biomedical applications of plasmonic colloidal particles,” *Journal of the Royal Society Interface*, vol. 7, no. 4, pp. S435–S450, 2010.
- [54] H.-Y. Wu, W.-L. Huang, and M. H. Huang, “Direct high-yield synthesis of high aspect ratio gold nanorods,” *Crystal Growth and Design*, vol. 7, no. 4, pp. 831–835, 2007.
- [55] C. B. Moore, W. Rison, J. Mathis, and G. Aulich, “Lightning rod improvement studies,” *Journal of Applied Meteorology*, vol. 39, no. 5, pp. 593–609, 2000.
- [56] J. Lee, B. Hua, S. Park et al., “Tailoring surface plasmons of high-density gold nanostar assemblies on metal films for surface-enhanced Raman spectroscopy,” *Nanoscale*, vol. 6, no. 1, pp. 616–623, 2014.
- [57] U. Gaware, V. Kamble, and B. Ankamwar, “Ecofriendly synthesis of anisotropic gold nanoparticles: a potential candidate of SERS studies,” *International Journal of Electrochemistry*, vol. 2012, Article ID e276246, 2012.
- [58] P. Halevi, “Chapter 2: surface enhanced Raman scattering,” in *Photonic Probes of Surfaces*, chapter 2, pp. 65–95, Newnes, New South Wales, Australia, 2012.
- [59] J. Li, D. Fattal, and Z. Li, “Plasmonic optical antennas on dielectric gratings with high field enhancement for surface enhanced Raman spectroscopy,” *Applied Physics Letters*, vol. 94, no. 26, Article ID 263114, 2009.
- [60] M. Li, Z. S. Zhang, X. Zhang, K. Y. Li, and X. F. Yu, “Optical properties of Au/Ag core/shell nanoshuttles,” *Optics Express*, vol. 16, no. 18, pp. 14288–14293, 2008.
- [61] E. C. Le Ru, J. Grand, I. Sow et al., “A scheme for detecting every single target molecule with surface-enhanced raman spectroscopy,” *Nano Letters*, vol. 11, no. 11, pp. 5013–5019, 2011.
- [62] A. Ermushev, B. Mchedlishvili, V. Oleinikov, and A. Petukhov, “Surface enhancement of local optical fields and the lightning-rod effect,” *Kvantovaya Elektron*, vol. 20, no. 5, pp. 503–508, 1993.
- [63] V. G. Pol, H. Grisar, and A. Gedanken, “Coating noble metal nanocrystals (Ag, Au, Pd, and Pt) on polystyrene spheres via ultrasound irradiation,” *Langmuir*, vol. 21, no. 8, pp. 3635–3640, 2005.
- [64] A. Dokoutchaev, J. Thomas James, S. C. Koene, S. Pathak, G. K. Surya Prakash, and M. E. Thompson, “Colloidal metal deposition onto functionalized polystyrene microspheres,” *Chemistry of Materials*, vol. 11, no. 9, pp. 2389–2399, 1999.
- [65] Y. Kobayashi, Y. Tadaki, D. Nagao, and M. Konno, “Deposition of gold nanoparticles on polystyrene spheres by electroless metal plating technique,” *Journal of Physics: Conference Series*, vol. 61, no. 1, pp. 582–586, 2007.
- [66] Z. Deng, M. Chen, and L. Wu, “Novel method to fabricate SiO₂/Ag composite spheres and their catalytic, surface-enhanced raman scattering properties,” *The Journal of Physical Chemistry C*, vol. 111, no. 31, pp. 11692–11698, 2007.
- [67] J. H. Kim, W. W. Bryan, and R. T. Lee, “Preparation, characterization, and optical properties of gold, silver, and gold-silver alloy nanoshells having silica cores,” *Langmuir*, vol. 24, no. 19, pp. 11147–11152, 2008.
- [68] Y. T. Lim, O. O. Park, and H.-T. Jung, “Gold nanolayer-encapsulated silica particles synthesized by surface seeding and shell growing method: near infrared responsive materials,” *Journal of Colloid and Interface Science*, vol. 263, no. 2, pp. 449–453, 2003.
- [69] I. Y. Goon, L. M. H. Lai, M. Lim, P. Munroe, J. J. Gooding, and R. Amal, “Fabrication and dispersion of gold-shell-protected magnetite nanoparticles: systematic control using polyethyleneimine,” *Chemistry of Materials*, vol. 21, no. 4, pp. 673–681, 2009.
- [70] L. Zhang, J. Xu, L. Mi, H. Gong, S. Jiang, and Q. Yu, “Multifunctional magnetic-plasmonic nanoparticles for fast concentration and sensitive detection of bacteria using SERS,” *Biosensors and Bioelectronics*, vol. 31, no. 1, pp. 130–136, 2012.
- [71] V. K. Pustovalov and W. Fritzsche, “Nonlinear dependences of optical properties of spherical core-shell silver-gold and gold-silver nanoparticles on their parameters,” *Plasmonics*, vol. 8, no. 2, pp. 983–993, 2013.
- [72] S. Pande, S. K. Ghosh, S. Praharaj et al., “Synthesis of normal and inverted gold-silver core-shell architectures in β -cyclodextrin and their applications in SERS,” *The Journal of Physical Chemistry C*, vol. 111, no. 29, pp. 10806–10813, 2007.
- [73] Z. Y. Li, J. P. Wilcoxon, F. Yin, Y. Chen, R. E. Palmer, and R. L. Johnston, “Structures and optical properties of 4-5 nm bimetallic AgAu nanoparticles,” *Faraday Discussions*, vol. 138, pp. 363–373, 2008.
- [74] P. K. Jain, K. S. Lee, I. H. El-Sayed, and M. A. El-Sayed, “Calculated absorption and scattering properties of gold nanoparticles of different size, shape, and composition: applications in biological imaging and biomedicine,” *Journal of Physical Chemistry B*, vol. 110, no. 14, pp. 7238–7248, 2006.
- [75] S. J. Oldenburg, R. D. Averitt, S. L. Westcott, and N. J. Halas, “Nanoengineering of optical resonances,” *Chemical Physics Letters*, vol. 288, no. 2–4, pp. 243–247, 1998.
- [76] Y. Ma, J. Zhou, W. Zou, Z. Jia, L. Petti, and P. Mormile, “Localized surface plasmon resonance and surface enhanced raman scattering responses of Au@Ag core-shell nanorods with different thickness of Ag shell,” *Journal of Nanoscience and Nanotechnology*, vol. 14, no. 6, pp. 4245–4250, 2014.
- [77] L. Lu, H. Wang, Y. Zhou et al., “Seed-mediated growth of large, monodisperse core-shell gold-silver nanoparticles with Ag-like optical properties,” *Chemical Communications*, no. 2, pp. 144–145, 2002.
- [78] E. Csapo, A. Oszko, E. Varga et al., “Synthesis and characterization of Ag/Au alloy and core(Ag)-shell(Au) nanoparticles,” *Colloids and Surfaces A, Physicochemical and Engineering Aspects*, vol. 415, pp. 281–287, 2012.
- [79] D. Mott, J. Lee, N. T. B. Thuy, Y. Aoki, P. Singh, and S. Maenosono, “A study on the plasmonic properties of silver core gold shell nanoparticles: optical assessment of the particle structure,” *Japanese Journal of Applied Physics*, vol. 50, no. 6, Article ID 065004, 2011.
- [80] L. Lu, G. Burkey, I. Halaciuga, and D. V. Goia, “Core-shell gold/silver nanoparticles: synthesis and optical properties,” *Journal of Colloid and Interface Science*, vol. 392, no. 1, pp. 90–95, 2013.
- [81] H. Liu, L. Zhang, X. Lang et al., “Single molecule detection from a large-scale SERS-active Au 79Ag21 substrate,” *Scientific Reports*, vol. 1, article 112, 2011.
- [82] S. Nie and S. R. Emory, “Probing single molecules and single nanoparticles by surface-enhanced Raman scattering,” *Science*, vol. 275, no. 5303, pp. 1102–1106, 1997.
- [83] H. M. Lee, S. M. Jin, H. M. Kim, and Y. D. Suh, “Single-molecule surface-enhanced Raman spectroscopy: a perspective on the

- current status," *Physical Chemistry Chemical Physics*, vol. 15, no. 15, pp. 5276–5287, 2013.
- [84] D.-K. Lim, K.-S. Jeon, H. M. Kim, J.-M. Nam, and Y. D. Suh, "Nanogap-engineerable raman-active nanodumbbells for single-molecule detection," *Nature Materials*, vol. 9, no. 1, pp. 60–67, 2010.
- [85] K. Faulds, F. McKenzie, W. E. Smith, and D. Graham, "Quantitative simultaneous multianalyte detection of DNA by dual-wavelength surface-enhanced resonance raman scattering," *Angewandte Chemie International Edition*, vol. 46, no. 11, pp. 1829–1831, 2007.
- [86] A. Kudelski, "Raman studies of rhodamine 6G and crystal violet sub-monolayers on electrochemically roughened silver substrates: do dye molecules adsorb preferentially on highly SERS-active sites?" *Chemical Physics Letters*, vol. 414, no. 4–6, pp. 271–275, 2005.
- [87] P. Hildebrandt and M. Stockhurger, "Surface-enhanced resonance Raman spectroscopy of rhodamine 6G adsorbed on colloidal silver," *Journal of Physical Chemistry*, vol. 88, no. 24, pp. 5935–5944, 1984.
- [88] J. A. Dieringer, K. L. Wustholz, D. J. Masiello et al., "Surface-enhanced Raman excitation spectroscopy of a single rhodamine 6G molecule," *Journal of the American Chemical Society*, vol. 131, no. 2, pp. 849–854, 2009.
- [89] N. P. W. Pieczonka, G. Moula, and R. F. Aroca, "SERRS for single-molecule detection of dye-labeled phospholipids in Langmuir-Blodgett monolayers," *Langmuir*, vol. 25, no. 19, pp. 11261–11264, 2009.
- [90] M. V. Cañamares, C. Chenal, R. L. Birke, and J. R. Lombardi, "DFT, SERS, and single-molecule SERS of crystal violet," *Journal of Physical Chemistry C*, vol. 112, no. 51, pp. 20295–20300, 2008.
- [91] X. Qian, S. R. Emory, and S. Nie, "Anchoring molecular chromophores to colloidal gold nanocrystals: surface-enhanced Raman evidence for strong electronic coupling and irreversible structural locking," *Journal of the American Chemical Society*, vol. 134, no. 4, pp. 2000–2003, 2012.
- [92] A. M. Fales, H. Yuan, and T. Vo-Dinh, "Silica-coated gold nanostars for combined surface-enhanced Raman scattering (SERS) detection and singlet-oxygen generation: a potential nanoplatform for theranostics," *Langmuir*, vol. 27, no. 19, pp. 12186–12190, 2011.
- [93] S. H. A. Nicolai and J. C. Rubim, "Surface-enhanced resonance Raman (SERR) spectra of methylene blue adsorbed on a silver electrode," *Langmuir*, vol. 19, no. 10, pp. 4291–4294, 2003.
- [94] H.-X. Cai, Y. Zhang, K.-T. Yong, Z. Shao, Y.-X. Li, and X.-H. Zhang, "Raman spectrum study of 3,3'-diethylthiatri carbocyanine iodide," *Spectroscopy and Spectral Analysis*, vol. 30, no. 12, pp. 3244–3248, 2010.
- [95] E. Smith and G. Dent, "Chapter 4: resonance Raman scattering," in *Modern Raman Spectroscopy—A Practical Approach*, pp. 93–112, John Wiley & Sons, New York, NY, USA, 2005.
- [96] D. A. Long, "Intensities in Raman spectra. I. A bond polarizability theory," *Proceedings of the Royal Society A: Mathematical, Physical and Engineering Sciences*, vol. 217, no. 1129, pp. 203–221, 1953.
- [97] P. G. Etchegoin, P. D. Lacharmoise, and E. C. Le Ru, "Influence of photostability on single-molecule surface enhanced Raman scattering enhancement factors," *Analytical Chemistry*, vol. 81, no. 2, pp. 682–688, 2009.
- [98] Y. Fang, N.-H. Seong, and D. D. Dlott, "Measurement of the distribution of site enhancements in surface-enhanced raman scattering," *Science*, vol. 321, no. 5887, pp. 388–392, 2008.
- [99] N. G. Greeneltch, A. S. Davis, N. A. Valley et al., "Near-infrared surface-enhanced raman spectroscopy (NIR-SERS) for the identification of eosin Y: theoretical calculations and evaluation of two different nanoplasmonic substrates," *The Journal of Physical Chemistry A*, vol. 116, no. 48, pp. 11863–11869, 2012.
- [100] P. Šimáková, J. Gautier, M. Procházka, K. Hervé-Aubert, and I. Chourpa, "Polyethylene-glycol-stabilized ag nanoparticles for surface-enhanced raman scattering spectroscopy: Ag surface accessibility studied using metalation of free-base porphyrins," *Journal of Physical Chemistry C*, vol. 118, no. 14, pp. 7690–7697, 2014.
- [101] W. E. Doering and S. M. Nie, "Spectroscopic tags using dye-embedded nanoparticles and surface-enhanced Raman scattering," *Analytical Chemistry*, vol. 75, no. 22, pp. 6171–6176, 2003.
- [102] X. Su, J. Zhang, L. Sun et al., "Composite Organic-Inorganic Nanoparticles (COINs) with chemically encoded optical signatures," *Nano Letters*, vol. 5, no. 1, pp. 49–54, 2005.
- [103] C.-C. Huang, C.-H. Huang, I.-T. Kuo, L.-K. Chau, and T.-S. Yang, "Synthesis of silica-coated gold nanorod as Raman tags by modulating cetyltrimethylammonium bromide concentration," *Colloids and Surfaces A: Physicochemical and Engineering Aspects*, vol. 409, pp. 61–68, 2012.
- [104] L. Rocks, K. Faulds, and D. Graham, "Rationally designed SERS active silica coated silver nanoparticles," *Chemical Communications*, vol. 47, no. 15, pp. 4415–4417, 2011.
- [105] G. Schmid, "Large clusters and colloids. Metals in the embryonic state," *Chemical Reviews*, vol. 92, no. 8, pp. 1709–1727, 1992.
- [106] J. Turkevich, P. C. Stevenson, and J. Hillier, "A study of the nucleation and growth processes in the synthesis of colloidal gold," *Discussions of the Faraday Society*, vol. 11, pp. 55–75, 1951.
- [107] M. Brust, M. Walker, D. Bethell, D. J. Schiffrin, and R. Whyman, "Synthesis of thiol-derivatised gold nanoparticles in a two-phase liquid-liquid system," *Journal of the Chemical Society, Chemical Communications*, no. 7, pp. 801–802, 1994.
- [108] P. C. Lee and D. Meisel, "Adsorption and surface-enhanced Raman of dyes on silver and gold sols," *Journal of Physical Chemistry*, vol. 86, no. 17, pp. 3391–3395, 1982.
- [109] J. A. Creighton, C. G. Blatchford, and M. G. Albrecht, "Plasma resonance enhancement of Raman scattering by pyridine adsorbed on silver or gold sol particles of size comparable to the excitation wavelength," *Journal of the Chemical Society, Faraday Transactions 2: Molecular and Chemical Physics*, vol. 75, pp. 790–798, 1979.
- [110] R. A. Caruso, M. Ashokkumar, and F. Grieser, "Sonochemical formation of gold sols," *Langmuir*, vol. 18, no. 21, pp. 7831–7836, 2002.
- [111] K. Okitsu, K. Sharyo, and R. Nishimura, "One-pot synthesis of gold nanorods by ultrasonic irradiation: the effect of pH on the shape of the gold nanorods and nanoparticles," *Langmuir*, vol. 25, no. 14, pp. 7786–7790, 2009.
- [112] Y. Liu, L. He, C. Xu, and M. Han, "Photochemical fabrication of hierarchical Ag nanoparticle arrays from domain-selective Ag⁺ loading on block copolymer templates," *Chemical Communications*, no. 43, pp. 6566–6568, 2009.
- [113] L. M. Alrehaily, J. M. Joseph, M. C. Biesinger, D. A. Guzonas, and J. C. Wren, "Gamma-radiolysis-assisted cobalt oxide nanoparticle formation," *Physical Chemistry Chemical Physics*, vol. 15, no. 3, pp. 1014–1024, 2013.
- [114] D. Zopes, B. Stein, S. Mathur, and C. Graf, "Improved stability of "naked" gold nanoparticles enabled by in situ coating with

- mono and multivalent thiol PEG ligands," *Langmuir*, vol. 29, no. 36, pp. 11217–11226, 2013.
- [115] T. K. Sau and C. J. Murphy, "Seeded high yield synthesis of short Au nanorods in aqueous solution," *Langmuir*, vol. 20, no. 15, pp. 6414–6420, 2004.
- [116] S.-Y. Zhao, S.-H. Chen, D.-G. Li, X.-G. Yang, and H.-Y. Ma, "A convenient phase transfer route for Ag nanoparticles," *Physica E: Low-Dimensional Systems and Nanostructures*, vol. 23, no. 1-2, pp. 92–96, 2004.
- [117] N. Leopold and B. Lendl, "A new method for fast preparation of highly surface-enhanced raman scattering (SERS) active silver colloids at room temperature by reduction of silver nitrate with hydroxylamine hydrochloride," *The Journal of Physical Chemistry B*, vol. 107, no. 24, pp. 5723–5727, 2003.
- [118] S. Kittler, C. Greulich, M. Köller, and M. Eppele, "Synthesis of PVP-coated silver nanoparticles and their biological activity towards human mesenchymal stem cells," *Materialwissenschaft und Werkstofftechnik*, vol. 40, no. 4, pp. 258–264, 2009.
- [119] E. A. Hauser and J. E. Lynn, *Experiments in Colloid Chemistry*, McGraw-Hill, 1940.
- [120] Y. Wan, Z. Guo, X. Jiang et al., "Quasi-spherical silver nanoparticles: aqueous synthesis and size control by the seed-mediated Lee-Meisel method," *Journal of Colloid and Interface Science*, vol. 394, no. 1, pp. 263–268, 2013.
- [121] J. Kimling, M. Maier, B. Okenve, V. Kotaidis, H. Ballot, and A. Plech, "Turkevich method for gold nanoparticle synthesis revisited," *Journal of Physical Chemistry B*, vol. 110, no. 32, pp. 15700–15707, 2006.
- [122] E. A. Vitol, G. Friedman, and Y. Gogotsi, "Surface-enhanced raman spectroscopy-active substrates: adapting the shape of plasmonic nanoparticles for different biological applications," *Journal of Nanoscience and Nanotechnology*, vol. 14, no. 4, pp. 3046–3051, 2014.
- [123] X. Dong, X. Ji, H. Wu, L. Zhao, J. Li, and W. Yang, "Shape control of silver nanoparticles by stepwise citrate reduction," *The Journal of Physical Chemistry C*, vol. 113, no. 16, pp. 6573–6576, 2009.
- [124] G. T. Hermanson, "Preparation of colloidal gold-labeled proteins," in *Bioconjugate Techniques*, chapter 24, pp. 924–935, Elsevier, New York, NY, USA, 2nd edition, 2008.
- [125] W. Niu, L. Zhang, and G. Xu, "Seed-mediated growth of noble metal nanocrystals: crystal growth and shape control," *Nanoscale*, vol. 5, no. 8, pp. 3172–3181, 2013.
- [126] A. K. Samal, T. S. Sreeprasad, and T. Pradeep, "Investigation of the role of NaBH₄ in the chemical synthesis of gold nanorods," *Journal of Nanoparticle Research*, vol. 12, no. 5, pp. 1777–1786, 2010.
- [127] N. R. Jana, L. Gearheart, and C. J. Murphy, "Evidence for seed-mediated nucleation in the chemical reduction of gold salts to gold nanoparticles," *Chemistry of Materials*, vol. 13, no. 7, pp. 2313–2322, 2001.
- [128] N. R. Jana, L. Gearheart, and C. J. Murphy, "Seeding growth for size control of 5–40 nm diameter gold nanoparticles," *Langmuir*, vol. 17, no. 22, pp. 6782–6786, 2001.
- [129] S. Kumar, H. Yang, and S. Zou, "Seed-mediated growth of uniform gold nanoparticle arrays," *Journal of Physical Chemistry C*, vol. 111, no. 35, pp. 12933–12938, 2007.
- [130] H. You, S. Yang, B. Ding, and H. Yang, "Synthesis of colloidal metal and metal alloy nanoparticles for electrochemical energy applications," *Chemical Society Reviews*, vol. 42, no. 7, pp. 2880–2904, 2013.
- [131] C. J. Orendorff, L. Gearheart, N. R. Jana, and C. J. Murphy, "Aspect ratio dependence on surface enhanced Raman scattering using silver and gold nanorod substrates," *Physical Chemistry Chemical Physics*, vol. 8, no. 1, pp. 165–170, 2006.
- [132] S. Y. Lee, L. Hung, G. S. Lang, J. E. Cornett, I. D. Mayergoyz, and O. Rabin, "Dispersion in the SERS enhancement with silver nanocube dimers," *ACS Nano*, vol. 4, no. 10, pp. 5763–5772, 2010.
- [133] C. G. Khoury and T. Vo-Dinh, "Gold nanostars for surface-enhanced Raman scattering: synthesis, characterization and optimization," *The Journal of Physical Chemistry C*, vol. 112, no. 48, pp. 18849–18859, 2008.
- [134] D. Correia-Ledo, K. F. Gibson, A. Dhawan et al., "Assessing the location of surface plasmons over nanotriangle and nanohole arrays of different size and periodicity," *Journal of Physical Chemistry C*, vol. 116, no. 12, pp. 6884–6892, 2012.
- [135] T. Tan, C. Tian, Z. Ren et al., "LSPR-dependent SERS performance of silver nanoplates with highly stable and broad tunable LSPRs prepared through an improved seed-mediated strategy," *Physical Chemistry Chemical Physics*, vol. 15, no. 48, pp. 21034–21042, 2013.
- [136] H. Wang, X. Han, X. Ou, C.-S. Lee, X. Zhang, and S.-T. Lee, "Silicon nanowire based single-molecule SERS sensor," *Nanoscale*, vol. 5, no. 17, pp. 8172–8176, 2013.
- [137] L. R. Bickford, G. Agollah, R. Drezek, and T.-K. Yu, "Silica-gold nanoshells as potential intraoperative molecular probes for HER2-overexpression in ex vivo breast tissue using near-infrared reflectance confocal microscopy," *Breast Cancer Research and Treatment*, vol. 120, no. 3, pp. 547–555, 2010.
- [138] L. R. Hirsch, J. B. Jackson, A. Lee, N. J. Halas, and J. L. West, "A whole blood immunoassay using gold nanoshells," *Analytical Chemistry*, vol. 75, no. 10, pp. 2377–2381, 2003.
- [139] J. Song, B. Duan, C. Wang et al., "SERS-encoded nanogapped plasmonic nanoparticles: growth of metallic nanoshell by templating redox-active polymer brushes," *Journal of the American Chemical Society*, vol. 136, no. 19, pp. 6838–6841, 2014.
- [140] G. H. Woehrle, L. O. Brown, and J. E. Hutchison, "Thiol-functionalized, 1.5-nm gold nanoparticles through ligand exchange reactions: scope and mechanism of ligand exchange," *Journal of the American Chemical Society*, vol. 127, no. 7, pp. 2172–2183, 2005.
- [141] R. Stiufluic, C. Iacovita, R. Nicoara et al., "One-step synthesis of PEGylated gold nanoparticles with tunable surface charge," *Journal of Nanomaterials*, vol. 2013, Article ID 146031, 7 pages, 2013.
- [142] S. P. Mulvaney, M. D. Musick, C. D. Keating, and M. J. Natan, "Glass-coated, analyte-tagged nanoparticles: a new tagging system based on detection with surface-enhanced Raman scattering," *Langmuir*, vol. 19, no. 11, pp. 4784–4790, 2003.
- [143] J.-M. Li, C. Wei, W.-F. Ma et al., "Multiplexed SERS detection of DNA targets in a sandwich-hybridization assay using SERS-encoded core-shell nanospheres," *Journal of Materials Chemistry*, vol. 22, no. 24, pp. 12100–12106, 2012.
- [144] C. M. Copley, L. Au, J. Chen, and Y. Xia, "Targeting gold nanocages to cancer cells for photothermal destruction and drug delivery," *Expert Opinion on Drug Delivery*, vol. 7, no. 5, pp. 577–587, 2010.
- [145] A. Weiss, T. C. Preston, J. Popov et al., "Selective recognition of rituximab-functionalized gold nanoparticles by lymphoma cells studied with 3D imaging," *Journal of Physical Chemistry C*, vol. 113, no. 47, pp. 20252–20258, 2009.
- [146] G. T. Hermanson, *Bioconjugate Techniques*, Academic Press, 2010.

- [147] L. Levy, Y. Sahoo, K.-S. Kim, E. J. Bergey, and P. N. Prasad, "Nanochemistry: synthesis and characterization of multifunctional nanoclusters for biological applications," *Chemistry of Materials*, vol. 14, no. 9, pp. 3715–3721, 2002.
- [148] J. Kneipp, H. Kneipp, A. Rajadurai, R. W. Redmond, and K. Kneipp, "Optical probing and imaging of live cells using SERS labels," *Journal of Raman Spectroscopy*, vol. 40, no. 1, pp. 1–5, 2009.
- [149] A. Hornemann, D. Drescher, S. Flemig, and J. Kneipp, "Intracellular SERS hybrid probes using BSA—reporter conjugates," *Analytical and Bioanalytical Chemistry*, vol. 405, no. 19, pp. 6209–6222, 2013.
- [150] G. L. Liu, F. F. Chen, J. A. Ellman, and L. P. Lee, "Peptide-nanoparticle hybrid SERS probe for dynamic detection of active cancer biomarker enzymes," *Conference Proceedings: Annual International Conference of the IEEE Engineering in Medicine and Biology Society*, vol. 1, pp. 795–798, 2006.
- [151] M. D. Hodges, J. G. Kelly, A. J. Bentley et al., "Combining immunolabeling and surface-enhanced Raman spectroscopy on cell membranes," *ACS Nano*, vol. 5, no. 12, pp. 9535–9541, 2011.
- [152] Y. Wang, L.-J. Tang, and J.-H. Jiang, "Surface-enhanced Raman spectroscopy-based, homogeneous, multiplexed immunoassay with antibody-fragments-decorated gold nanoparticles," *Analytical Chemistry*, vol. 85, no. 19, pp. 9213–9220, 2013.

Research Article

Photocatalytic Removal of Microcystin-LR by Advanced WO₃-Based Nanoparticles under Simulated Solar Light

Chao Zhao,^{1,2} Dawei Li,¹ Yonggang Liu,³ Chuanping Feng,² Zhenya Zhang,¹ Norio Sugiura,¹ and Yingnan Yang¹

¹Graduate School of Life and Environmental Sciences, University of Tsukuba, Tsukuba 305-8572, Japan

²School of Water Resources and Environment, China University of Geosciences, Beijing 100083, China

³Institute of Environmental Sciences, Zhengzhou University, Zhengzhou 450001, China

Correspondence should be addressed to Yingnan Yang; yangjiayangjp@yahoo.co.jp

Received 1 July 2014; Revised 1 September 2014; Accepted 1 September 2014

Academic Editor: Xiao-Feng Zhao

Copyright © 2015 Chao Zhao et al. This is an open access article distributed under the Creative Commons Attribution License, which permits unrestricted use, distribution, and reproduction in any medium, provided the original work is properly cited.

A series of advanced WO₃-based photocatalysts including CuO/WO₃, Pd/WO₃, and Pt/WO₃ were synthesized for the photocatalytic removal of microcystin-LR (MC-LR) under simulated solar light. In the present study, Pt/WO₃ exhibited the best performance for the photocatalytic degradation of MC-LR. The MC-LR degradation can be described by pseudo-first-order kinetic model. Chloride ion (Cl⁻) with proper concentration could enhance the MC-LR degradation. The presence of metal cations (Cu²⁺ and Fe³⁺) improved the photocatalytic degradation of MC-LR. This study suggests that Pt/WO₃ photocatalytic oxidation under solar light is a promising option for the purification of water containing MC-LR.

1. Introduction

Eutrophication in superficial freshwater bodies induced frequent cyanobacteria blooms worldwide. The occurrence of toxic cyanobacterial blooms in eutrophic lakes, reservoirs, and other recreational water has been identified as an increasingly serious problem in many countries [1]. The toxins released into freshwater by cyanobacteria are well documented [2].

Microcystins (MCs) are the most commonly occurring toxins released by cyanobacteria. MCs are cyclic heptapeptides containing the unique C₂₀ amino acid, 3-amino-9-methoxy-2,6,8-trimethyl-10-phenyldeca-4,6-dienoic acid (ADDA). MCs are strongly hepatotoxic because they inhibit serine/threonine protein phosphatases 1 and 2A [3]. Acute exposure may result in hepatic injury, promote primary liver cancer, and even cause the death of animals and humans. One of the most common occurring MCs is the highly toxic microcystin-LR (MC-LR), which has leucine (L) and arginine (R) in the variable positions. The World Health

Organization (WHO) has determined a provisional guideline value of 1.0 μg L⁻¹ for MC-LR in drinking water. Various water treatment processes have been evaluated to determine their performance in decomposing these toxins. However, MCs are chemically stable across a range of pH values and temperatures, due to their cyclic structure. Consequently, traditional water treatment processes are not reliable for the removal of MCs [4–6].

Photocatalytic oxidation as an advanced oxidation technology has been considered an environment-friendly water treatment method [7–11]. When the photocatalyst exposure to a light with appropriate wavelength happens, electron (e⁻) and hole (h⁺) pairs are generated on the catalyst surface. The photogenerated electrons and holes react with oxygen and water molecules or hydroxyl groups adsorbed on photocatalyst surface to form highly reactive species, such as superoxide radicals (•O₂⁻) and hydroxyl radicals (•OH) [12]. These radicals can oxidize a number of organic pollutants including dyes, pesticides, and herbicides [7–11, 13]. Previous research proved that photocatalytic oxidation with TiO₂ photocatalyst

could effectively destroy MCs, even at extremely high toxin concentrations [14, 15]. However, TiO_2 has a large band gap energy (E_g) of 3.2 eV that restricts the wide use of this photocatalyst, because it can only absorb UV light which accounts for 5% of the solar light [16]. Many efforts have been made to enhance the photocatalytic performance of TiO_2 under solar light. For example, Ag-modified TiO_2 thin film was developed for bacteria disinfection under solar light [17, 18]. TiO_2 -film/ CuO microgrid heterojunction and P-doped TiO_2 nanoparticles were synthesized for the decomposition of organic dye [19, 20]. By contrast, tungsten trioxide (WO_3) can utilize solar light more effectively than TiO_2 , because it has an E_g between 2.4 and 2.8 eV [10]. In addition, WO_3 is inexpensive to prepare and stable in acidic and oxidative conditions, which makes it a promising material for photocatalytic applications. Previous research showed that photocatalytic degradation of organic pollutants such as organic dyes using WO_3 under solar light was intensified by the presence of suitable dopants, such as Pt, Pd, and CuO [21–23]. However, there is little research on the photocatalytic degradation of MCs using WO_3 -based photocatalysts under solar light.

In the present study, three types of WO_3 -based photocatalysts including CuO/WO_3 , Pd/WO_3 , and Pt/WO_3 were synthesized for photocatalytic degradation of MC-LR under simulated solar light. The characteristics of developed WO_3 -based photocatalysts were analyzed by BET surface area, X-ray diffraction (XRD), and scanning electron microscopy (SEM). A series of batch experiments were carried out to evaluate the photocatalytic performance of the developed photocatalysts for MC-LR degradation under simulated solar light. On the other hand, chlorides and metal cations are common in water, and they are important in many treatment technologies such as breakpoint chlorination and electrochemical oxidation methods [24]. Therefore, in this study, the effects of chloride ions (Cl^-) and metal cations (Cu^{2+} and Fe^{3+}) on the photocatalytic degradation of MC-LR under solar light were also investigated.

2. Experimental

2.1. Reagents. WO_3 powder, microcystin-LR (MC-LR) standard ($\geq 95\%$ purity; FW 995.2 g mol^{-1}), terephthalic acid 99%, and $\text{Cu}(\text{NO}_3)_2 \cdot 3\text{H}_2\text{O}$ (99.9% purity) were purchased from Wako (Wako Pure Chemical Industries, Ltd., Japan). Hexachloroplatinic acid ($\text{H}_2\text{PtCl}_6 \cdot 6\text{H}_2\text{O}$) and Pd powder with a surface area of 40–60 $\text{m}^2 \text{g}^{-1}$ were supplied by Sigma-Aldrich (Sigma-Aldrich Co. LLC., USA).

2.2. Photocatalyst Preparation. The WO_3 loaded with 0.1 wt% CuO (marked as CuO/WO_3) was synthesized by an impregnation method [21]: $\text{Cu}(\text{NO}_3)_2$ aqueous solution was mixed with WO_3 powder, and the mixture was dried on hot plate and then calcined at 300 °C for 30 min in air.

The Pd doped WO_3 photocatalyst (Pd/WO_3) was prepared by the mechanical mixing of Pd (wt% versus WO_3) and WO_3 in a ceramic mortar [25].

The Pt modified WO_3 sample (Pt/WO_3) was developed using a photodeposition method [21] from $\text{H}_2\text{PtCl}_6 \cdot 6\text{H}_2\text{O}$

on the fine particulate WO_3 under visible light irradiation in pure water and subsequently in an aqueous methanol (10 vol.%) solution.

2.3. Photocatalyst Characterization. The crystalline phases of the prepared photocatalysts were determined using a powder X-ray diffraction (XRD) (Rigaku RINT2200, Japan). The morphology of the prepared photocatalysts was analyzed by a scanning electron microscopy (SEM) (JEOL, JSM-5600, Japan). The specific surface area of the prepared photocatalyst was measured using a BET surface area analyzer (Coulter SA3100, USA).

2.4. Photocatalytic Removal of MC-LR. The photocatalytic degradation of MC-LR by prepared WO_3 -based photocatalyst was performed in a 6 mL glass vessel placed on a magnetic stirrer. A simulated solar lamp (XC-100B, SERIC Ltd., Japan) equipped axially at the center region above the glass vessel was employed as the irradiation source. In the present experiments, pure WO_3 and the developed three types of WO_3 -based photocatalysts (CuO/WO_3 , Pd/WO_3 , and Pt/WO_3) were previously dispersed in water using an ultrasonic bath sonicator for 30 min. Then the photocatalysts dispersed solutions were transferred to the glass vessels containing MC-LR to obtain a final volume of 5 mL. The initial MC-LR concentration in each glass vessel was 1 mg L^{-1} . Before irradiation, the suspension was magnetically stirred for 60 min in the dark to achieve adsorption equilibrium. After that, the lamp was switched on to initiate the photocatalytic reaction. Temperature of the whole laboratory was controlled at $25 \pm 1^\circ\text{C}$ by an air conditioner. In addition, a mini-air-circulator was also employed near to the reactor to make sure constant local temperature during the photocatalytic reaction exists. During irradiation, 0.25 mL of sample was withdrawn at a time interval of 30 min, centrifuged at 10000 rpm for 10 min, and filtered through a 0.22 μm filter membrane before the HPLC analysis.

The concentration of MC-LR was measured using a high performance liquid chromatography (HPLC) (Jasco-1500, Jasco, Japan) equipped with a high-resolution diode array detector (Jasco UV-1570) set at 238 nm. Samples were separated on a C18 column (4.6 \times 250 mm, 5 μm) using a mixture of acetonitrile and 0.05 M phosphate buffer (pH 6.8; 32 : 68 v/v) as the mobile phase at a flow rate of 1 mL min^{-1} . All the experiments were replicated three times under the same conditions and the average value was used for analyses.

2.5. Detection of Hydroxyl Radicals ($\bullet\text{OH}$). The detection of hydroxyl radicals generated by the prepared WO_3 -based photocatalysts was carried out according to Ishibashi et al. [26]. Terephthalic acid was used as a probe molecule to detect the photogenerated $\bullet\text{OH}$ radicals in the photocatalytic reaction system. A sample of 4 mg developed WO_3 -based photocatalyst powder was dispersed in a 20 mL solution made of terephthalic acid at 5×10^{-4} M dissolved in a 2×10^{-3} M NaOH aqueous solution. The simulated solar light was used as an irradiation source. During the irradiation, samples were withdrawn and centrifuged at a 20 min time interval. Then,

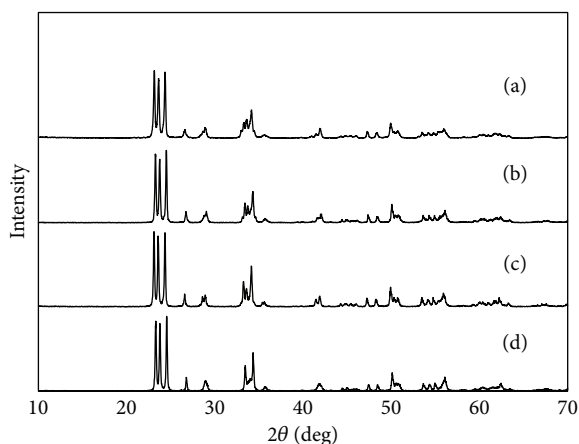


FIGURE 1: XRD patterns of WO_3 and modified WO_3 samples: (a) Pd/ WO_3 , (b) Pt/ WO_3 , (c) CuO/ WO_3 , and (d) pure WO_3 .

the centrifuged solution was transferred in a quartz cell and the photoluminescence spectra of 2-hydroxyterephthalic acid generated by the reaction of terephthalic acid with $\bullet\text{OH}$ were measured on a Hitachi F-4500 fluorescence spectrophotometer. The spectra were recorded between 350 and 550 nm under an excitation at 315 nm.

3. Results and Discussion

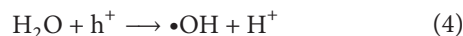
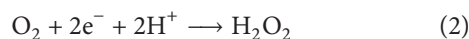
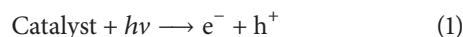
3.1. Characterization of WO_3 -Based Photocatalysts. The crystalline phases of the developed WO_3 -based photocatalysts were measured by a powder X-ray diffraction (XRD) (Rigaku RINT2200, Japan). Characteristic peaks are observed for all diffraction patterns, which are indexed to the standard card (JCPDS 43-1035). As shown in Figure 1, all samples have monoclinic WO_3 structure and the metal doping does not influence the crystal structures of WO_3 . No extra peaks except for monoclinic WO_3 are observed (Figure 1). This phenomenon can be explained by the small amount of CuO, Pd, and Pt species content and high dispersion in the samples.

The morphology and microstructure of the developed photocatalysts were analyzed by scanning electron microscopy (SEM) (Figure 2). The SEM images of pure and modified WO_3 photocatalysts showed that they are composed of particles with size ranging from 100 to 200 nm. The specific surface area of the pure WO_3 was about $5 \text{ m}^2 \text{ g}^{-1}$ which is in agreement with other reports [22]. The specific surface area of modified WO_3 photocatalysts (CuO/ WO_3 , Pd/ WO_3 , and Pt/ WO_3) was slightly increased to 6.0, 6.5, and $7.0 \text{ m}^2 \text{ g}^{-1}$, respectively, due to the metals loading and a grind of WO_3 powders in the preparation process.

3.2. Photocatalytic Removal of MC-LR Using Various WO_3 -Based Photocatalysts. As shown in Figure 3, the concentration of MC-LR was virtually unchanged after 180 min solar light irradiation when there was no photocatalyst in the solution. This result indicated that MC-LR was stable under solar

light irradiation. After 180 min photocatalysis, approximately 24.8% of MC-LR was removed from the aqueous solution in which only pure WO_3 was added. The modified WO_3 -based photocatalysts (CuO/ WO_3 and Pd/ WO_3) achieved 31.4% and 42.9% MC-LR removal, respectively. The Pt/ WO_3 composite achieved a 100% degradation of MC-LR after 180 min solar light irradiation. The modified WO_3 -based photocatalysts are supported by many previous researches. Arai et al. reported that the photocatalytic activity of Pd/ WO_3 was 2 times higher than that of CuO/ WO_3 in the degradation of acetaldehyde, and the performance of Pt/ WO_3 was better than that of CuO/ WO_3 for decomposing formaldehyde [22, 23]. In this present study, Pt/ WO_3 exhibits the best photocatalytic performance for the degradation of MC-LR under solar light irradiation.

3.3. The Mechanism of MC-LR Degradation by WO_3 -Based Photocatalysts. The relative more positive conduction band level of WO_3 (+0.5 V versus NHE) compared to potential for the single-electron reduction of oxygen ($\text{O}_2/\text{O}_2^- = -0.56 \text{ V}$ versus NHE; $\text{O}_2/\text{HO}_2 = -0.13 \text{ V}$ versus NHE) was the main reason for the relative slow reaction rate of WO_3 -induced photocatalytic reactions. In the presence of CuO, Pd, and Pt, the reduction of O_2 molecules can be promoted effectively by a multielectron process ($\text{O}_2/\text{H}_2\text{O}_2 = +0.68 \text{ V}$ versus NHE; $\text{O}_2/\text{H}_2\text{O} = +1.23 \text{ V}$ versus NHE) [22, 27]. In a photocatalytic reaction, the following chain reactions have been postulated:



Photocatalytic degradation of MC-LR was initiated by the attack of hydroxyl radical ($\bullet\text{OH}$) on the conjugated diene structure of ADDA [28], indicating the primary reactive species in MC-LR degradation is $\bullet\text{OH}$ radical. The photogenerated $\bullet\text{OH}$ radicals can be detected by photoluminescence spectra analysis. Figure 4 shows the photoluminescent spectral changes of Pt/ WO_3 during 60 min solar light irradiation. At the wavelength of 425 nm, the photoluminescence intensity gradually increased from 2.5 to 43.8 a.u with increasing the irradiation time to 60 min, indicating that $\bullet\text{OH}$ radicals were generated on the photocatalyst-water interface via photocatalytic reactions [26, 27].

Figure 5 presents the photoluminescence intensity of pure WO_3 and modified WO_3 -based photocatalysts at 425 nm as a function of irradiation time. The photoluminescence intensity induced by simulated solar light in terephthalic acid solution was linearly related to the irradiation time. The number of $\bullet\text{OH}$ radicals generated on the surface of these photocatalysts was proportional to the irradiation time and followed zero-order kinetic model [26, 28]. Furthermore, the slopes of the regression lines represent the generation rate of $\bullet\text{OH}$ radicals (Figure 5). Without a dopant, WO_3 could

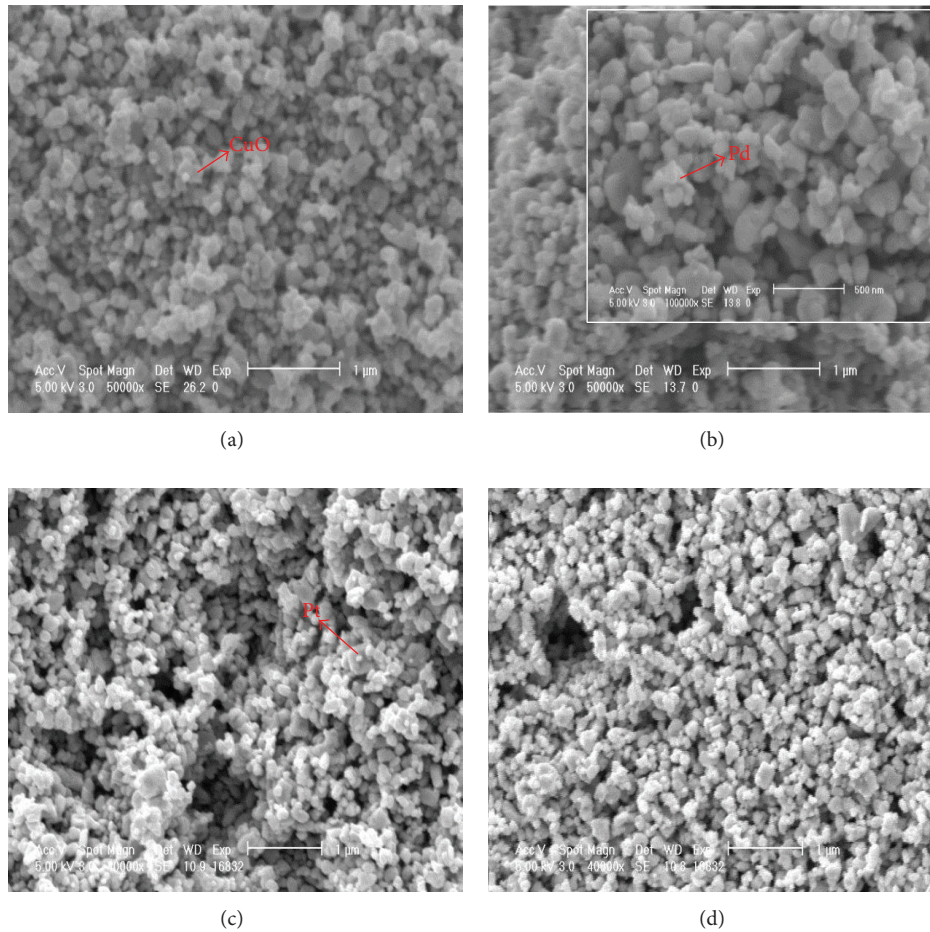


FIGURE 2: SEM images of WO_3 and modified WO_3 samples: (a) CuO/WO_3 , (b) Pd/WO_3 , (c) Pt/WO_3 , and (d) pure WO_3 .

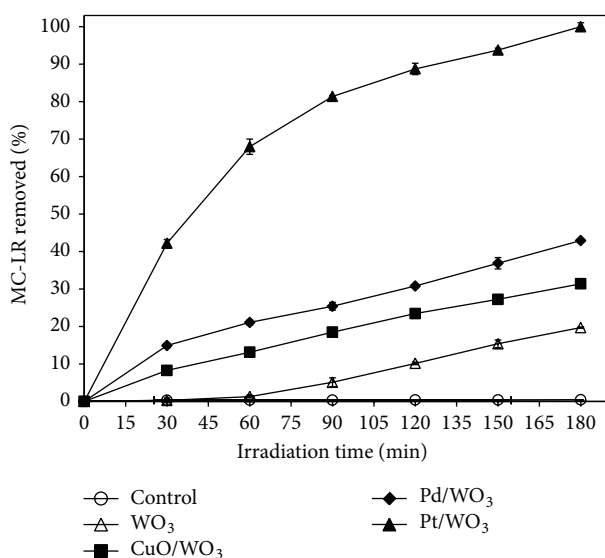


FIGURE 3: The effect of catalysts on the efficiency of photocatalytic degradation of MC-LR. (Experimental conditions: MC-LR concentration of 1 mg L^{-1} , catalyst concentration of 100 mg L^{-1} , and simulated solar light intensity of 0.4 mW cm^{-2} .)

only generate a small number of $\bullet\text{OH}$ radicals under solar light irradiation. The generation rate of $\bullet\text{OH}$ radicals on the surface of pure WO_3 is merely $0.04 \text{ a.u min}^{-1}$. When doped with CuO , Pd , and Pt , the generation rate of $\bullet\text{OH}$ radicals on WO_3 surface was obviously enhanced. During 60 min solar light irradiation, Pt/WO_3 achieved the highest generation rate ($0.72 \text{ a.u min}^{-1}$) of $\bullet\text{OH}$ radicals, which was much higher than those by CuO/WO_3 ($0.17 \text{ a.u min}^{-1}$) and Pd/WO_3 ($0.42 \text{ a.u min}^{-1}$). Since the photocatalytic degradation of MC-LR was initiated by the attack of $\bullet\text{OH}$ radical, Pt/WO_3 seems to be the most promising photocatalyst for MC-LR removal due to its higher generation rate of $\bullet\text{OH}$ radicals. Therefore, in the following part, Pt/WO_3 was selected as the photocatalyst for MC-LR removal under simulated solar light irradiation.

3.4. Kinetic Analysis in a Range of Light Intensities. The kinetics of photocatalytic oxidation for MC-LR were analyzed using Langmuir-Hinshelwood (L-H) model expressed as follows:

$$r = \frac{dC}{dt} = \frac{kKC}{(1 + KC)}. \quad (5)$$

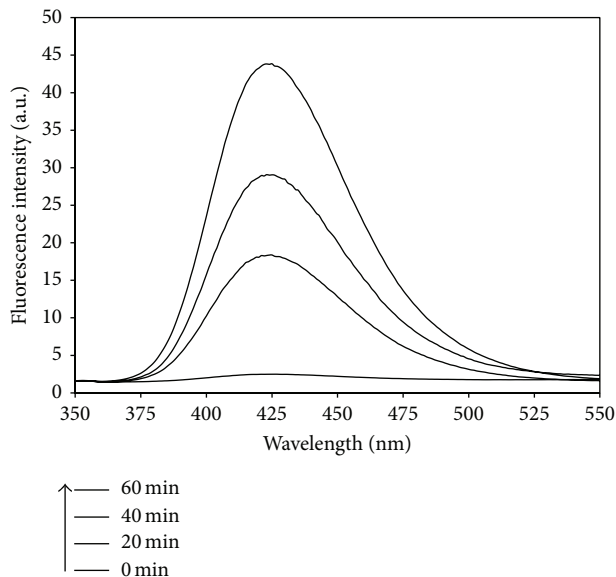


FIGURE 4: Photoluminescence spectral changes observed during irradiation of the Pt/WO₃ sample. (Experimental conditions: NaOH concentration of 2×10^{-3} M, terephthalic acid concentration of 5×10^{-4} M, Pt/WO₃ concentration of 200 mg L^{-1} , and simulated solar light intensity of 0.4 mW cm^{-2} .)

Since KC is much less than 1, if neglecting the term of KC , the L-H model can be simplified to a pseudo-first-order kinetic equation:

$$\ln\left(\frac{C_0}{C}\right) = kKt = k_{app}t, \quad (6)$$

where r is the reaction rate ($\text{mg L}^{-1} \text{ min}^{-1}$), C_0 is the initial concentration of MC-LR after dark adsorption (mg L^{-1}), C is the concentration of MC-LR at time t (mg L^{-1}), t is the irradiation time (min), k is the reaction rate constant (min^{-1}), K is the adsorption coefficient of MC-LR on a photocatalyst particle (L mg^{-1}), and k_{app} is the apparent rate constant for the photocatalytic degradation of MC-LR.

The kinetic curves for the degradation of MC-LR by Pt/WO₃ under various intensities of solar light irradiation are shown in Figure 6. The correlation coefficient (R^2) values of linear regression in all the cases are greater than 0.99, which confirms the photocatalytic degradation of MC-LR by Pt/WO₃ under simulated solar light well follows the pseudo-first-order kinetic equation. The corresponding k_{app} values of MC-LR degradation were 0.148, 0.196, and 0.241 min^{-1} under 0.2, 0.4, and 0.8 mW cm^{-2} solar light irradiation, respectively. At higher intensity of solar irradiation, more electron-hole pairs were expected to generate on photocatalyst surface, resulting in the enhancement of MC-LR degradation. According to Ohko et al. [29], if photocatalytic reaction proceeded under purely light-limited conditions, the degradation rate would depend on adsorbed photon numbers (light intensity) linearly. In this present study, a nonlinear relationship of photodegradation rate with light intensity was observed (figure was not shown) that seemingly

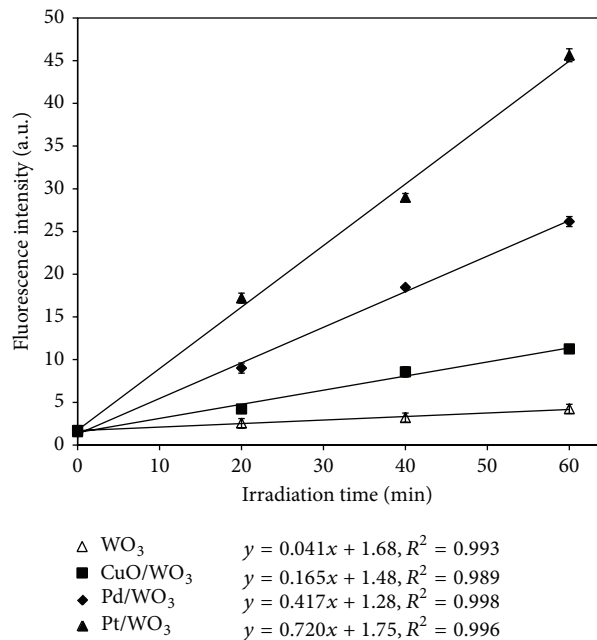


FIGURE 5: Photoluminescence intensity of pure WO₃ and modified WO₃-based photocatalysts as a function of irradiation time. (Experimental conditions: NaOH concentration of 2×10^{-3} M, terephthalic acid concentration of 5×10^{-4} M, catalyst concentration of 200 mg L^{-1} , and simulated solar light intensity of 0.4 mW cm^{-2} .)

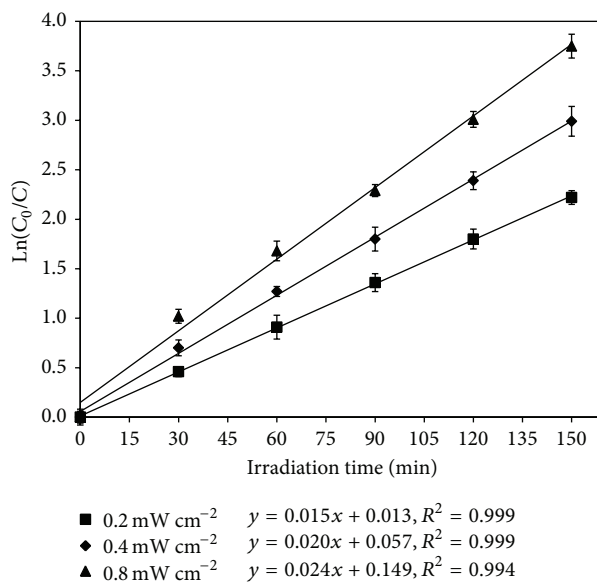


FIGURE 6: Efficiency of photocatalytic degradation of MC-LR as a function of light intensity. (Experimental conditions: MC-LR concentration of 1 mg L^{-1} and Pt/WO₃ concentration of 100 mg L^{-1} .)

implies the photocatalytic reaction proceeded under a light-rich condition. In that case, the surface adsorptive property of photocatalyst has a major influence on the photodegradation rate. Although MC-LR concentration showed a very slight decrease during 60 min dark adsorption (removal rate was less than 5%), a systematic study on the effects of initial

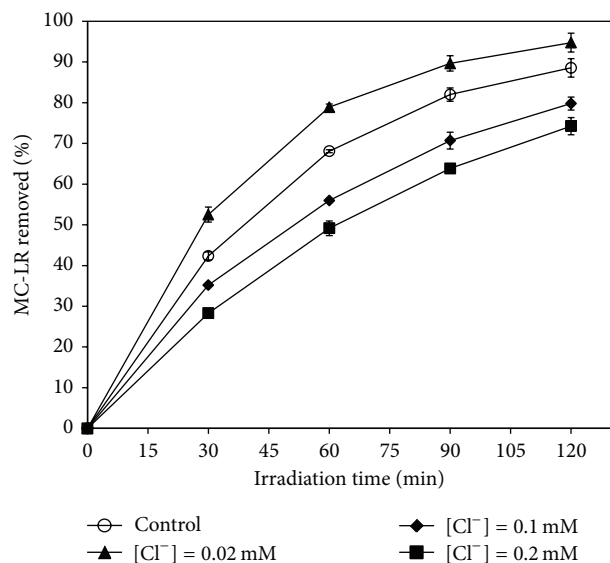


FIGURE 7: Efficiency of photocatalytic degradation of MC-LR as a function of Cl^- concentration. (Experimental conditions: MC-LR concentration of 1 mg L^{-1} , Pt/WO_3 concentration of 100 mg L^{-1} , and simulated solar light intensity of 0.4 mW cm^{-2} .)

MC-LR concentration should be carried out in the future research. That is helpful to understand clearly that the photodegradation proceeds under light-rich or light-limited condition. Since the average intensity of natural solar light is generally 0.8 mW cm^{-2} , Pt/WO_3 appears to be a promising photocatalyst for the degradation of MC-LR in practical water.

3.5. Effect of Chloride Ion (Cl^-) on the Photocatalytic Degradation of MC-LR. Sodium chloride (NaCl) was introduced into the reaction solution at different concentrations to investigate the effect of Cl^- on the photocatalytic degradation of MC-LR. As shown in Figure 7, without Cl^- addition, about 88.6% MC-LR was removed after 120 min solar light irradiation. With Cl^- addition at the concentration of 0.02 mM, the percentage removal of MC-LR increased to 94.8%, whereas the percentage removal of MC-LR decreased to 79.8% and 74.2%, when the Cl^- concentrations were 0.1 mM and 0.2 mM, respectively. The results indicate that Cl^- at proper concentration could enhance the photocatalytic degradation of MC-LR, whereas excessive Cl^- could inhibit the degradation. This phenomenon can be ascribed to the formation of Cl radicals ($\bullet\text{Cl}$) in the photocatalytic reaction system. With Cl^- addition at an appropriate concentration, the photogenerated holes on the catalyst surface were scavenged by the Cl^- ions to form $\bullet\text{Cl}$ radicals [30, 31]. The $\bullet\text{Cl}$ radical is also a kind of high reactive species that can oxidize many organic substances. Guo et al. reported that Cl^- ions adsorbed on TiO_2 surface promoted the photocatalytic oxidation of propylene [32]. However, excessive Cl^- ions can also scavenge $\bullet\text{OH}$ radicals to form Cl_2 molecules very quickly, and the reactivity of Cl_2 was lower than that of $\bullet\text{OH}$ [33]. Consequently, when adding Cl^-

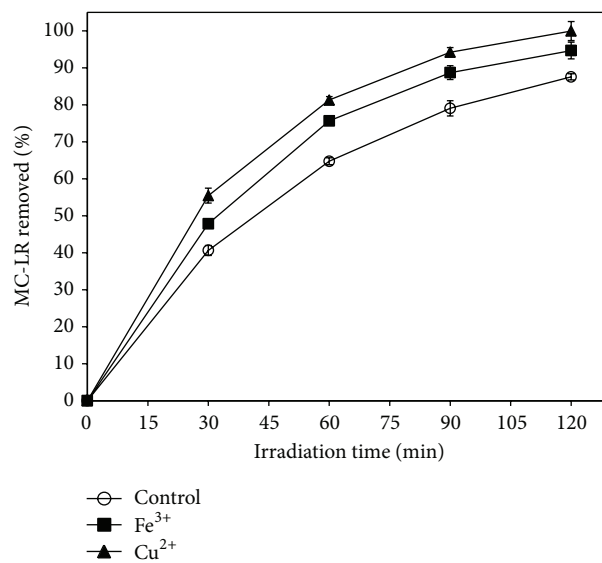


FIGURE 8: The effect of 0.2 mM of metal ions on the efficiency of photocatalytic degradation of MC-LR. (Experimental conditions: MC-LR concentration of 1 mg L^{-1} , Pt/WO_3 concentration of 100 mg L^{-1} , and simulated solar light intensity of 0.4 mW cm^{-2} .)

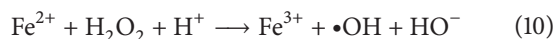
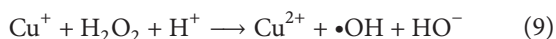
at an excessive concentration, the Cl^- ions began to scavenge $\bullet\text{OH}$ radicals preferentially that decreased the photocatalytic degradation of MC-LR.

3.6. Effect of Metal Cations (Cu^{2+} and Fe^{3+}) on the Photocatalytic Degradation of MC-LR. The fast recombination of photogenerated electrons and holes on the catalyst surface is an important factor that limits the photocatalytic degradation of organic substances. Consequently, to enhance the photocatalytic activity of catalysts, improving the separation of photogenerated electron-hole pairs is very essential. Metal cations can be used as the scavengers of photogenerated electrons and seem to be an effect additive for suppressing the recombination of photogenerated electrons and holes. The enhanced photocatalytic activity of WO_3 by addition of Cu^{2+} and Fe^{3+} in the reaction solution has been reported for the degradation of various organic substances such as phenol and sucrose [34, 35].

In order to investigate the effects of metal cations on photocatalytic degradation of MC-LR, $\text{Cu}(\text{NO}_3)_2$ and $\text{Fe}(\text{NO}_3)_3$ were introduced into the reaction solutions at a concentration of 0.2 mM. As shown in Figure 8, without metal cations addition, about 87.6% MC-LR was removed after 120 min solar light irradiation. In the presence of 0.2 mM Cu^{2+} and Fe^{3+} , the percentage removal of MC-LR increased to 100% and 94.7%, respectively. The addition of Cu^{2+} and Fe^{3+} obviously enhanced the photocatalytic degradation of MC-LR under solar light irradiation.

The possible mechanism for the enhanced photocatalytic activity of Pt/WO_3 by Cu^{2+} and Fe^{3+} addition can be described as follows. (1) The consumption of photogenerated electrons by the reduction of Cu^{2+} and Fe^{3+} ions suppressed

the recombination of electrons and holes that increased the number of $\bullet\text{OH}$ radicals in the reaction system (7) and (8) [36]. In addition, (2) the Cu^{2+} and Fe^{3+} can react with H_2O_2 generated in a photo-Fenton reaction to produce additional $\bullet\text{OH}$ radicals in the reaction system (9) and (10). Consider



Then, the increased number of $\bullet\text{OH}$ radicals in the reaction solution promoted the photocatalytic degradation of MC-LR [37, 38]. According to Irie et al. [39] and Liu et al. [40], electrons in the surface grafted Fe^{3+} and Cu^{2+} ions efficiently cause multielectron reduction of adsorbed O_2 molecules to achieve high quantum efficiency value. Therefore, the H_2O_2 produced during the multielectron reduction of O_2 molecules also promoted the photodegradation of MC-LR in aqueous solution.

3.7. Photocatalytic Degradation Pathway of MC-LR. The degradation pathway of MC-LR through photocatalytic reaction has been in detail reported by Su et al. [41]. As shown in Figure 9, MC-LR is a relatively large molecule with a cyclo-structure, which consists of a usual 20-carbon amino acid (ADDA) that expresses biological toxicity and an amino acid N-methyldehydroalanine (MDHA). The MC-LR molecule is more readily attacked by $\bullet\text{OH}$ radicals at four sites of the toxin: three on the ADDA chain ((A) aromatic ring, (B) methoxy group, and (C) conjugated double bonds) and one on the cyclic structure ((D) MDHA amino acid) [28]. Among these, the conjugated double bond (site (C)) at the ADDA moiety of MC-LR molecule has been reported to be susceptible to photocatalytic attack [42, 43]. The destruction of MC-LR molecule by the attack of $\bullet\text{OH}$ radicals on these sensitive sites leads to production of many kinds of intermediate products, which can be degraded to final products by further reaction with $\bullet\text{OH}$ radicals.

In this present study, although the complete removal of MC-LR was obtained after 180 min solar irradiation when using Pt/WO_3 as photocatalyst, less than 50% of the total MC-LR was mineralized. This can be attributed to the production of many kinds of intermediates which are stable against photocatalytic destruction and do not undergo complete oxidation. Since MC-LR was not completely mineralized, it is important to confirm that the intermediate products are nontoxic. Lawton et al. [14] assessed the toxicity of intermediates produced in photocatalytic degradation of MC-LR using brine shrimp bioassay method, and they could not detect any measureable toxicity.

4. Conclusions

A series of advanced WO_3 -based photocatalysts including CuO/WO_3 , Pd/WO_3 , and Pt/WO_3 were developed for

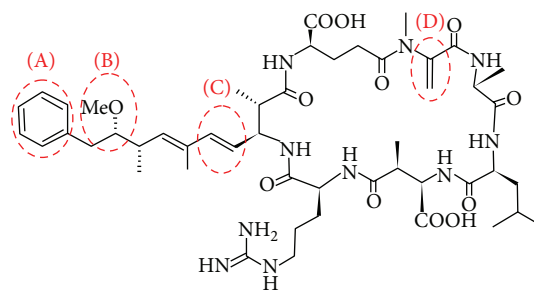


FIGURE 9: The molecular structure of microcystin-LR and the main attack sites ((A) benzene ring; (B) methoxy group; (C) conjugated double bond; (D) unsaturated double bond of MDHA) of hydroxyl radicals during photocatalytic reaction. ADDA: 3-amino-methoxy-10-phenyl-2,6,8-trimethyl-deca-4,6-dienoic acid.

the photocatalytic removal of microcystin-LR (MC-LR) under simulated solar light irradiation. In this present study, when doped with CuO , Pd , and Pt , the generation rate of $\bullet\text{OH}$ radicals on WO_3 surface was obviously enhanced. Pt/WO_3 achieved the highest generation rate of $\bullet\text{OH}$ radicals and exhibited the best photocatalytic performance for the degradation of MC-LR under solar light irradiation. The photocatalytic degradation of MC-LR by Pt/WO_3 under solar light well followed the pseudo-first-order kinetic equation. Cl^- addition at an appropriate concentration could enhance the photocatalytic degradation of MC-LR by Pt/WO_3 under solar light irradiation. The addition of Cu^{2+} and Fe^{3+} obviously enhanced the photocatalytic degradation of MC-LR under solar light irradiation. The developed Pt/WO_3 is a promising photocatalyst for enhancing the photocatalytic removal of recalcitrant organic compounds like MC-LR in water under solar light irradiation.

Conflict of Interests

The authors declare that there is no conflict of interests regarding the publication of this paper.

Acknowledgment

This work was supported in part by Grant-in-Aid for Exploratory Research 26670901 and Scientific Research (A) 22248075 from Japan Society for the Promotion of Science (JSPS).

References

- [1] W. W. Carmichael, "Cyanobacteria secondary metabolites—the cyanotoxins," *Journal of Applied Bacteriology*, vol. 72, no. 6, pp. 445–459, 1992.
- [2] F. Al Momani, D. W. Smith, and M. Gamal El-Din, "Degradation of cyanobacteria toxin by advanced oxidation processes," *Journal of Hazardous Materials*, vol. 150, no. 2, pp. 238–249, 2008.
- [3] R. E. Honkanen, J. Zwiller, R. E. Moore et al., "Characterization of microcystin-LR, a potent inhibitor of type 1 and type 2A

- protein phosphatases," *The Journal of Biological Chemistry*, vol. 265, no. 32, pp. 19401–19404, 1990.
- [4] V. M. Vasconcelos and E. Pereira, "Cyanobacteria diversity and toxicity in a wastewater treatment plant (Portugal)," *Water Research*, vol. 35, no. 5, pp. 1354–1357, 2001.
 - [5] K. Himberg, A.-M. Keijola, L. Hiisvirta, H. Pyysalo, and K. Sivonen, "The effect of water treatment processes on the removal of hepatotoxins from *Microcystis* and *Oscillatoria* cyanobacteria: a laboratory study," *Water Research*, vol. 23, no. 8, pp. 979–984, 1989.
 - [6] S. Takenaka and Y. Tanaka, "Behavior of microcystins and its decomposition product in water treatment process," *Chemosphere*, vol. 31, no. 7, pp. 3635–3641, 1995.
 - [7] C. Shifu and C. Gengyu, "Photocatalytic degradation of organophosphorus pesticides using floating photocatalyst $\text{TiO}_2 \cdot \text{SiO}_2$ /beads by sunlight," *Solar Energy*, vol. 79, no. 1, pp. 1–9, 2005.
 - [8] M. Sharon, B. Pal, and D. V. Kamat, "Photocatalytic killing of pathogenic bacterial cells using nanosize Fe_2O_3 and carbon nanotubes," *Journal of Biomedical Nanotechnology*, vol. 1, no. 4, pp. 365–368, 2005.
 - [9] M. C. López, M. I. Fernández, S. Rodríguez, J. A. Santaballa, S. Steenken, and E. Vulliet, "Mechanisms of direct and TiO_2 -photocatalysed UV degradation of phenylurea herbicides," *ChemPhysChem*, vol. 6, no. 10, pp. 2064–2074, 2005.
 - [10] T. Arai, M. Yanagida, Y. Konishi, Y. Iwasaki, H. Sugihara, and K. Sayama, "Efficient complete oxidation of acetaldehyde into CO_2 over $\text{CuBi}_2\text{O}_4/\text{WO}_3$ composite photocatalyst under visible and UV light irradiation," *The Journal of Physical Chemistry C*, vol. 111, no. 21, pp. 7574–7577, 2007.
 - [11] M. Miyauchi, "Photocatalysis and photoinduced hydrophilicity of WO_3 thin films with underlying Pt nanoparticles," *Physical Chemistry Chemical Physics*, vol. 10, no. 41, pp. 6258–6265, 2008.
 - [12] U. I. Gaya and A. H. Abdullah, "Heterogeneous photocatalytic degradation of organic contaminants over titanium dioxide: a review of fundamentals, progress and problems," *Journal of Photochemistry and Photobiology C: Photochemistry Reviews*, vol. 9, no. 1, pp. 1–12, 2008.
 - [13] N. Genç, "Photocatalytic oxidation of a reactive azo dye and evaluation of the biodegradability of photocatalytically treated and untreated dye," *Water SA*, vol. 30, no. 3, pp. 399–405, 2004.
 - [14] L. A. Lawton, P. K. J. Robertson, B. J. P. A. Cornish, and M. Jaspars, "Detoxification of microcystins (cyanobacterial hepatotoxins) using TiO_2 photocatalytic oxidation," *Environmental Science and Technology*, vol. 33, no. 5, pp. 771–775, 1999.
 - [15] I. Liu, L. A. Lawton, D. W. Bahnemann, and P. K. J. Robertson, "The photocatalytic destruction of the cyanotoxin, nodularin using TiO_2 ," *Applied Catalysis B: Environmental*, vol. 60, no. 3–4, pp. 245–252, 2005.
 - [16] Z.-G. Zhao and M. Miyauchi, "Nanoporous-walled tungsten oxide nanotubes as highly active visible-light-driven photocatalysts," *Angewandte Chemie*, vol. 47, no. 37, pp. 7051–7055, 2008.
 - [17] O. Akhavan and E. Ghaderi, "Self-accumulated Ag nanoparticles on mesoporous TiO_2 thin film with high bactericidal activities," *Surface and Coatings Technology*, vol. 204, no. 21–22, pp. 3676–3683, 2010.
 - [18] O. Akhavan, "Lasting antibacterial activities of Ag- TiO_2 /Ag/a- TiO_2 nanocomposite thin film photocatalysts under solar light irradiation," *Journal of Colloid and Interface Science*, vol. 336, no. 1, pp. 117–124, 2009.
 - [19] J. Zhang, H. Zhu, S. Zheng, F. Pan, and T. Wang, " TiO_2 Film/ Cu_2O microgrid heterojunction with photocatalytic activity under solar light irradiation," *Applied Materials and Interfaces*, vol. 1, no. 10, pp. 2111–2114, 2009.
 - [20] Y. Lv, L. Yu, H. Huang, H. Liu, and Y. Feng, "Preparation, characterization of P-doped TiO_2 nanoparticles and their excellent photocatalytic properties under the solar light irradiation," *Journal of Alloys and Compounds*, vol. 488, no. 1, pp. 314–319, 2009.
 - [21] R. Abe, H. Takami, N. Murakami, and B. Ohtani, "Pristine simple oxides as visible light driven photocatalysts: highly efficient decomposition of organic compounds over platinum-loaded tungsten oxide," *Journal of the American Chemical Society*, vol. 130, no. 25, pp. 7780–7781, 2008.
 - [22] T. Arai, M. Horiguchi, M. Yanagida, T. Gunji, H. Sugihara, and K. Sayama, "Complete oxidation of acetaldehyde and toluene over a Pd/ WO_3 photocatalyst under fluorescent- or visible-light irradiation," *Chemical Communications*, no. 43, pp. 5565–5567, 2008.
 - [23] T. Arai, M. Yanagida, Y. Konishi, Y. Iwasaki, H. Sugihara, and K. Sayama, "Promotion effect of CuO co-catalyst on WO_3 -catalyzed photodegradation of organic substances," *Catalysis Communications*, vol. 9, no. 6, pp. 1254–1258, 2008.
 - [24] L. Li and Y. Liu, "Ammonia removal in electrochemical oxidation: mechanism and pseudo-kinetics," *Journal of Hazardous Materials*, vol. 161, no. 2–3, pp. 1010–1016, 2009.
 - [25] Y. Liu, Y. Ohko, R. Zhang, Y. Yang, and Z. Zhang, "Degradation of malachite green on Pd/ WO_3 photocatalysts under simulated solar light," *Journal of Hazardous Materials*, vol. 184, no. 1–3, pp. 386–391, 2010.
 - [26] K.-I. Ishibashi, A. Fujishima, T. Watanabe, and K. Hashimoto, "Detection of active oxidative species in TiO_2 photocatalysis using the fluorescence technique," *Electrochemistry Communications*, vol. 2, no. 3, pp. 207–210, 2000.
 - [27] Q. Xiao, Z. Si, J. Zhang, C. Xiao, and X. Tan, "Photoinduced hydroxyl radical and photocatalytic activity of samarium-doped TiO_2 nanocrystalline," *Journal of Hazardous Materials*, vol. 150, no. 1, pp. 62–67, 2008.
 - [28] I. Liu, L. A. Lawton, and P. K. J. Robertson, "Mechanistic studies of the photocatalytic oxidation of microcystin-LR: an investigation of byproducts of the decomposition process," *Environmental Science and Technology*, vol. 37, no. 14, pp. 3214–3219, 2003.
 - [29] Y. Ohko, K. Hashimoto, and A. Fujishima, "Kinetics of photocatalytic reactions under extremely low-intensity UV illumination on titanium dioxide thin films," *The Journal of Physical Chemistry A*, vol. 101, no. 43, pp. 8057–8062, 1997.
 - [30] G. Munuera, A. Navio, J. Soria, and A. R. Gonzalez-elipe, "Photo-adsorption of oxygen on chlorinated TiO_2 surfaces; a possible way to photo-oxy-chlorinations," in *Studies in Surface Science and Catalysis*, T. Seiyama and K. Tanabe, Eds., vol. 7, pp. 1185–1197, 1981.
 - [31] S. Kutsuna, Y. Ebihara, K. Nakamura, and T. Ibusuki, "Heterogeneous photochemical reactions between volatile chlorinated hydrocarbons (trichloroethene and tetrachloroethene) and titanium dioxide," *Atmospheric Environment A: General Topics*, vol. 27, no. 4, pp. 599–604, 1993.
 - [32] J. Guo, L. Mao, J. Zhang, and C. Feng, "Role of Cl^- ions in photooxidation of propylene on TiO_2 surface," *Applied Surface Science*, vol. 256, no. 7, pp. 2132–2137, 2010.
 - [33] H.-C. Liang, X.-Z. Li, Y.-H. Yang, and K.-H. Sze, "Effects of dissolved oxygen, pH, and anions on the 2,3-dichlorophenol degradation by photocatalytic reaction with anodic TiO_2 nanotube films," *Chemosphere*, vol. 73, no. 5, pp. 805–812, 2008.

- [34] T. Arai, M. Yanagida, Y. Konishi, H. Sugihara, and K. Sayama, "Utilization of $\text{Fe}^{3+}/\text{Fe}^{2+}$ redox for the photodegradation of organic substances over WO_3 photocatalyst and for H_2 production from the electrolysis of water," *Electrochemistry*, vol. 76, no. 2, pp. 128–131, 2008.
- [35] D. Beydoun, H. Tse, R. Amal, G. Low, and S. McEvoy, "Effect of copper(II) on the photocatalytic degradation of sucrose," *Journal of Molecular Catalysis A: Chemical*, vol. 177, no. 2, pp. 265–272, 2002.
- [36] M. D. Ward and A. J. Bard, "Photocurrent enhancement via trapping of photogenerated electrons of TiO_2 particles," *Journal of Physical Chemistry*, vol. 86, no. 18, pp. 3599–3605, 1982.
- [37] K. Okamoto, Y. Yamamoto, H. Tanaka, M. Tanaka, and A. Itaya, "Heterogeneous photocatalytic decomposition of phenol over TiO_2 powder," *Bulletin of the Chemical Society of Japan*, vol. 58, no. 7, pp. 2015–2022, 1985.
- [38] T. Y. Wei and C. C. Wan, "Kinetics of photocatalytic oxidation of phenol on TiO_2 surface," *Journal of Photochemistry and Photobiology, A: Chemistry*, vol. 69, no. 2, pp. 241–249, 1992.
- [39] H. Irie, S. Miura, K. Kamiya, and K. Hashimoto, "Efficient visible light-sensitive photocatalysts: Grafting Cu(II) ions onto TiO_2 and WO_3 photocatalysts," *Chemical Physics Letters*, vol. 457, no. 1–3, pp. 202–205, 2008.
- [40] M. Liu, X. Qiu, M. Miyauchi, and K. Hashimoto, "Energy-level matching of Fe(III) ions grafted at surface and doped in bulk for efficient visible-light photocatalysts," *Journal of the American Chemical Society*, vol. 135, no. 27, pp. 10064–10072, 2013.
- [41] Y. Su, Y. Deng, and Y. Du, "Alternative pathways for photocatalytic degradation of microcystin-LR revealed by TiO_2 nanotubes," *Journal of Molecular Catalysis A: Chemical*, vol. 373, pp. 18–24, 2013.
- [42] M. Welker and C. Steinberg, "Rates of humic substance photosensitized degradation of microcystin-LR in natural waters," *Environmental Science and Technology*, vol. 34, no. 16, pp. 3415–3419, 2000.
- [43] P. Chen, L. Zhu, S. Fang, C. Wang, and G. Shan, "Photocatalytic degradation efficiency and mechanism of microcystin-RR by mesoporous Bi_2WO_6 under near ultraviolet light," *Environmental Science & Technology*, vol. 46, no. 4, pp. 2345–2351, 2012.

Review Article

Recent Trends in Rapid Environmental Monitoring of Pathogens and Toxicants: Potential of Nanoparticle-Based Biosensor and Applications

Preeyaporn Koedrith,¹ Thalisa Thasiphu,¹ Jong-II Weon,² Rattana Boonprasert,¹ Kooranee Tuitemwong,³ and Pravate Tuitemwong⁴

¹Faculty of Environment and Resource Studies, Mahidol University, Phutthamonthon District, Nakhon Pathom 73170, Thailand

²Department of Safety Engineering, Institute of Environmental Medicine for Green Chemistry, Dongguk University, Gyeongju, Gyeongbuk 780-714, Republic of Korea

³Department of Microbiology, Kasetsart University, Bangkok 10900, Thailand

⁴Food Safety Center, Institute for Scientific and Technological Research and Services (ISTRs), King Mongkut's University of Technology Thonburi (KMUTT), Bangkok 10140, Thailand

Correspondence should be addressed to Pravate Tuitemwong; ptt59@hotmail.com

Received 30 July 2014; Revised 7 November 2014; Accepted 7 November 2014

Academic Editor: Xiao-Feng Zhao

Copyright © 2015 Preeyaporn Koedrith et al. This is an open access article distributed under the Creative Commons Attribution License, which permits unrestricted use, distribution, and reproduction in any medium, provided the original work is properly cited.

Of global concern, environmental pollution adversely affects human health and socioeconomic development. The presence of environmental contaminants, especially bacterial, viral, and parasitic pathogens and their toxins as well as chemical substances, poses serious public health concerns. Nanoparticle-based biosensors are considered as potential tools for rapid, specific, and highly sensitive detection of the analyte of interest (both biotic and abiotic contaminants). In particular, there are several limitations of conventional detection methods for water-borne pathogens due to low concentrations and interference with various enzymatic inhibitors in the environmental samples. The increase of cells to detection levels requires long incubation time. This review describes current state of biosensor nanotechnology, the advantage over conventional detection methods, and the challenges due to testing of environmental samples. The major approach is to use nanoparticles as signal reporter to increase output rather than spending time to increase cell concentrations. Trends in future development of novel detection devices and their advantages over other environmental monitoring methodologies are also discussed.

1. Introduction

Environmental pollution is the major source of problem to human health and sustainable development of society and economy. The presence of environmental pathogens and their toxins, heavy metals, and organic pollutants is a serious environmental issue that drew scientific interest and public concern [1–3]. Several environmental microorganisms cause different clinical diseases and morbidities, resulting in public health burden. Particularly, the presence of water-borne pathogens in water streamline is critical issue for regulatory agencies, healthcare agencies, and industry sectors. These pathogens should therefore be routinely monitored under clinical diagnostic procedures. For instance,

Cryptosporidium parvum, one of water-borne pathogens that contaminated drinking water, can cause disease even at low levels. The detection of water-borne pathogen using commercially available assays has been successfully achieved with detection limit of 10–1,000 organisms per mL (such as the widely used MERIFLUOR *Cryptosporidium*/*Giardia* test from Meridian Biosciences). Owing to low numbers of target microorganisms, step of culture preenrichment become necessary to increase their numbers to detectable level for several hours. Likewise, sensitive polymerase chain reaction-(PCR-) based techniques require preenrichment culturing process to efficiently detect environmental pathogens. In accordance with the US Environmental Protection Agency (EPA) Methods 1622 and 1623, preconcentration by filtration

of 10-liter water sample is essential for detection of *C. parvum* oocysts.

The environmental sector urgently needs diagnostic system and test kits which are sensitive, cost-effective, and portable. Potential applications of nanotechnology enable researchers to use pathogen diagnostics as well as developing a new generation of biosensors and imaging techniques with higher sensitivity and reliability. Particularly, high sensitivity fluorescent dye doped nanoparticles provide important feature for increasing the signals by the magnitude of 10^5 to 10^6 times as well as tagging pathogens, enabling the instrument to detect specimens at very low levels. Furthermore, nanobiotechnology improves the performance of instrument for wider commercial deployment of the instrument at environmental site.

Nanoparticles (about 1–100 nm in diameter) display unique properties over bulk-sized materials and thus have been widely used in various areas, including biomedical, electronic, environmental, pharmaceutical, cosmetic, and energy [4, 5]. Indeed, environmental monitoring and diagnostics have been improved by using nanoparticles for detecting biotic and abiotic contaminants (e.g., pathogens and their toxins as well as metal ions and organic pollutants, resp.). Incorporating the nanoparticles into nanosensors provides advantages of rapid and high-throughput detecting ability on a portable device. The nanoparticles are considered as potential sensing materials due to strong physical confinement of electrons at nanoscale. Their tiny size correspond high surface-to-volume ratios. Additionally, their physical properties can be customized since they are directly related to size, composition, and shape. Surface-modified nanocolloids, such as gold nanoparticles (GNPs) [6], magnetic nanoparticles (MNPs) [7], quantum dots (QDs) [8], and carbon nanotubes, exhibit specific target-binding properties. Therefore, the distinct small size and nanoscale properties of nanoparticles are useful for new-generation environmental detection.

Use of fluorescence nanoparticles in combination with magnetic beads capable of capturing and concentrating target specimens in the sampling process has been established to overcome the limitation of fluorescence intensity [9–12]. Fluorescent nanoparticles (about 10–20 μm diameter in range) including semiconductor nanoparticles, quantum dots, metal nanoparticles, silica nanoparticles, and polymer nanoparticles have been focused for research and development. Fluorescent nanoparticles display distinct features, such as high fluorescence intensity, photostability, photobleaching resistance, and biocompatibility. Their emission spectra show narrow peaks. The emission wavelength peak or fluorescent color can be adjusted based on their particle size during production. Based on the fact that one excitation source or wavelength with spectrum of ultraviolet or blue that excites certain fluorescent nanoparticles with different sizes simultaneously yields multiple emission spectra, multicolorimetric or multiplex assay format can be accomplished using a single light source [13]. The fluorescent nanoparticles are also served as multivalent scaffolds for supramolecular assemblies as well as versatile synthetic platform for surface

coatings via chemical conjugation to bioreceptors (such as antibodies, aptamers, and other agents) [14]. Owing to their excellent properties, they become powerful tools for monitoring several different species under both biological and environmental purposes. For example, antibody- and DNA aptamer-based assays with and without the use of magnetic beads-mediated capture and filtration can detect bacteria as low as 10 cells per mL and several thousands of *C. parvum* oocysts [15–17]. In this review, the applications and developments of fluorescent nanoparticles and other potential nanoparticles are focused in terms of chemical and biological sensing within the environmental samples.

2. Potential Applications of Nanotechnology

Conventional molecular-based detection techniques are commonly used to identify pathogenic agents with high degree of sensitivity and reproducibility [18]. Mostly, these techniques cannot be employed in the field (e.g., rivers and drinking water distributors) since they usually require complex instrumentation and well-trained operator. Expensive and short shelf half-life of certain reagents (e.g., enzymes and oligonucleotides) also limits the utility of conventional pathogen detection techniques in rural areas of developing countries. Despite their high sensitivity, current technologies like enzyme-linked immunosorbent assay (ELISA) and polymerase chain reaction (PCR) still require extensive sample preparation and have long readout periods, resulting in delayed response and disease containment. Thus, taking advantage of the unique properties of nanoparticles (e.g., electrical, magnetic, luminescent, and catalytic capacity), economical detection assays with high speediness and sensitivity can be developed to promptly monitor environmental specimens, especially microbial pathogens. Nanoparticles when acting as signal reporter will increase signal significantly and, hence, reduce or eliminate the time to increase target cells to detectable level. Apart from high sensitivity and speediness, nanotechnology-based systems are developed to have reasonable reproducibility, cost-effectiveness, robustness, and user-friendly properties, allowing their applications even in field applications. The techniques with nanoparticles require universal testing instrument available in most laboratories such as spectrophotometer, fluorescent microscope, and luminometer and some reactions could be observed with naked eyes.

Moreover, assays without any sample preparation have been established using innovative nanotechnological tools, leading to user-friendly platforms with rapid and reliable results [19]. As presented in Figure 1, different nanoparticles show specific optical, fluorescence, and magnetic properties, and integrations between these properties hold great promise for environmental screening. In particular, the applications of nanoparticle-based technology enable us to monitor or even improve quality of air, water, and soil. For example, silica nanoparticles are considered an appropriate choice with multiple functional abilities as to deliver antimicrobial agents for treating towards particular pathogenic microorganisms and to sense the microorganisms [20]. Therefore, this further section summarizes the impact of sensing nanotechnology

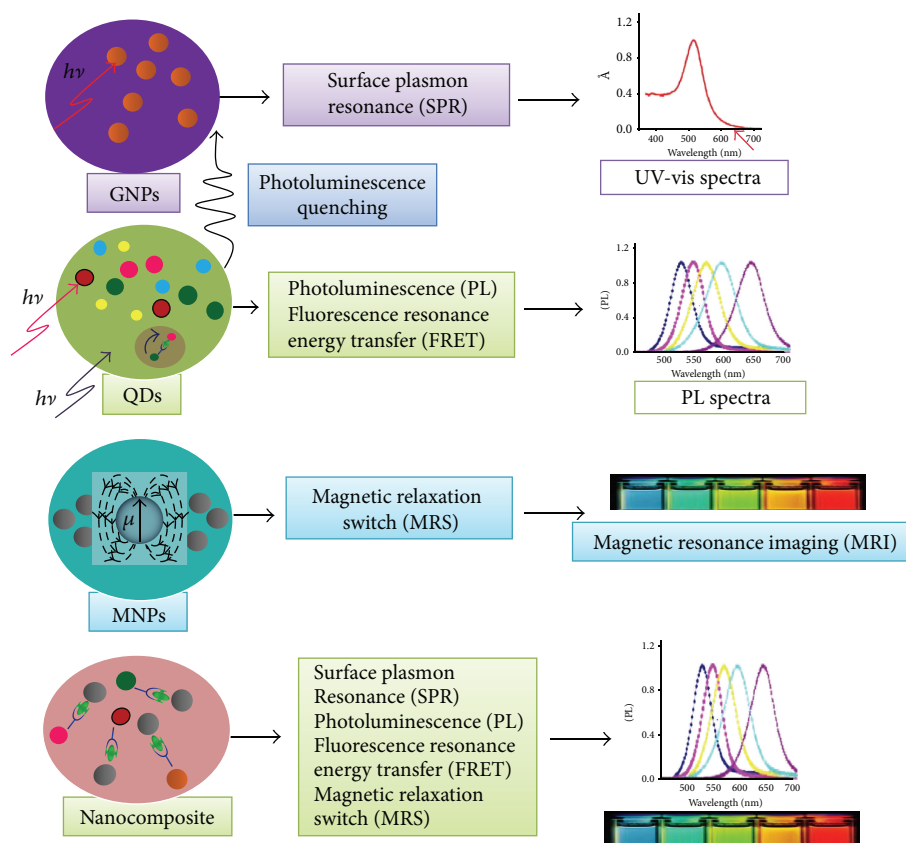


FIGURE 1: Schematic diagram illustrating different nanoparticles conferring optical (e.g., gold nanoparticles (GNPs)), fluorescence (e.g., quantum dots (QDs)), and magnetic (e.g., magnetic nanoparticles (MNPs)) properties, and combinations between these particles as nanocomposites conferring multifunctionalities provide distinct advantages for environmental monitoring.

on improving the current testing procedures for accurate and precise monitoring of environmental pathogens and other contaminants.

3. Necessary Characteristics for Development of Nanoparticle-Based Biosensor

Biosensor is typically comprised of two main components: a bioreceptor and a transducer [21]. The bioreceptor is a biomolecule that recognizes the target analyte whereas the transducer converts the recognition event into a measurable signal. The bioreceptor is a biological molecular species (e.g., antibody, enzyme, and nucleic acid), a living biological system (e.g., cells, tissue, or whole organisms), or biomimetic material (e.g., synthetic bioreceptor) that utilizes a biochemical mechanism for recognition. The transducer is a device capable of converting a signal in one form to another form of energy. For transducer classification, common techniques include optical (e.g., luminescence and absorption), electrochemical (e.g., current and voltage), and mechanical measurements (e.g., magnetic resonance). In principle, the detection occurred by the specific binding of target analyte to the complementary biorecognition element (namely, bioreceptor) immobilized on an appropriate supportive medium. The specific interaction causes alteration in one or more

physicochemical properties that is detectable using the second component, so-called transducer. Usually, magnitude of signal is proportionally related to the concentration of a specific analyte captured by the biorecognition element [22] (Figure 2).

For development of a biosensor system, some requirements for commercialization are as follows [23].

- Specificity.** The biosensor device should be highly specific to the target analyte and exhibits minimum or no cross reactivity with moieties conferring similar chemical structure.
- Sensitivity.** The biosensor device should be able to measure in the range of a given target analyte of interest with minimum additional steps such as pre-cleaning and preconcentration of the samples.
- Response Linearity.** The linear response range of the system should cover the concentration range over which the target analyte is measurable.
- Reproducibility.** When samples at same concentrations are analyzed several times, they should produce same signal intensity or magnitude.
- Short Response and Recovery Time.** The biosensor device response should be rapid enough for real-time monitoring of the target analyte. The recovery time

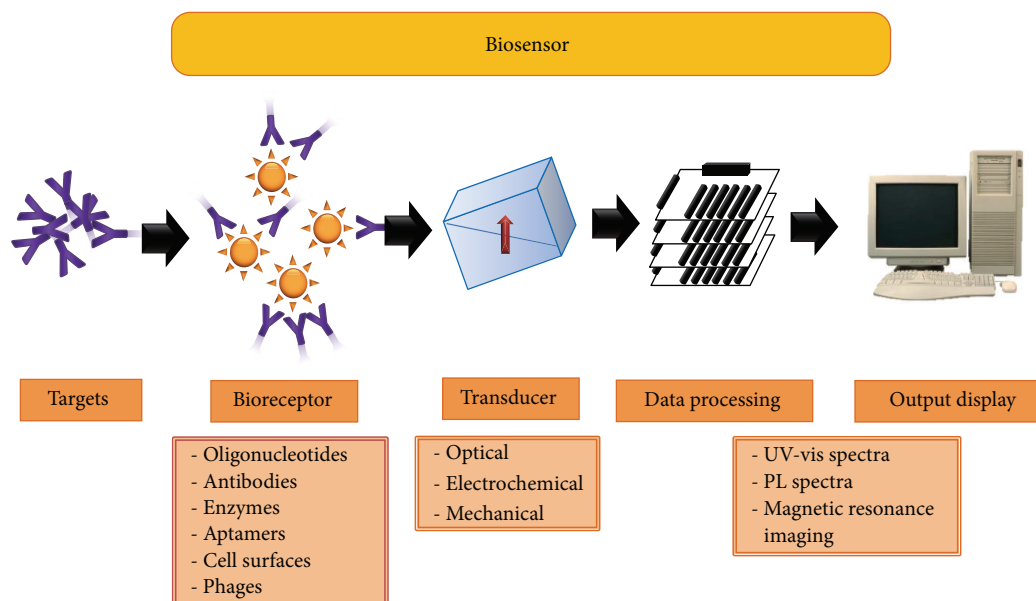


FIGURE 2: Scheme representing nanobiosensor components consisting of different bioreceptors (e.g., antibodies, aptamers, cell-surface molecules, enzymes, oligonucleotide probes, and phages) and major transducers depending on types of signal response (i.e., optical, electrochemical, and mechanical signal). Output can be displayed as UV-visible or photoluminescence spectra and magnetic resonance images.

of the biosensor system should be short enough for efficient reusability.

- (f) *Stability and Operating Life.* The signal of biosensor device response should be stable enough for real-time monitoring of the target analyte. The components of biosensor device should be resistant to deterioration throughout the operating period. The operating lifetime should be long enough for monitoring of the target analyte. Of concern, most of the biological components are unstable in different biochemical conditions.

4. Characteristics of Environmental Nanobiosensors Based on Potential Nanomaterials

Biosensor is defined as a device or an assay with use of a biorecognition element coupled to a signal transducer for measurement an analyte of interest [24]. Common biorecognition elements include oligonucleotide probes, antibodies, enzymes, aptamers, cell-surface molecules [25], and phages [26]. Transducers are divided into three main types: optical, electrochemical, and mechanical. As shown in Figure 3, schemes illustrate fundamental principle of biosensor-based detection: the full spectrum of biorecognition elements and transduction methods was reportedly established for detection of particular water-borne pathogens, with oligonucleotide probes and antibodies being the most common.

4.1. Nanoparticle-Based Optical Sensors. Gold nanoparticles (GNPs) that are widely used have various nanostructures.

Owing to their low dimensionality and relevant properties, they are thus introduced into novel applications in photonic, electronic, and sensing sections. With color and fluorescence properties of gold nanoparticles and quantum dots, they are commonly utilized in optical sensors for detection of toxins, heavy metals, and other environmental contaminants, as discussed below. Typically, gold nanoparticles display various colors (ranging from red to purple or blue) depending on interparticle reactions during aggregation or dispersion of the aggregates (Figure 3(b)) [27] while quantum dots exhibit changes in photoluminescence intensity (Figure 3(b)) [27]. Optical sensors are served as powerful tools for detecting environmental contaminants since they exhibit high signal-to-noise ratios.

Potential natural toxins, such as ochratoxin A (OTA), zearalenone (ZEA), and aflatoxin B1 (AFB1), are produced from certain fungi *Aspergillus ochraceus*, *Aspergillus flavus*, *Aspergillus parasiticus*, and *Fusarium graminearum*. They are often contaminated in cereals, cereal products, and coffee beans and exhibit teratogenic, mutagenic, and immunosuppressive activity in human. Moreover, another class of toxins is also generated from particular bacteria *Bacillus botulinus*, *Escherichia coli*, or *Ricinus communis* that are usually found in animal tissues and plant. These toxins can produce high toxicity and induce injury to human. Owing to high affinity of the toxin ricin to sugar underlying the naturally occurring infection mechanism, gold nanoparticles were coated with sugar to detect ricin and readout can be visualized [28]. Combination of chromatographic technology with conventional immunoassays (namely, immune-chromatographic strip assays) facilitates a rapid and affordable tool for toxin diagnosis [29]. Different types of immune-chromatographic assays with use of gold

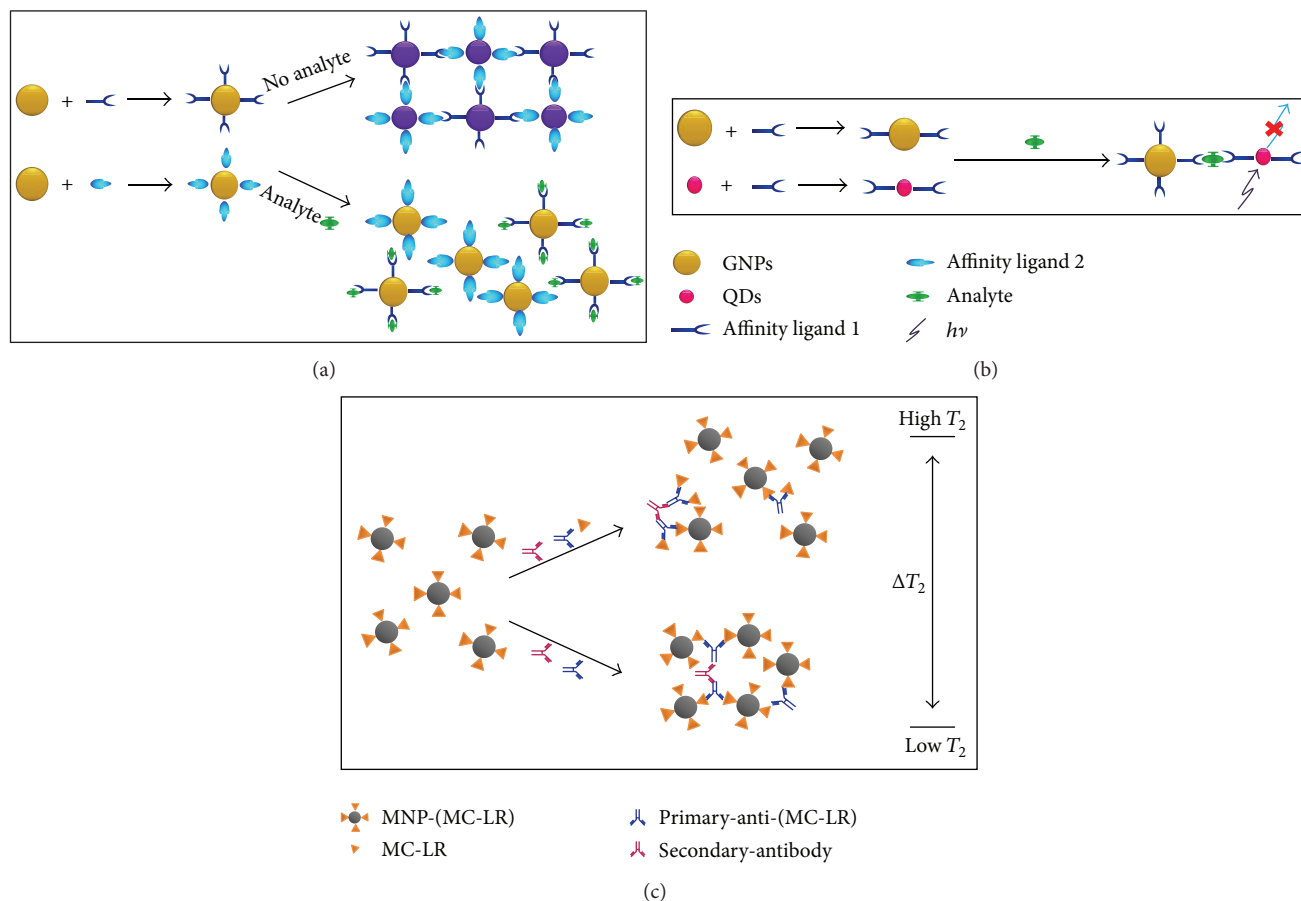


FIGURE 3: Scheme depicting principle of biosensor-based detection using (a) gold nanoparticles and (b) quantum dots as well as (c) magnetic nanoparticle aggregates for detection of microcystin-LR (MC-LR), naturally occurring toxin produced from cyanobacteria.

nanoparticles-antibody conjugates were developed for detection of ochratoxin A [29, 30], zearalenone [31], and aflatoxin B1 [32]. The immune-chromatographic strip assay has advantages in terms of format simplicity, speediness, and stability over a wide range of conditions, allowing for on-site testing by untrained users.

Of ongoing global concern, heavy metal contamination in environment can cause problems on both public human and environmental health. Hence, environmental monitoring of aqueous heavy metal ions becomes crucial. A variety of nanoparticles-based sensors for sensing selective heavy metal ions have been successfully conducted. By using hyper-Rayleigh scattering technique, a gold nanoparticle-based sensor was utilized for rapid screening of mercury (Hg^{2+}) ions in aqueous solutions with a sensitivity of 5 ng/mL (ppb) [33]. Additionally, L-cysteine-functionalized gold nanoparticles were employed to detect aqueous copper (Cu^{2+}) by changing solution color from red into blue [34]. This colorimetric nanosensor enables rapid, quantitative detection of Cu^{2+} with a sensitivity of 10^{-5} M. Likewise, based on mediated T-T base pairs at room temperature, a novel and practical colorimetric detection of Hg^{2+} was developed using 14 nm nanoparticles with sensitivity as low as 3.0 ppb of Hg^{2+} by unaided eye [35].

Numbers of optical sensors have been continuously established based on photoluminescent-quenching characteristics. A gold nanoparticle-rhodamine 6G-based fluorescent sensor was developed for sensing Hg^{2+} in aqueous solution with a detection limit of 0.012 ppb [36]. Similarly, photoluminescence-based assays were performed for monitoring level of Hg^{2+} (with sensitivity of 2.0 ppb) by the fact that Hg^{2+} concentration is directly proportional to photoluminescent intensity [37]. In addition, a homogeneous Cu^{2+} sensing assay was conducted based on photoluminescent-quenching between a perylene bisimide chromophore and gold nanoparticles in the presence of Cu^{2+} [38].

G-quadruplex-based DNAzymes, nucleic acid enzymes with peroxidase-like activity, were utilized for colorimetric and chemiluminescent detection of various metal ions in aqueous samples. In principle that Hg^{2+} -induced T-T base pair can stimulate appropriate folding of G-quadruplex DNAs but inhibit the DNAzyme activity, G-quadruplex-based DNAzymes were conducted for detecting aqueous Hg^{2+} with detection limit of 50 nM (10 ppb) [39].

A multiplex assay for detecting Hg^{2+} and silver (Ag^+) ions was developed using an electron-transfer-quenching path [40]. Hg^{2+} or Ag^+ ions could modify quantum dots by

inducing formation of T-T and C-C base pairs, respectively, resulting in colorless complexes of Hg^{2+} -thymine (T) or Ag^+ -cytosine (C) that cannot transfer energy from the quantum dots. Consequently, concentration of Hg^{2+} or Ag^+ ions is inversely proportional to photoluminescence intensity via electron-transfer quenching. Nevertheless, this assay was not sensitive enough for sensing such Hg^{2+} or Ag^+ ions. A more sensitive assay was thus developed for highly selective detection of Hg^{2+} ions (with detection limit of 5.0 nM), based on aggregation-mediated fluorescence quenching of 11-mercaptopundecanoic acid- (11-MUA-) protected gold nanoparticles in presence of 2,6-pyridinedicarboxylic acid [41]. The aggregation mainly occurred by interaction of Hg^{2+} ions with carboxylate groups on 11-MUA-protected gold nanoparticles [40].

Furthermore, nanoparticles can be effectively employed to detect small molecules (e.g., hydrogen, carbon dioxide, nitrogen oxide, oxygen, and ammonium ions). Contamination with nitrite (NO_2^-) ions from chemical fertilizers, livestock, and organic waste becomes environmental problem. The *in situ* precipitation of gold nanoparticles, a sensitive colorimetric assay for selective detection of nitrite and nitrate contaminants, was developed using gold nanoparticle probe functionalized with nitrite-reactive groups [42]. The 2,4,6-trinitrotoluene (TNT) compound is commonly used as nitroaromatic explosives for mining-related purposes and consequently contaminated into soil and ground water. This TNT compound can be detected by reaction between TNT and cysteine on the gold nanoparticle surface using so-called cysteine-modified gold nanoparticle-based surface enhanced Raman spectroscopy probe in label-free system [43]. In presence of TNT, a gold nanoparticle color becomes altered with a detection limit of 2 pM TNT in aqueous solution.

A fluorescence nanoparticles-based assay for rapid and selective nitrite detection was constituted which relied on nitrite-induced fluorescence quenching of the nanoparticles through a simple diazotization reaction [44]. Under optimal conditions, nitrite was quantitatively determined using organic fluorescence nanoparticles (namely, 1-aminopyrene nanoparticles) under linearity range of 20–1400 ng/mL with a correlation coefficient of 0.9987 and detection limit of 3 ng/mL nitrite in solution. For quantitative determination, this method for nitrite analysis can be applied to water samples.

In addition, gold nanorods can be incorporated into optical sensors for detecting bacterial pathogens. Coliform bacteria (e.g., *Escherichia coli*) contaminated in the environment is still a serious public health concern. Of necessity, a sensitive assay based on an antibody-conjugated gold nanorod was successfully constituted by using two-photon scattering technique for determining *E. coli*, with detection limit as low as 50 colony forming unit (CFU)/mL [45]. Using gold nanorod assemblies with basic side-by-side and end-to-end modalities, a rapid and sensitive detection method for microcystin-LR (MC-LR) containing two substitutions of leucine (Leu) and arginine (Arg) was further developed, with detection limit of 0.45 ng/mL and 5 pg/mL, respectively [46]. The assemblies with different geometries of MC-LR

were determined using adsorption spectroscopy and light scattering. Besides MC-LR, the measurable immunoassembly methods can be extensively utilized for detection of other various environmental toxins.

4.2. Nanoparticle-Based Electrochemical Sensors. Electrochemical sensors are of interest to sensor-focused research field. Several enzyme-based systems, similar to glucose sensor, were developed. Nanoparticle-based labels for analyte not only are useful for spectroscopic methods but are also applied in electrochemical detection. Since metal nanoparticles can be oxidized to form ions that are electrochemically detectable, electrochemical sensors thus were often utilized for screening environmental contaminants.

An electrochemical sensor for copper (Cu^{2+}) ions was accomplished with detection limit of less than 1 pM [47]. Electrodes were initially established with gold nanoparticles, and then the gold colloid surface was subsequently functionalized with cysteine for sensing Cu^{2+} ions. Single-walled carbon nanotubes (SWNTs) impregnating porous fibrous materials (e.g., fabrics and papers) were employed to render biosensors high performance [48]. SWNTs and antibodies were utilized to create paper-based sensors for sensitive and specific detection of MC-LR. A paper-based sensor was successfully employed to detect microcystin-LR (MC-LR) in Tai lake sample, with detection limit of 0.6 ppb and at least 28 times quicker response period in comparison to that obtained by an enzyme-linked immunosorbent assay [49]. This nanoparticle-based electrochemical sensing technology facilitates the preparation of several other sensitive environmental sensors. Additionally, a sensitive electrochemical immunosensor using analyte-functionalized single-walled carbon nanohorns was developed for detecting MC-LR in Tai lake water [50]. In competitive immunoassay format, the immunosensor using horseradish peroxidase-conjugated MC-LR antibodies showed broad spectrum response of linearity (0.05–20 $\mu\text{g}/\text{mL}$) with detection limit of 0.03 $\mu\text{g}/\text{mL}$. Such nanoparticle-based electrochemical sensing technology would improve prominent tool performance for detecting various pathogens and their potential toxins as well as for on-site monitoring of environmental pollutants.

4.3. Magnetic-Relaxation Sensors. Magnetic-relaxation sensors have been established based on the switching events between target analyte-induced aggregation and disaggregation of magnetic nanoparticles (MNPs). Biocompatible magnetic nanoparticles can serve as magnetic-relaxation switches (MRS) by generating spin-spin relaxation times of water T_2 signals and by resulting switches between dispersed and aggregated forms. Magnetic-relaxation switches-based methods evolve radiofrequency, hence being indifferent to light-based interference (e.g., scattering, absorption, or fluorescence) in fluids or tissues. Magnetic-relaxation switches-based sensing technology is used for detecting analytes, especially environmental toxins in various matrices. In relevance to radiofrequency, magnetic-relaxation switches-based assays enable sensing such complex and nonoptical matrices (e.g., multicomponent environmental samples, blood, or

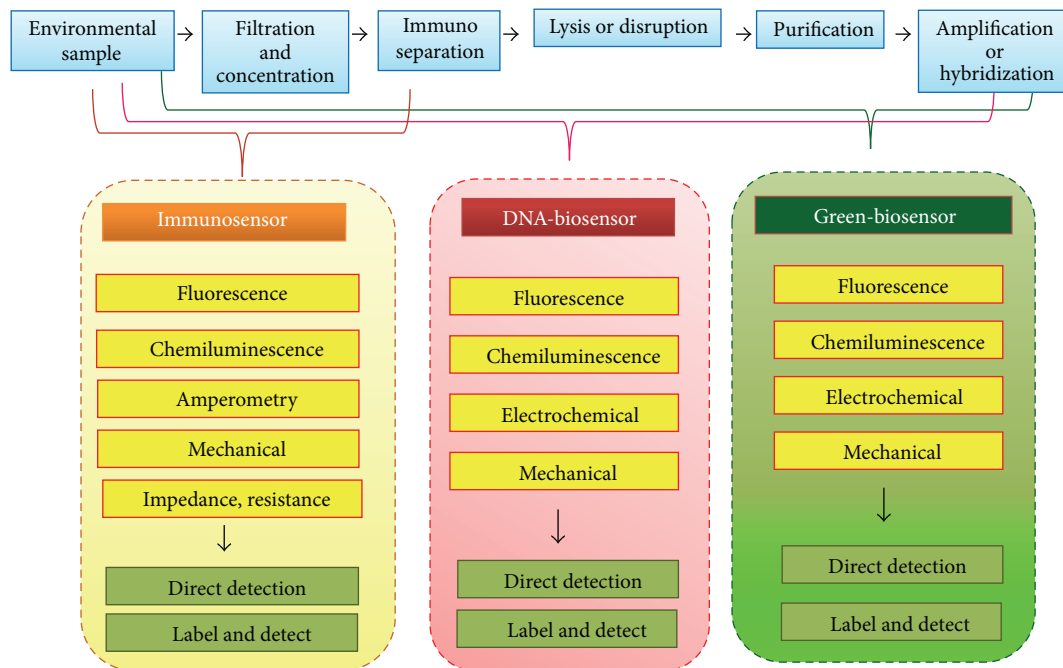


FIGURE 4: Common procedures for detection of certain water-borne pathogens in environmental matrices and progressive development of respective bionanosensors including immunosensor, DNA-based sensor, and others. Irrespectively, preprocessing steps of necessity initially require filtration and concentration, and then an immunoseparation step (e.g., immunomagnetic separation) in several types of assays.

culture media). Consequently, the handling capability with complex samples expedites multiple processing steps, relative to the traditional optical applications [51–54].

In addition, magnetic-relaxation switches-based methodologies provide advantages over similar detection tests *in vitro*. Specific and highly sensitive assays with the use of MRS sensors were able to quantitatively determine bacterial pathogens in environmental samples [55]. For sensing MC-LR residual, stable and sensitive immunosensors were successfully developed on basis of relaxation of magnetic nanoparticles [56]. By using antigen MC-LR conjugated magnetic nanoparticles, MC-LR specific antibodies can aggregate them into clustered forms in liquid media (Figure 3) [27]. In water sample, the MC-LR was quantitatively determined at range of 1–18 ppb with detection limit of 0.6 ppb. Due to advantage of magnetic-relaxation switches-based assay, it is regarded as a potential platform for rapid monitoring of hazardous pollutants in complex environmental samples and may extend its use of choices in wider fields [8].

5. Improvements for Environmental Nanobiosensors Regarding Bioreceptors

Recently, nucleic acid biosensor-based researches have been increasingly focused. Nucleic acid biosensors offer desirable sensitivity for detecting particularly water-borne pathogens even at low levels (Figure 4) [57, 58]. At diverging point, immunosensors (left panels) require only filtration, concentration, and detection while DNA biosensors (central panels) possibly need consecutive preprocessing of cellular component disruption, genetic material purification, and

often enzymatic amplification and/or hybridization. Aforementioned sensors can be established in either label-based or label-free detection system. Typical detection methods are exemplified in column boxes.

To improve efficacy of these biosensors, step of purification and concentration of pathogens of interest, followed by lysis step of several components (e.g., cell membrane, oocyst wall, spore coat, or viral capsid) and nucleic acid purification prior to amplification and detection, are required. Although market ready-to-use kits for these procedures (e.g., Qiagen's nucleic acid purification kits) are available, such preprocessing steps consume time. The assay procedures need to be simplified and shortened.

In respect to miniaturization, confining reaction within a micro- or nanoscale, fluidic panel has potential to shorten assay time using its higher diffusion ability [59] and to simplify assay steps by combining multiple operations together into micro total analysis systems (μ TAS) [60]. Microfluidic devices with sample preparation steps including immunoseparation and preconcentration have been accomplished for mRNA isolation [61], PCR-based amplification [62–65], and isothermal amplification reactions [66].

Of particular interest, immunosensors-based methods have proved to enhance sensitivity. Similar to PCR-based methods, these methods possess low detection limits toward detection of numerous pathogens but amplification step is unnecessary. This technology is promising due to the reduction of both assay time and complexity. For instance, biobarcode assays have been employed to accomplish signal amplification in *S. enterica* Enteritidis-sensing assays. A sandwich hybridization assay combining target-specific probe

coated-gold nanoparticles and fluorescein-labeled barcode DNA (a 1:100 ratio) with magnetic beads was achieved to detect 0.25 fmol target DNA [67]. The detection limit of this method is similar to that of using liposomal signal amplification in DNA-based sensors [68, 69]. Nevertheless, its sensitivity is insufficient to detect nonamplified target DNA. The use of multiple liposome-tagged probes in a rapid lateral flow assay was capable of selectively detecting 16S rRNA as a potential target as 80% of the total RNA (135 ng) in an intact bacterial cell, without enzymatic amplification within 20 minutes [70, 71]. This implies further potential utilization of liposome-based signal amplification.

Another method with use of up-converting phosphor technology (UPT) provides specific signals in assays without enzymatic amplification. Usually, UPT uses inorganic microcrystals that confer visible light emission when an infrared laser is excited, yielding specific signals with very low noise due to nonautofluorescent property [72]. PCR-based assays using these UPT-based molecules as reporters were achieved to detect low level of specific target DNA [73]. Moreover, amplification-free hybridization-based DNA assay using four probes (two labeled with biotin for capture of the specific target and two labeled with digoxigenin) and UPT-reporters labeled with an antidigoxigenin antibody was developed to detect *Streptococcus pneumoniae* [74]. With the utility of the multiple probes, this assay enables the detection of target genomic DNA at 1 ng or about 10^6 bacterial cells.

6. Future Perspectives with Advanced Nanotechnology

Of considerable interest, we summarize recent progress in environmental sensor-based research with “individual or combinatorial” uses of fluorescent nanoparticles and magnetic nanomaterials as environmental monitoring tool, and the utility of newly developed nanoparticles for detection of various environmental pollutants [75].

Due to facile synthetic processes of nanoparticles with desirable sizes and structures, this will definitely facilitate development of nanomaterial fabrication. Accordingly, nanocomposites comprising of discrete domains of different materials display novel physicochemical properties that will be important for wider applications in several fields, including environment. For instance, magnetic Fe_3O_4 nanoparticles with silica shell in $\text{Fe}_3\text{O}_4/\text{SiO}_2$ core-shell structures were synthesized. The $\text{Fe}_3\text{O}_4/\text{SiO}_2$ core-shell absorbed with gold nanoparticles by electrostatic adsorption to amino groups on the surface was established to form $\text{Fe}_3\text{O}_4/\text{SiO}_2/\text{Au}$ structures [76]. Composite core-shell nanostructures possessing optical, magnetic, catalytic, and surface plasmon resonance properties offer advantages over individual single-component materials.

Typically, environmental screening is constituted using instrumental analysis (e.g., thin layer chromatography (TLC) [77], high-pressure liquid chromatography (HPLC) [78, 79], gas chromatography-mass spectrometry (GC-MS) [80], liquid chromatography-mass spectrometry (LC-MS), and immunoassay [81–84]). TLC is a simple and economic

method for environmental contaminant determination but its sensitivity is low. Traditional instrument-based methods (e.g., HPLC, GC-MS, and LC-MS) are commonly applied for environmental pollutant measurement. However, they are cost- and time-ineffective due to complicated sample preparation [85]. Hence, these methods are inappropriate for routine monitoring of numerous samples. Nanoparticle-based sensors conferring sensitive and specific potential in possible portable platform offer advantages over traditional instrument analysis and enzyme-linked immunosorbent assay in more rapid results and higher throughputs.

Applications of nanoparticle-based sensors in widespread surveillance of environmental toxicants+ are due to their sensitivity, selectivity, speediness, and affordability. The detection of environmental pollutants with fewer steps is possible with nanoparticle-based sensors (e.g., optical and magnetic resonance sensors). Numerous nanosensors have been developed as portable devices. In addition, immune-chromatographic strip-based assays can be readout by unaided eyes. However, quantitative analysis of analytes usually needs an array scanner or similar instrumentation. Portable strip readers for quantitative dry-reagent strip sensors have been designed to assess the color intensity of membrane bands, enabling them for on-site detection [86–88]. On basis of magnetic nanomaterials, magnetic-relaxation sensing method can be undertaken using miniaturized diagnostic magnetic resonance systems containing planar microcoils, microfluidic channels, and a portable magnet [89]. This portable device has been established for rapid, quantitative, and multiplex measurement of multicomponent environmental samples with high sensitivity using smaller device [8].

In commercial setting, these technologies include immunomagnetic separation (IMS) with semiautomated procedure (TCS Biosciences Isolate System), immunofluorescence assay (FA) microscopy in antibodies-labeled well slide platform (Meridian Biosciences MERIFLUOR), cytometry using fluorescent cell labeling and laser scanning technology (highly-automated, ChemScan RDI Solid-Phase Cytometry, bioMérieux), and molecular biology- and PCR-based detection methods of target specific sequences (RT-PCR Detection Kits, CEERAM, and Norgen Biotek).

Advanced nanotechnology refers to the study of how nanotechnology can benefit the environment and hence aims for products and processes that are safe and energy efficient, reduce waste, and lessen greenhouse gas emissions. The so-called “green” nanotechnology is also about manufacturing processes that are economically and environmentally sustainable. Green nanotechnology is increasingly referred to in connection with other concepts such as green chemistry and sustainable and green engineering and manufacturing. This green nanotechnology enables advance development of nanotechnology to minimize potential environmental and human health risks associated with the manufacture and use of engineered-nanomaterial products and to encourage replacement of existing products with novel nanomaterial-based products that are more eco-friendly throughout their lifecycle.

Intriguingly, selective colorimetric assay with the use of green synthesized silver nanoparticles from plant extracts

has been recently developed for sensing toxic metal ions in aqueous solution across a wide pH range (2.0–11.0) [90]. The green silver nanoparticles were synthesized by coordinating metal with organic functional groups present in the plant extracts (e.g., fresh and sun-dried neem leaf, fresh and sun-dried mango leaf, green tea, and pepper seed). Fresh neem leaf extracts-based silver nanoparticles were selectively capable of detecting Hg^{2+} while sun-dried neem leaf extract-based silver nanoparticles were found to selectively determine Hg^{2+} and Pb^{2+} at micromolar concentrations. Neem bark extract-based silver nanoparticles displayed selective colorimetric sensing of Hg^{2+} and Zn^{2+} . Similarly, silver nanoparticles synthesized from mango leaf (fresh and sun-dried) and green tea extracts exhibited selective colorimetric sensing of Hg^{2+} and Pb^{2+} ions. Interestingly, pepper seed extracts-based silver nanoparticles showed selective colorimetric sensing properties toward Hg^{2+} , Pb^{2+} , and Zn^{2+} . These green synthesized silver nanoparticles offer versatility with use of plant extracts via green nanotechnology as well as applicability in environmental sensor, especially in decontamination of toxic metal ions over broad pH range.

Taken together, high-throughput and ultrasensitive detection nanotechnology provide effective screening methods for various environmental pollutants. Nanosensors offer potential advantages: sensing capability of microbial pathogens or chemical contaminants at very low levels, convenient handling as portable device for on-site screening or real-time monitoring, cost-, labor-, and time-effectiveness, and simultaneous multiplex detecting ability. Furthermore, advanced nanotechnology encourages a fresh way of designing new products, with the environment and sustainability in mind. This nanobiotechnology will further promote widespread applications in several fields, particularly in environmental monitoring. The benefits of nanotechnology have thus an important role in keeping the environmental health safer.

7. Concluding Remarks

Of global health concern, particular water-borne pathogens and other potential toxicants contaminated in environmental conditions are critical. Development of detection methods with sensitivity, selectivity, and speediness is urgently required for screening their occurrence in correspondence with safety regulations at clinically significant levels. This will promote for betterment of the public health and individual life quality. Even though nucleic acid-based biosensors have potential at sensing very low concentrations, they still require time-ineffective purification steps at upstream processes. Immunosensors need relatively fewer steps of sample preparation processes, giving rise to shorter assay time; however, antibodies of need are complicated and noneconomical. Using different signal amplification and background-reduction techniques coupled with the miniaturization with enhanced sensitivity, nucleic acid/antibody-based detection methods offer sensitive and selective tools for screening various forms of water-borne pathogens.

So far, current investigations have been focused on detection of pathogens in the actual environmental samples as well as on prerequisite of preprocessing steps. Combinatorial use of fluorescent nanoparticles and magnetic nanomaterials will facilitate miniaturization techniques, multiplex detection systems, and nanomaterials-based research for simultaneously sensing relevant pathogens in a specific environmental scenario. However, some artifacts relating to interfering substances, nonspecific binding, aggregation, and toxicity of such nanoparticles should be addressed prior to their full potential and implementation as biosensors. The significant advantage includes rapid results because the approach to increase signal rather than the target analytes has revolutionized the paradigm of detection.

Taken together, these methodologies conjugated with green nanotechnology will expedite potential existing methods that would offer sensitivity, specificity, speediness, robustness, and self-cleaning to complement or replace the typical standards as well as promote accessibility of safe drinking water and decrease the global health problem due to water-borne diseases, in particular. Taking care of environmental concerns up front pays back in long-term benefits.

Conflict of Interests

The authors declare that there is no conflict of interests regarding the publication of this paper.

Acknowledgments

This research was supported by a grant from the Faculty of Environment and Resource Studies, Mahidol University, and a 2557 Grant from Mahidol University, and National Research Council of Thailand (NRCT)/Thailand Research Funds (TRF). Additionally, this paper is supported by Korea Ministry of Environment as “The Eco-Innovation Project” (412-112-011).

References

- [1] K. A. Kvenvolden and C. K. Cooper, “Natural seepage of crude oil into the marine environment,” *Geo-Marine Letters*, vol. 23, no. 3-4, pp. 140–146, 2003.
- [2] G. Duan, Z. Zhang, J. Zhang, Y. Zhou, L. Yu, and Q. Yuan, “Evaluation of crude toxin and metabolite produced by *Helminthosporium gramineum* Rabenh for the control of rice sheath blight in paddy fields,” *Crop Protection*, vol. 26, no. 7, pp. 1036–1041, 2007.
- [3] F. Busetti, S. Badoer, M. Cuomo, B. Rubino, and P. Traverse, “Occurrence and removal of potentially toxic metals and heavy metals in the wastewater treatment plant of fusina (Venice, Italy),” *Industrial and Engineering Chemistry Research*, vol. 44, no. 24, pp. 9264–9272, 2005.
- [4] M. Auffan, J. Rose, J.-Y. Bottero, G. V. Lowry, J.-P. Jolivet, and M. R. Wiesner, “Towards a definition of inorganic nanoparticles from an environmental, health and safety perspective,” *Nature Nanotechnology*, vol. 4, no. 10, pp. 634–641, 2009.
- [5] J. Cheon and J.-H. Lee, “Synergistically integrated nanoparticles as multimodal probes for nanobiotechnology,” *Accounts of Chemical Research*, vol. 41, no. 12, pp. 1630–1640, 2008.

- [6] P. K. Jain, X. Huang, I. H. El-Sayed, and M. A. El-Sayed, "Noble metals on the nanoscale: optical and photothermal properties and some applications in imaging, sensing, biology, and medicine," *Accounts of Chemical Research*, vol. 41, no. 12, pp. 1578–1586, 2008.
- [7] J. Gao, H. Gu, and B. Xu, "Multifunctional magnetic nanoparticles: design, synthesis, and biomedical applications," *Accounts of Chemical Research*, vol. 42, no. 8, pp. 1097–1107, 2009.
- [8] C. Peng, Z. Li, Y. Zhu et al., "Simultaneous and sensitive determination of multiplex chemical residues based on multicolor quantum dot probes," *Biosensors and Bioelectronics*, vol. 24, no. 12, pp. 3657–3662, 2009.
- [9] P. Tuitemwong, N. Songvorawit, and K. Tuitemwong, "Facile and sensitive epifluorescent silica nanoparticles for the rapid screening of EHEC," *Journal of Nanomaterials*, vol. 2013, Article ID 706354, 8 pages, 2013.
- [10] H. Yu and J. G. Bruno, "Immunomagnetic-electrochemiluminescent detection of *Escherichia coli* O157 and *Salmonella typhimurium* in foods and environmental water samples," *Applied and Environmental Microbiology*, vol. 62, no. 2, pp. 587–592, 1996.
- [11] J. G. Bruno and H. Yu, "Immunomagnetic-electrochemiluminescent detection of *Bacillus anthracis* spores in soil matrices," *Applied and Environmental Microbiology*, vol. 62, no. 9, pp. 3474–3476, 1996.
- [12] X.-L. Su and Y. Li, "Quantum dot biolabeling coupled with immunomagnetic separation for detection of *Escherichia coli* O1517:H7," *Analytical Chemistry*, vol. 76, no. 16, pp. 4806–4810, 2004.
- [13] E. R. Goldman, A. R. Clapp, G. P. Anderson et al., "Multiplexed toxin analysis using four colors of quantum dot fluororeagents," *Analytical Chemistry*, vol. 76, no. 3, pp. 684–688, 2004.
- [14] J. A. Kloepfer, R. E. Mielke, M. S. Wong, K. H. Neelson, G. Stucky, and J. L. Nadeau, "Quantum dots as strain- and metabolism-specific microbiological labels," *Applied and Environmental Microbiology*, vol. 69, no. 7, pp. 4205–4213, 2003.
- [15] J. G. Bruno and J. L. Kiel, "Use of magnetic beads in selection and detection of biotoxin aptamers by electrochemiluminescence and enzymatic methods," *BioTechniques*, vol. 32, no. 1, pp. 178–180, 2002.
- [16] S. Dwarakanath, J. G. Bruno, A. Shastry et al., "Quantum dot-antibody and aptamer conjugates shift fluorescence upon binding bacteria," *Biochemical and Biophysical Research Communications*, vol. 325, no. 3, pp. 739–743, 2004.
- [17] M. Ikanovic, W. E. Rudzinski, J. G. Bruno et al., "Fluorescence assay based on aptamer-quantum dot binding to *Bacillus thuringiensis* spores," *Journal of Fluorescence*, vol. 17, no. 2, pp. 193–199, 2007.
- [18] S. B. Shinde, C. B. Fernandes, and V. B. Patravale, "Recent trends in *in-vitro* nanodiagnosics for detection of pathogens," *Journal of Controlled Release*, vol. 159, no. 2, pp. 164–180, 2012.
- [19] C. Kaittanis, S. Santra, and J. M. Perez, "Emerging nanotechnology-based strategies for the identification of microbial pathogenesis," *Advanced Drug Delivery Reviews*, vol. 62, no. 4–5, pp. 408–423, 2010.
- [20] J. Song, H. Kim, Y. Jang, and J. Jang, "Enhanced antibacterial activity of silver/polyrhodanine-composite-decorated silica nanoparticles," *ACS Applied Materials and Interfaces*, vol. 5, no. 22, pp. 11563–11568, 2013.
- [21] M. N. Velasco-Garcia, "Optical biosensors for probing at the cellular level: a review of recent progress and future prospects," *Seminars in Cell and Developmental Biology*, vol. 20, no. 1, pp. 27–33, 2009.
- [22] T. Vo-Dinh, "Nanosensing at the single cell level," *Spectrochimica Acta B*, vol. 63, no. 2, pp. 95–103, 2008.
- [23] M. S. Thakur and K. V. Ragavan, "Biosensors in food processing," *Journal of Food Science and Technology*, vol. 50, no. 4, pp. 625–641, 2013.
- [24] A. P. F. Turner, I. Karube, and G. S. Wilson, *Biosensors: Fundamentals and Applications*, Oxford University Press, New York, NY, USA, 1987.
- [25] T. H. Rider, M. S. Petrovick, F. E. Nargi et al., "A B cell-based sensor for rapid identification of pathogens," *Science*, vol. 301, no. 5630, pp. 213–215, 2003.
- [26] S. K. Arya, A. Singh, R. Naidoo, P. Wu, M. T. McDermott, and S. Evoy, "Chemically immobilized T4-bacteriophage for specific *Escherichia coli* detection using surface plasmon resonance," *Analyst*, vol. 136, no. 3, pp. 486–492, 2011.
- [27] L. Wang, W. Ma, L. Xu et al., "Nanoparticle-based environmental sensors," *Materials Science and Engineering R*, vol. 70, no. 3–6, pp. 265–274, 2010.
- [28] H. Uzawa, K. Ohga, Y. Shinozaki et al., "A novel sugar-probe biosensor for the deadly plant proteinous toxin, ricin," *Biosensors and Bioelectronics*, vol. 24, no. 4, pp. 923–927, 2008.
- [29] B.-H. Liu, Z.-J. Tsao, J.-J. Wang, and F.-Y. Yu, "Development of a monoclonal antibody against ochratoxin A and its application in enzyme-linked immunosorbent assay and gold nanoparticle immunochromatographic strip," *Analytical Chemistry*, vol. 80, no. 18, pp. 7029–7035, 2008.
- [30] X.-H. Wang, T. Liu, N. Xu, Y. Zhang, and S. Wang, "Enzyme-linked immunosorbent assay and colloidal gold immunoassay for ochratoxin A: investigation of analytical conditions and sample matrix on assay performance," *Analytical and Bioanalytical Chemistry*, vol. 389, no. 3, pp. 903–911, 2007.
- [31] W. B. O. Shim, K. Y. Kim, and D. H. Chung, "Development and validation of a gold nanoparticle immunochromatographic assay (ICG) for the detection of zearalenone," *Journal of Agricultural and Food Chemistry*, vol. 57, no. 10, pp. 4035–4041, 2009.
- [32] W.-B. Shim, Z.-Y. Yang, J.-S. Kim et al., "Development of immunochromatography strip-test using nanocolloidal gold-antibody probe for the rapid detection of aflatoxin B1 in grain and feed samples," *Journal of Microbiology and Biotechnology*, vol. 17, no. 10, pp. 1629–1637, 2007.
- [33] G. K. Darbha, A. K. Singh, U. S. Rai, E. Yu, H. Yu, and P. C. Ray, "Selective detection of mercury (II) ion using nonlinear optical properties of gold nanoparticles," *Journal of the American Chemical Society*, vol. 130, no. 25, pp. 8038–8043, 2008.
- [34] W. Yang, J. J. Gooding, Z. He, Q. Li, and G. Chen, "Fast colorimetric detection of copper ions using L-cysteine functionalized gold nanoparticles," *Journal of Nanoscience and Nanotechnology*, vol. 7, no. 2, pp. 712–716, 2007.
- [35] X. Xue, F. Wang, and X. Liu, "One-step, room temperature, colorimetric detection of mercury (Hg^{2+}) using DNA/nanoparticle conjugates," *Journal of the American Chemical Society*, vol. 130, no. 11, pp. 3244–3245, 2008.
- [36] J. Chen, A. Zheng, A. Chen et al., "A functionalized gold nanoparticles and Rhodamine 6G based fluorescent sensor for high sensitive and selective detection of mercury(II) in environmental water samples," *Analytica Chimica Acta*, vol. 599, no. 1, pp. 134–142, 2007.
- [37] C. C. Huang and H. T. Chang, "Selective gold-nanoparticle-based "turn-on" fluorescent sensors for detection of mercury(II)

- in aqueous solution,” *Analytical Chemistry*, vol. 78, no. 24, pp. 8332–8338, 2006.
- [38] X. He, H. Liu, Y. Li et al., “Gold nanoparticle-based fluorometric and colorimetric sensing of copper(II) ions,” *Advanced Materials*, vol. 17, no. 23, pp. 2811–2815, 2005.
- [39] T. Li, S. Dong, and E. Wang, “Label-free colorimetric detection of aqueous mercury ion (Hg^{2+}) using Hg^{2+} -modulated G-quadruplex-based dnzymes,” *Analytical Chemistry*, vol. 81, no. 6, pp. 2144–2149, 2009.
- [40] R. Freeman, T. Finder, and I. Willner, “Multiplexed analysis of Hg^{2+} and Ag^+ ions by nucleic acid functionalized CdSe/ZnS quantum dots and their use for logic gate operations,” *Angewandte Chemie*, vol. 48, no. 42, pp. 7818–7821, 2009.
- [41] C.-C. Huang, Z. Yang, K.-H. Lee, and H.-T. Chang, “Synthesis of highly fluorescent gold nanoparticles for sensing mercury(II),” *Angewandte Chemie*, vol. 46, no. 36, pp. 6824–6828, 2007.
- [42] W. L. Daniel, M. S. Han, J.-S. Lee, and C. A. Mirkin, “Colorimetric nitrite and nitrate detection with gold nanoparticle probes and kinetic end points,” *Journal of the American Chemical Society*, vol. 131, no. 18, pp. 6362–6363, 2009.
- [43] S. S. R. Dasary, A. K. Singh, D. Senapati, H. Yu, and P. C. Ray, “Gold nanoparticle based label-free SERS probe for ultrasensitive and selective detection of trinitrotoluene,” *Journal of the American Chemical Society*, vol. 131, no. 38, pp. 13806–13812, 2009.
- [44] L. Wang, L. Dong, G.-R. Bian, L.-Y. Wang, T.-T. Xia, and H.-Q. Chen, “Using organic nanoparticle fluorescence to determine nitrite in water,” *Analytical and Bioanalytical Chemistry*, vol. 382, no. 5, pp. 1300–1303, 2005.
- [45] A. K. Singh, D. Senapati, S. Wang et al., “Gold nanorod based selective identification of *Escherichia coli* bacteria using two-photon rayleigh scattering spectroscopy,” *ACS Nano*, vol. 3, no. 7, pp. 1906–1912, 2009.
- [46] L. Wang, Y. Zhu, L. Xu et al., “Side by side and end to end gold nanorod assemblies for environmental toxin sensing,” *Angewandte Chemie International Edition*, vol. 49, no. 32, pp. 5472–5475, 2010.
- [47] J. J. Gooding, J. Shein, and L. M. H. Lai, “Using nanoparticle aggregation to give an ultrasensitive amperometric metal ion sensor,” *Electrochemistry Communications*, vol. 11, no. 10, pp. 2015–2018, 2009.
- [48] B. S. Shim, W. Chen, C. Doty, C. L. Xu, and N. A. Kotov, “Smart electronic yarns and wearable fabrics for human biomonitoring made by carbon nanotube coating with polyelectrolytes,” *Nano Letters*, vol. 8, no. 12, pp. 4151–4157, 2008.
- [49] L. Wang, W. Chen, D. Xu et al., “Simple, rapid, sensitive, and versatile SWNT-paper sensor for environmental toxin detection competitive with ELISA,” *Nano Letters*, vol. 9, no. 12, pp. 4147–4152, 2009.
- [50] J. Zhang, J. Lei, C. Xu, L. Ding, and H. Ju, “Carbon nanohorn sensitized electrochemical immunosensor for rapid detection of microcystin-LR,” *Analytical Chemistry*, vol. 82, no. 3, pp. 1117–1122, 2010.
- [51] T. J. Lowery, R. Palazzolo, S. M. Wong, P. J. Prado, and S. Taktak, “Single-coil, multisample, proton relaxation method for magnetic relaxation switch assays,” *Analytical Chemistry*, vol. 80, no. 4, pp. 1118–1123, 2008.
- [52] E. Y. Sun, R. Weissleder, and L. Josephson, “Continuous analyte sensing with magnetic nanoswitches,” *Small*, vol. 2, no. 10, pp. 1144–1147, 2006.
- [53] K. Aurich, S. Nagel, G. Glöckl, and W. Weitschies, “Determination of the magneto-optical relaxation of magnetic nanoparticles as a homogeneous immunoassay,” *Analytical Chemistry*, vol. 79, no. 2, pp. 580–586, 2007.
- [54] G. Y. Kim, L. Josephson, R. Langer, and M. J. Cima, “Magnetic relaxation switch detection of human chorionic gonadotrophin,” *Bioconjugate Chemistry*, vol. 18, no. 6, pp. 2024–2028, 2007.
- [55] C. Kaittanis, S. A. Naser, and J. M. Perez, “One-step, nanoparticle-mediated bacterial detection with magnetic relaxation,” *Nano Letters*, vol. 7, no. 2, pp. 380–383, 2007.
- [56] W. Ma, W. Chen, R. R. Qiao et al., “Rapid and sensitive detection of microcystin by immunosensor based on nuclear magnetic resonance,” *Biosensors and Bioelectronics*, vol. 25, no. 1, pp. 240–243, 2009.
- [57] M. Taniuchi, J. J. Verweij, Z. Noor et al., “High throughput multiplex PCR and probe-based detection with luminex beads for seven intestinal parasites,” *The American Journal of Tropical Medicine and Hygiene*, vol. 84, no. 2, pp. 332–337, 2011.
- [58] J. T. Connelly, S. R. Nugen, W. Borejsza-Wysocki, R. A. Durst, R. A. Montagna, and A. J. Baeumner, “Human pathogenic *Cryptosporidium* species bioanalytical detection method with single oocyst detection capability,” *Analytical and Bioanalytical Chemistry*, vol. 391, no. 2, pp. 487–495, 2008.
- [59] K. A. Heyries, M. G. Loughran, D. Hoffmann, A. Homsy, L. J. Blum, and C. A. Marquette, “Microfluidic biochip for chemiluminescent detection of allergen-specific antibodies,” *Biosensors and Bioelectronics*, vol. 23, no. 12, pp. 1812–1818, 2008.
- [60] D. R. Reyes, D. Iossifidis, P.-A. Aurox, and A. Manz, “Micro total analysis systems. 1. Introduction, theory, and technology,” *Analytical Chemistry*, vol. 74, no. 12, pp. 2623–2636, 2002.
- [61] S. R. Nugen, P. J. Asiello, and A. J. Baeumner, “Design and fabrication of a microfluidic device for near-single cell mRNA isolation using a copper hot embossing master,” *Microsystem Technologies*, vol. 15, no. 3, pp. 477–483, 2009.
- [62] C. Zhang and D. Xing, “Miniaturized PCR chips for nucleic acid amplification and analysis: latest advances and future trends,” *Nucleic Acids Research*, vol. 35, no. 13, pp. 4223–4237, 2007.
- [63] C. Zhang, J. Xu, W. Ma, and W. Zheng, “PCR microfluidic devices for DNA amplification,” *Biotechnology Advances*, vol. 24, no. 3, pp. 243–284, 2006.
- [64] K. Sun, A. Yamaguchi, Y. Ishida, S. Matsuo, and H. Misawa, “A heater-integrated transparent microchannel chip for continuous-flow PCR,” *Sensors and Actuators B: Chemical*, vol. 84, no. 2-3, pp. 283–289, 2002.
- [65] P. J. Obeid, T. K. Christopoulos, H. J. Crabtree, and C. J. Backhouse, “Microfabricated device for DNA and RNA amplification by continuous-flow polymerase chain reaction and reverse transcription-polymerase chain reaction with cycle number selection,” *Analytical Chemistry*, vol. 75, no. 2, pp. 288–295, 2003.
- [66] P. J. Asiello and A. J. Baeumner, “Miniaturized isothermal nucleic acid amplification, a review,” *Lab on a Chip—Miniaturisation for Chemistry and Biology*, vol. 11, no. 8, pp. 1420–1430, 2011.
- [67] D. Zhang, D. J. Carr, and E. C. Alocilja, “Fluorescent barcode DNA assay for the detection of *Salmonella enterica* serovar Enteritidis,” *Biosensors and Bioelectronics*, vol. 24, no. 5, pp. 1377–1381, 2009.
- [68] V. N. Goral, N. V. Zaytseva, and A. J. Baeumner, “Electrochemical microfluidic biosensor for the detection of nucleic acid

- sequences," *Lab on a Chip: Miniaturisation for Chemistry and Biology*, vol. 6, no. 3, pp. 414–421, 2006.
- [69] N. V. Zaytseva, R. A. Montagna, and A. J. Baeumner, "Microfluidic biosensor for the serotype-specific detection of dengue virus RNA," *Analytical Chemistry*, vol. 77, no. 23, pp. 7520–7527, 2005.
- [70] T. A. Brown, *Genomes 3*, Garland Science, New York, NY, USA, 3rd edition, 2007.
- [71] S. R. Nugen, B. Leonard, and A. J. Baeumner, "Application of a unique server-based oligonucleotide probe selection tool toward a novel biosensor for the detection of *Streptococcus pyogenes*," *Biosensors and Bioelectronics*, vol. 22, no. 11, pp. 2442–2448, 2007.
- [72] H. J. M. A. A. Zijlmans, J. Bonnet, J. Burton et al., "Detection of cell and tissue surface antigens using up-converting phosphors: a new reporter technology," *Analytical Biochemistry*, vol. 267, no. 1, pp. 30–36, 1999.
- [73] P. Corstjens, M. Zuiderwijk, A. Brink et al., "Use of up-converting phosphor reporters in lateral-flow assays to detect specific nucleic acid sequences: a rapid, sensitive DNA test to identify human papilloma-virus type 16 infection," *Clinical Chemistry*, vol. 47, no. 10, pp. 1885–1893, 2001.
- [74] M. Zuiderwijk, H. J. Tanke, R. S. Niedbala, and P. L. A. M. Corstjens, "An amplification-free hybridization-based DNA assay to detect *Streptococcus pneumoniae* utilizing the up-converting phosphor technology," *Clinical Biochemistry*, vol. 36, no. 5, pp. 401–403, 2003.
- [75] J. T. Connelly and A. J. Baeumner, "Biosensors for the detection of waterborne pathogens," *Analytical and Bioanalytical Chemistry*, vol. 402, no. 1, pp. 117–127, 2012.
- [76] W. Chen, N. Xu, L. Xu et al., "Multifunctional magnetoplasmonic nanoparticle assemblies for cancer therapy and diagnostics (Theranostics)," *Macromolecular Rapid Communications*, vol. 31, no. 2, pp. 228–236, 2010.
- [77] J. Stroka, R. V. Otterdijk, and E. Anklam, "Immunoaffinity column clean-up prior to thin-layer chromatography for the determination of aflatoxins in various food matrices," *Journal of Chromatography A*, vol. 904, no. 2, pp. 251–256, 2000.
- [78] E. Calleri, G. Marrubini, G. Brusotti, G. Massolini, and G. Caccialanza, "Development and integration of an immunoaffinity monolithic disk for the on-line solid-phase extraction and HPLC determination with fluorescence detection of aflatoxin B1 in aqueous solutions," *Journal of Pharmaceutical and Biomedical Analysis*, vol. 44, no. 2, pp. 396–403, 2007.
- [79] H. U. Yan-Yun, P. Zheng, Z.-X. Zhang, and H. E. You-Zhao, "Determination of aflatoxins in high-pigment content samples by matrix solid-phase dispersion and high-performance liquid chromatography," *Journal of Agricultural and Food Chemistry*, vol. 54, no. 12, pp. 4126–4130, 2006.
- [80] T. Tanaka, A. Yoneda, S. Inoue, Y. Sugiura, and Y. Ueno, "Simultaneous determination of trichothecene mycotoxins and zearalenone in cereals by gas chromatography-mass spectrometry," *Journal of Chromatography A*, vol. 882, no. 1-2, pp. 23–28, 2000.
- [81] A. Korde, U. Pandey, S. Banerjee et al., "Development of a radioimmunoassay procedure for aflatoxin B1 measurement," *Journal of Agricultural and Food Chemistry*, vol. 51, no. 4, pp. 843–846, 2003.
- [82] N. A. Lee, S. Wang, R. D. Allan, and I. R. Kennedy, "A rapid aflatoxin B1 ELISA: development and validation with reduced matrix effects for peanuts, corn, pistachio, and soybeans," *Journal of Agricultural and Food Chemistry*, vol. 52, no. 10, pp. 2746–2755, 2004.
- [83] S. Lipigorngoson, P. Limtrakul, M. Suttajit, and T. Yoshizawa, "In-house direct cELISA for determining aflatoxin B1 in Thai corn and peanuts," *Food Additives and Contaminants*, vol. 20, no. 9, pp. 838–845, 2003.
- [84] D. Nilüfer and D. Boyacıoğlu, "Comparative study of three different methods for the determination of aflatoxins in tahini," *Journal of Agricultural and Food Chemistry*, vol. 50, no. 12, pp. 3375–3379, 2002.
- [85] K. T. Devi, M. A. Mayo, K. L. N. Reddy et al., "Production and characterization of monoclonal antibodies for aflatoxin B1," *Letters in Applied Microbiology*, vol. 29, no. 5, pp. 284–288, 1999.
- [86] H. Xu, X. Mao, Q. Zeng, S. Wang, A.-N. Kawde, and G. Liu, "Aptamer-functionalized gold nanoparticles as probes in a dry-reagent strip biosensor for protein analysis," *Analytical Chemistry*, vol. 81, no. 2, pp. 669–675, 2009.
- [87] X. Mao, Y. Ma, A. Zhang, L. Zhang, L. Zeng, and G. Liu, "Disposable nucleic acid biosensors based on gold nanoparticle probes and lateral flow strip," *Analytical Chemistry*, vol. 81, no. 4, pp. 1660–1668, 2009.
- [88] H. Xie, W. Ma, L. Liu et al., "Development and validation of an immunochromatographic assay for rapid multi-residues detection of cepheids in milk," *Analytica Chimica Acta*, vol. 634, no. 1, pp. 129–133, 2009.
- [89] H. Lee, E. Sun, D. Ham, and R. Weissleder, "Chip-NMR biosensor for detection and molecular analysis of cells," *Nature Medicine*, vol. 14, no. 8, pp. 869–874, 2008.
- [90] D. Karthiga and S. P. Anthony, "Selective colorimetric sensing of toxic metal cations by green synthesized silver nanoparticles over a wide pH range," *RSC Advances*, vol. 3, no. 37, pp. 16765–16774, 2013.

Research Article

Self-Consolidation Mechanism of Nanostructured Ti_5Si_3 Compact Induced by Electrical Discharge

W. H. Lee,¹ Y. W. Cheon,¹ Y. H. Jo,¹ J. G. Seong,¹ Y. J. Jo,¹ Y. H. Kim,² M. S. Noh,³
H. G. Jeong,³ C. J. Van Tyne,⁴ and S. Y. Chang⁵

¹Faculty of Nanotechnology and Advanced Materials Engineering, Sejong University, Seoul 143-747, Republic of Korea

²Department of Dental Laboratory Technology, Wonkwang Health Science University, Iksan 570-750, Republic of Korea

³Center for SCINOVATOR, Posung High School, Seoul 138-829, Republic of Korea

⁴Department of Metallurgical and Materials Engineering, Colorado School of Mines, Golden, CO 80401, USA

⁵Department of Materials Engineering, Korea Aerospace University, Goyang-si 412-791, Republic of Korea

Correspondence should be addressed to S. Y. Chang; sychang@kau.ac.kr

Received 30 August 2014; Revised 26 October 2014; Accepted 27 October 2014

Academic Editor: Xiao-Feng Zhao

Copyright © 2015 W. H. Lee et al. This is an open access article distributed under the Creative Commons Attribution License, which permits unrestricted use, distribution, and reproduction in any medium, provided the original work is properly cited.

Electrical discharge using a capacitance of 450 μ F at 7.0 and 8.0 kJ input energies was applied to mechanical alloyed Ti_5Si_3 powder without applying any external pressure. A solid bulk of nanostructured Ti_5Si_3 with no compositional deviation was obtained in times as short as 159 μ sec by the discharge. During an electrical discharge, the heat generated is the required parameter possibly to melt the Ti_5Si_3 particles and the pinch force can pressurize the melted powder without allowing the formation of pores. Followed rapid cooling preserved the nanostructure of consolidated Ti_5Si_3 compact. Three stepped processes during an electrical discharge for the formation of nanostructured Ti_5Si_3 compact are proposed: (a) a physical breakdown of the surface oxide of Ti_5Si_3 powder particles, (b) melting and condensation of Ti_5Si_3 powder by the heat and pinch pressure, respectively, and (c) rapid cooling for the preservation of nanostructure. Complete conversion yielding a single phase Ti_5Si_3 is primarily dominated by the solid-liquid mechanism.

1. Introduction

Syntheses of intermetallic compounds with high melting points via mechanical alloying have been attempted in numerous studies [1, 2]. In general, combustion reactions have been initiated by ball milling in a variety of highly exothermic reaction mixtures. The formation of intermetallics from their elemental components accelerates during ball milling to become a self-sustaining high temperature reaction [3, 4]. Among intermetallic compounds, Ti_5Si_3 has attracted more interest recently because a number of their properties have potential in materials applications. Characteristics which make them promising high temperature structural materials include low temperature toughness, high temperature strength and creep resistance, oxidation resistance, and relatively low density [5, 6]. There are various ways to improve the fracture toughness of Ti_5Si_3 , such as reduction of grain size and alloying with other elements [7–9].

Conventionally, a solid bulk typed Ti_5Si_3 can be synthesized by reacting mixed stoichiometric powders of Ti and Si at higher temperature or arc melting of Ti and Si pieces [10, 11]. In spite of their research significance, in recent years there have been relatively few studies on the consolidation of Ti_5Si_3 in the form of powder. The usual sequence in powder metallurgy operations is to compact a metal powder in a die at room temperature and subsequently sinter it at elevated temperatures. Not only are high pressure, high temperature, and long times required, but in the case of reactive materials, such as Ti and its alloys, an inert atmosphere is also inevitably required. The high temperatures involved in these processes, however, result in detrimental changes in the microstructure and mechanical properties.

Lee and coworkers reported that Ti, Ti-6Al-4V, and Ti_5Si_3 powders can be successfully consolidated into a solid bulk type without detrimental changes in the microstructure and mechanical properties by using an electrical discharge

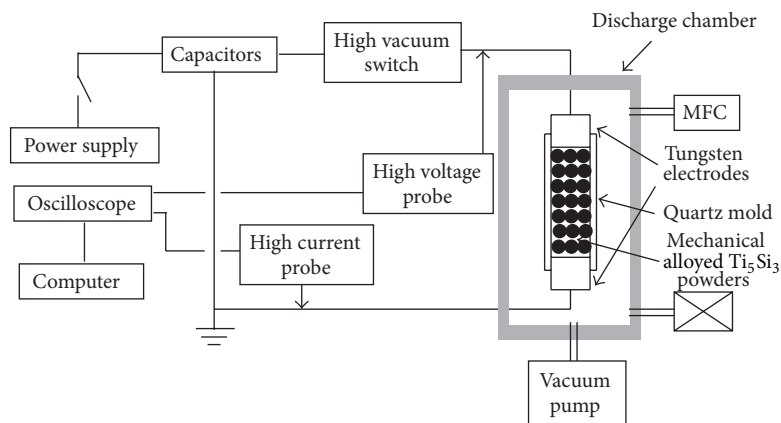


FIGURE 1: A schematic diagram of the experimental setup for the electrical discharge consolidation (EDC) technique.

technique [12–15]. However, the formation of nanostructured Ti₅Si₃ compact by the discharge has not been reported.

This paper thus analyzes the electrical discharge characteristics in terms of input energy, capacitance, and discharge time. It also systematically describes means by which the electrical discharge consolidates the mechanical alloyed Ti₅Si₃ powder particles to produce a solid compact with a nanostructure.

2. Materials and Methods

Elemental Ti and Si powders were mechanically alloyed (MAed) for 30 minutes at a fixed rpm of 1200 in an Ar atmosphere using a high speed Spex 8000D mixer/mill (SPEX Industries, Inc.) and a cylindrical partially stabilized zirconia (PSZ) vial (60 mm i.d. and 87 mm long) with high Cr hardened steel balls (10.0 and 4.7 mm in diameter). The charged atomic ratio of the reactants corresponded to the reaction stoichiometry (Ti-37.5 at.% Si). The purity of the powders was better than 99.95%. The mass of the powder charge was 10 g and the mass ratio of ball to powder was 5 : 1.

MAed powder without any surface treatment was mounted on the spectrometer probe tip by means of double-sided adhesive tape and examined by XPS (X-ray photoelectron microscopy) for any possible surface modification. Under the current conditions employed, the full width at half maximum (FWHM) of the Ag 3d_{5/2} peak was 1.1 eV, and the binding energy difference between Ag 3d_{5/2} and Ag 3d_{3/2} was 6.0 eV. When the Ag 3d_{5/2} peak was used as the reference peak, the binding energy of the C1s peak of adventitious carbon on the standard silver surface was 285 eV. All binding energies were referenced to the C1s peak to correct for sample charging.

0.34 grams of MAed powder was vibrated into a quartz tube with an inner diameter of 4.0 mm that had a tungsten electrode at the bottom and top. The discharging chamber was evacuated to 2×10^{-2} torr. A capacitor bank of 450 μ F was charged with two different electrical input energies (7.0 and 8.0 kJ). The charged capacitor bank instantaneously discharged through the MAed powder column without applying any pressure by on/off high vacuum switch which

closes the discharge circuit. The voltage and current that the powder column experiences when the circuit is closed were simultaneously picked up by a high voltage probe and a high current probe, respectively. Outputs from these probes are fed into a high speed oscilloscope that stores them as a function of discharge time. The overall process is referred to as electrical discharge consolidation (EDC). A schematic of the EDC apparatus is shown in Figure 1.

The phase compositions of the MAed powder and EDC compacts were investigated by X-ray diffraction (XRD) using Cu K _{α} radiation. Each EDC compact was sliced every two millimeters and the resulting cross-sections were examined under scanning electron microscopy (SEM) and transmission electron microscopy (TEM). The average hardness values were obtained from at least 20 measurements on the cross-sections of each sample.

3. Results and Discussion

Figure 2(a) shows SEM micrograph of the MAed powder with a mean particle size of 3.4 μ m, which was used in current experiment. XRD patterns of the powder, shown in Figure 2(b), confirmed that the powder is mainly composed of Ti₅Si₃ phase.

To investigate the surface chemical states of MAed Ti₅Si₃ powder, XPS was carried out. Figure 3(a) shows narrow scan spectra of the Ti 2p region before and after light Ar⁺ etching for 5 minutes. For the MAed Ti₅Si₃ powder before etching, a Ti 2p_{3/2} peak at 459.2 eV is shown, with 5.8 eV splitting between the Ti 2p_{1/2} and Ti 2p_{3/2} peaks. The Ti 2p_{3/2} peak at 459.2 eV corresponds to TiO_x, implying that the surface of MAed Ti₅Si₃ powder is primarily in the form of titanium oxide [16, 17]. However, after etching the MAed Ti₅Si₃ powder, the Ti 2p_{3/2} peak shifted to lower binding energy, 453.4 eV, which indicates the presence of titanium silicide [18]. It can thus be known that the MAed Ti₅Si₃ powder was lightly oxidized. Figure 3(b) shows narrow scan spectra of the Si 2p region before and after light Ar⁺ etching for 5 minutes. For the MAed Ti₅Si₃ powder before etching, a Si 2p peak at 102.5 eV corresponds to SiO_x [18]. After etching the MAed Ti₅Si₃ powder, the Si 2p peak shifted to

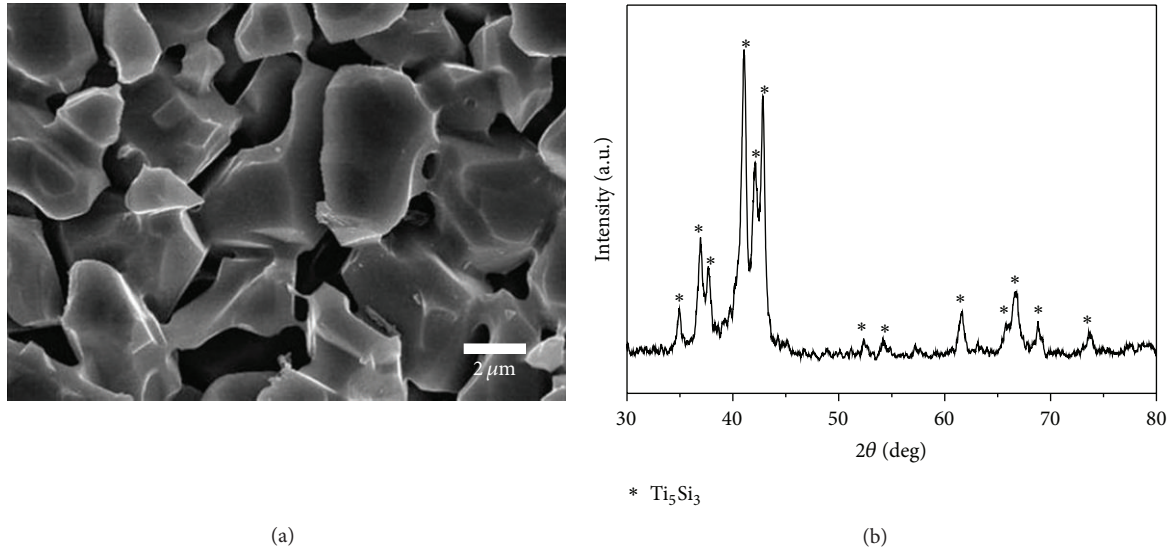


FIGURE 2: (a) SEM micrograph and (b) XRD patterns of MAed Ti-37.5 at.% Si powder mixture.

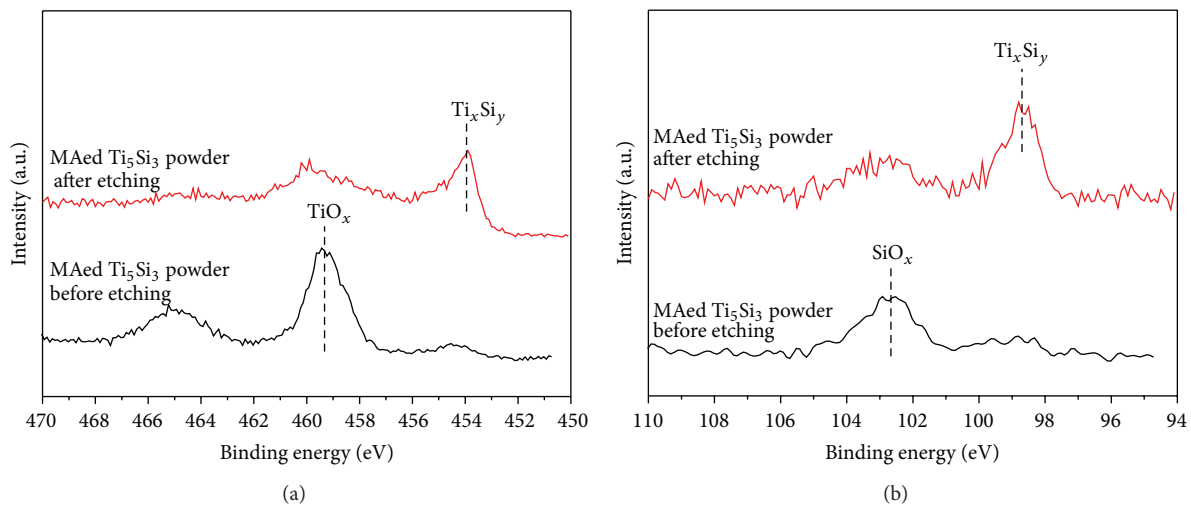


FIGURE 3: XPS narrow scan spectra of the (a) Ti 2p and (b) Si 2p region of MAed Ti₅Si₃ powder before and after light Ar⁺ etching for 5 minutes.

lower binding energy, 98.2 eV, which indicates the presence of titanium silicide [18]. This result also supports that the MAed Ti₅Si₃ powder was lightly oxidized.

The MAed Ti₅Si₃ powder was consolidated by a conventional hot-pressing process. As shown in Figure 4(a), the consolidation process at 1200°C in a vacuum of 2×10^{-6} torr for two hours by applying a pressure of 10 tons did not successfully produce the compact in a bulk type, resulting in the formation of a porous structure. As listed in Table 1, the hardness of MAed Ti₅Si₃ powder was found to be about Hv 1120, but that of the hot-pressed Ti₅Si₃ compact decreased down to Hv 800. The decreased hardness can be attributed to the release of strain energy during a hot-pressing and also to the porous structure of the compact. The cross-section views of EDC Ti₅Si₃ compacts at the input energy of 7.0 and 8.0 kJ are shown in Figures 4(b) and 4(c), respectively.

The compacts were composed of powder particles that were completely deformed and welded together by the electrical discharge. The density of the solid core of EDC Ti₅Si₃ compacts is approximately ~99% of theoretical value. From XRD patterns of the EDC Ti₅Si₃ compacts as shown in Figure 5, only peaks corresponding to the phase of Ti₅Si₃ have been found. It can be known that the unique phase of Ti₅Si₃ has not been altered by the electrical discharge process. The average crystallite size of EDC Ti₅Si₃ compacts was determined as 93–101 nm by using Suryanarayana and Grant Norton's formula [19]. Measured hardness of EDC Ti₅Si₃ compacts is also listed in Table 1, indicating that the hardness can be increased by the electrical discharge.

Figure 6 shows a typical TEM bright-field image (a) and selected area diffraction patterns ((b) and (c)) of the EDC Ti₅Si₃ compact discharged at 7.0 kJ of input energy [13].

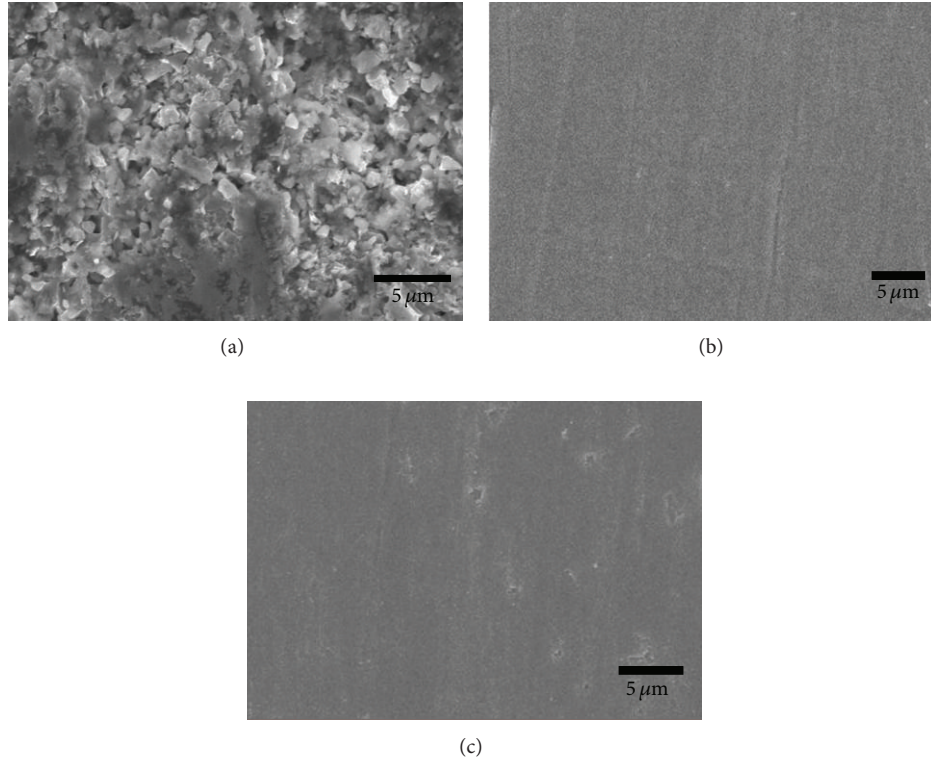


FIGURE 4: SEM micrographs of the cross-sections of consolidated Ti_5Si_3 compacts obtained by (a) hot-pressing at 1200°C in a vacuum of 2×10^{-6} torr for two hours with a pressure of 10 tons and electrical discharge consolidation using (b) 7.0 kJ and (c) 8.0 kJ of input energy.

TABLE 1: Microhardness of MAed Ti_5Si_3 powder, hot-pressed Ti_5Si_3 compact, and EDC Ti_5Si_3 compacts.

MAed Ti_5Si_3 powder	Hot-pressed Ti_5Si_3 compact	EDC Ti_5Si_3 compact	
		Input energy	
		7.0 kJ	8.0 kJ
Hv 1120	Hv 800	Hv 1410	Hv 1450

TEM bright-field image in Figure 6(a) presents the facet grain boundary, which is quite flat suggesting that the grain boundaries of the Ti_5Si_3 compound are quite stable. The diffraction peaks in Figures 6(b) and 6(c) correspond to [001] and [100] zone axis of hexagonal Ti_5Si_3 compound ($P6_3/mcm$), respectively. Based on the analysis of the diffraction patterns, a value of the lattice parameter for the EDC Ti_5Si_3 compact can be calculated as $a = 7.42 \text{ \AA}$ and $c = 5.17 \text{ \AA}$, which is almost identical to the value of the lattice parameter in the standard hexagonal Ti_5Si_3 compound; that is, $a = 7.46 \text{ \AA}$ and $c = 5.15 \text{ \AA}$ [14]. This indicates that there is no compositional deviation even after the electrical discharge process. This result supports that physical breakdown of the oxide film of MAed powder occurs first in the initial stage of an electrical discharge.

To investigate the consolidation mechanism of nanostructured Ti_5Si_3 solid compact by electrical discharge, electrical discharging characteristics were considered in terms

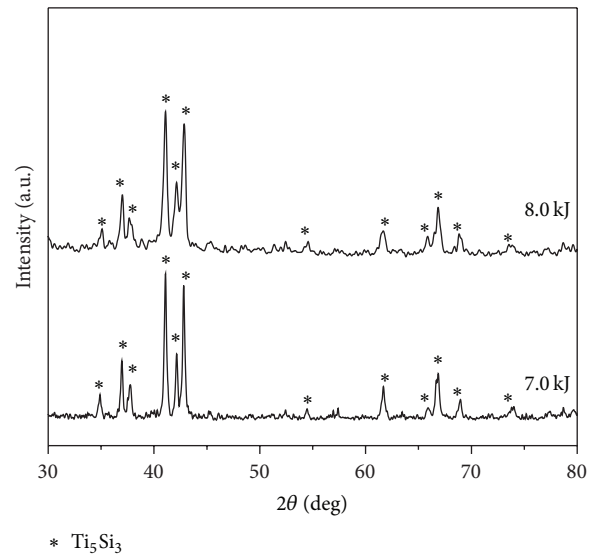


FIGURE 5: XRD patterns of the Ti_5Si_3 compacts obtained by electrical discharge consolidation of MAed Ti_5Si_3 powder using 7.0 and 8.0 kJ of input energy.

of input energy and capacitance under current experimental conditions. A typical discharge curve (Figure 7(a)) shows voltage and current in terms of discharge time. $450 \mu\text{F}$ of capacitance and 5.58 kV of input voltage were employed

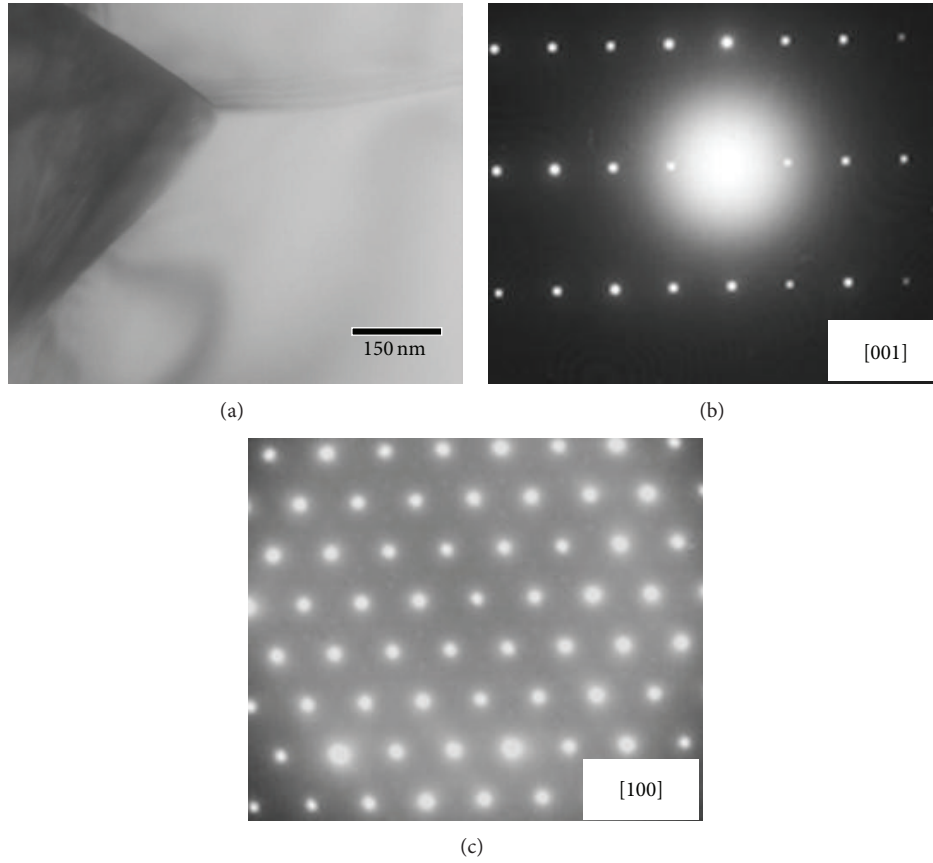


FIGURE 6: Typical TEM bright-field image (a) and selected area diffraction patterns ((b) and (c)) of the EDC Ti_5Si_3 compact at 7.0 kJ of input energy [13].

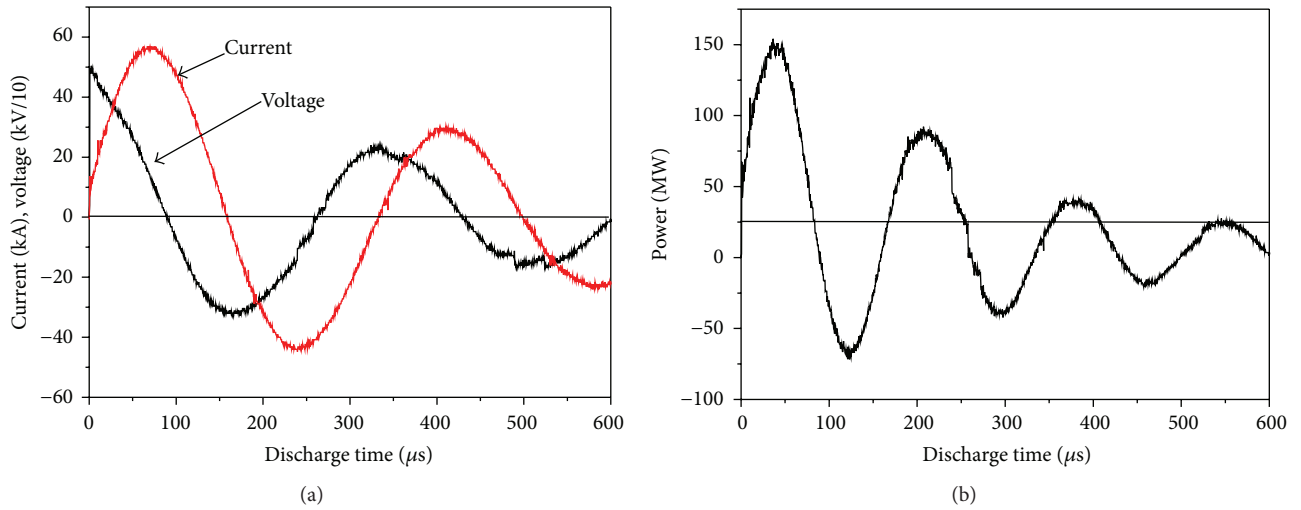


FIGURE 7: (a) Typical discharge curve measured current and voltage on oscilloscope and (b) typical power curve versus discharge time (discharge condition: 450 μF , 7.0 kJ).

TABLE 2: Peak voltage, peak current, discharge time, and heat generated (ΔH) during a discharge.

Capacitance (μF)	Input energy (kJ)	Peak voltage (kV)	Peak current (kA)	Discharge time (μF)	ΔH (J)
450	7.0	5.04	58.4	159	5880
450	8.0	5.36	60.8	159	6640

TABLE 3: Temperature rise (ΔT), current density (j), and pinch pressure (P) produced by an electrical discharge.

Input energy (kJ)	Temperature rise ($^{\circ}\text{C}$)	Current density (A/m^2)	Pinch pressure (MPa)
7.0	29,163	7.75×10^{11}	300
8.0	33,371	8.06×10^{11}	322

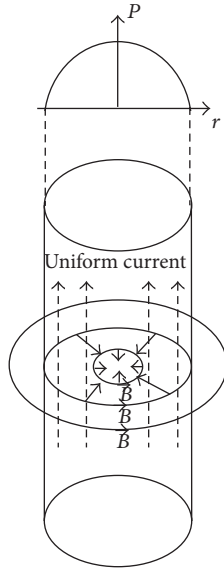


FIGURE 8: Linear pinch effect with a uniform current distribution.

to yield 7.0 kJ. The input energy (E) is predetermined by controlling input voltage (V) according to

$$E = \frac{CV^2}{2}, \tag{1}$$

where C is the capacitance of a capacitor. Figure 7(a) shows that the peak current was 58.4 kA and the peak voltage was 5.04 kV. From the results shown in Figure 7(a), the power (watt) curve is plotted in Figure 7(b) against the discharge time. The power was obtained from the following equation:

$$P \text{ (watt)} = \text{current (A)} \times \text{voltage (V)} = I^2 R \text{ (J/sec)}. \tag{2}$$

The discharge times for the duration of the first cycle at two different input energies are identical to be approximately 159 μsec . The amount of heat generated (ΔH) during a discharge can be obtained by using

$$\Delta H = \sum [i^2(t) R(t) \Delta t]. \tag{3}$$

Typical discharge characteristics under the current conditions are tabulated in Table 2 in terms of peak current, peak voltage, discharge time, and ΔH . It is known that ΔH increases with an increase in input energy at constant capacitance.

As a usual sintering process, the consolidation of metal powder requires a heat. To understand the effects of ΔH as one of discharge characteristics for the consolidation process,

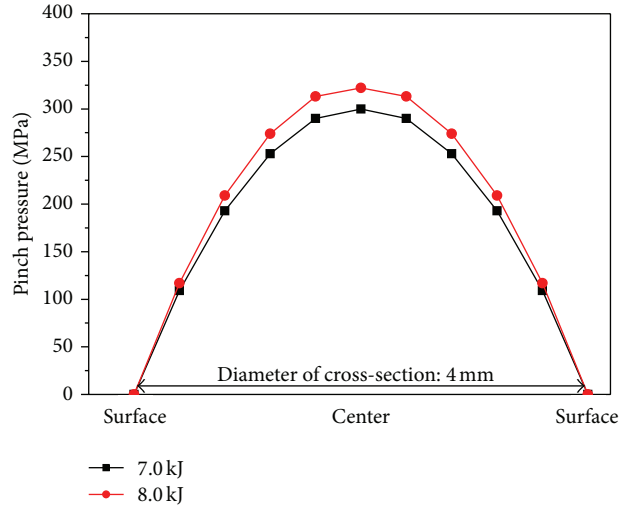


FIGURE 9: Distribution of pinch pressure generated on the cross-section of EDC Ti_5Si_3 compact.

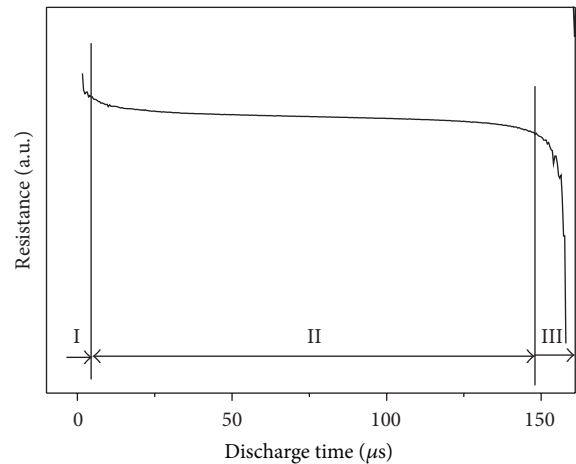


FIGURE 10: Resistance variation of MAed Ti_5Si_3 powder column calculated from the voltage and current recordings during an electrical discharge.

the temperature rise (ΔT), which is caused by an input energy, is now considered and estimated using

$$W = mCp\Delta T, \tag{4}$$

where m is the mass of the MAed Ti_5Si_3 powder and Cp is the specific heat of Ti_5Si_3 . The electrical input power (W) was calculated by integrating current and voltage as a function of discharge time. The resulting data for the heat generated by the electrical discharge process are listed in Table 3. It can be known that the electrical discharge produces the heat

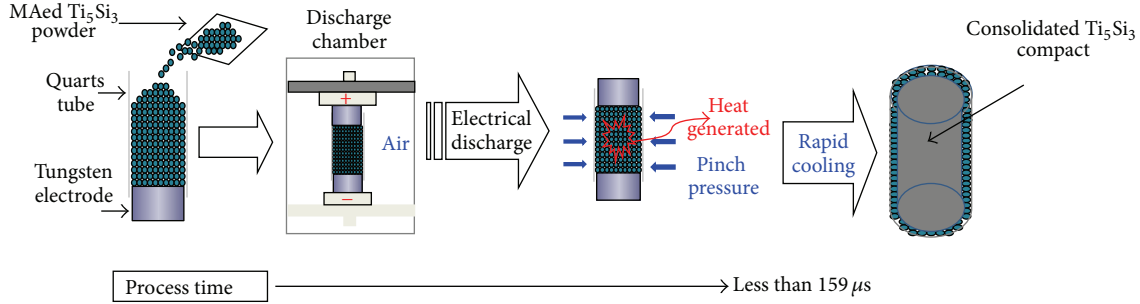


FIGURE 11: Schematic illustration for the formation of nanostructured Ti_5Si_3 compact by an electrical discharge of MAed Ti_5Si_3 powder.

significantly greater than the melting temperature of Ti_5Si_3 . Such a heat generated through the MAed Ti_5Si_3 powder is supposed to be high enough to vaporize the Ti_5Si_3 powder. However, the duration of the heat rise as $159 \mu\text{sec}$ could be too short for the complete vaporization process, resulting in the phase transformation into liquid. Moreover, it can be expected that the consolidated Ti_5Si_3 compact contains some pores since the electrical discharge process of Ti_5Si_3 powder was carried out without applying any pressure. Therefore, one possible force which can pressurize the liquidus powder can be considered as a function of input energy.

When a capacitor bank is discharged through a powder column, a long cylindrical metal powder column conducting an axial current, distributed axisymmetrically as shown in Figure 8, tends to contract radially inwards. At this moment the magnetic field generated by the current flow causes a diametric contraction, which is known as the pinch effect [20]. The magnitude of the magnetic field (B) can be obtained by using

$$B = \frac{1}{2} \mu r j, \quad (5)$$

where μ is the permeability, j is the current density, and r is the distance from the center of the powder column. The resulting pinch pressure (P) is the mechanical force acting on the powder column that will produce a solid core. The pinch pressure is given by

$$P = \frac{\mu j^2 (a^2 - r^2)}{4}, \quad (6)$$

where a is the radius of the cylindrical powder column. Allow the diameter ($2a$) of the contact region to be approximately one-tenth of the diameter of an average powder particle, as is often the case in solid mechanics [21]. MAed Ti_5Si_3 powder particles are considered to be stacked in such a linear manner that only one contact point is formed, resulting in the parallel straight current passage. The geometrical parameters needed for estimating the pinch pressure can be obtained and are tabulated in Table 4. Using these parameters, the maximum pinch pressure can be estimated in the center of the contact area (at $r = 0$). The resulting pinch pressures calculated under current experimental conditions are also listed in Table 3. It can be known that the pinch pressures between 300 and 322 MPa by the discharge were generated and could

TABLE 4: Geometric parameters in the pinch pressure calculation.

Number of particles on cross-section of powder column	614
Contact area of particle (m^2)	1.23×10^{-10}
Mean cross-sectional area of powder particle (m^2)	7.55×10^{-8}
Radius of the powder column (m)	1.2×10^{-4}

pressurize the liquidus powder particles, producing a bulk-typed Ti_5Si_3 compact without containing pores.

Since the pinch pressure is maximal at the center of Ti_5Si_3 powder column, its distribution across the cross-section of the compact should be different. The distribution of pinch pressures generated across the Ti_5Si_3 powder column with two different input energies is shown in Figure 9. The pinch pressure decreases down to 0 at the surface of the Ti_5Si_3 powder column. Since the pinch pressure is maximal at the center of the powder column, the solid core is formed easily, especially in the center of the Ti_5Si_3 compact. Therefore, it is very logical that the heat generated is the required parameter to melt the MAed Ti_5Si_3 powder particles and the pinch pressure can condense them without allowing a formation of pores across the compact.

Figure 10 shows the resistance change through the MAed Ti_5Si_3 powder column during an electrical discharge, which was determined from the recordings of voltage and current. It can be seen that there are three distinct regions: 0 to $6 \mu\text{sec}$ as stage 1, 7 to $146 \mu\text{sec}$ as stage 2, and 147 to $159 \mu\text{sec}$ as stage 3. In stage 1, electronic and physical breakdown of the oxide layer of MAed Ti_5Si_3 powder occurred, causing the rapid drop of resistance. In stage 2, the resistance decreased very slowly. The heat generated during a discharge would liquefy the MAed Ti_5Si_3 powder. Both condensation and densification of melted Ti_5Si_3 powder are promoted by the pinch force, especially in the center of the powder column. In stage 3, another rapid drop of resistance occurred. The rapid cooling occurs in this stage, resulting in the preservation of nanosized crystallite of Ti_5Si_3 compact.

Figure 11 shows the formation sequence of nanostructured Ti_5Si_3 compact by the electrical discharge of MAed Ti_5Si_3 powder, indicating that the heat generated, pinch pressure, and rapid cooling are required parameters for the consolidation process of nanostructured Ti_5Si_3 .

4. Conclusions

Electrical discharges of mechanical alloyed Ti-37.5 at.% Si powder mixture using a capacitance of 450 μF at input energies of 7.0 and 8.0 kJ were carried out without applying any external pressure. The MAed Ti_5Si_3 powder was successfully consolidated in times as short as 160 μsec into a solid bulk of Ti_5Si_3 compact with nanosized crystallites. It is proposed that, during an electrical discharge, physical breakdown of the oxide film of MAed Ti_5Si_3 powder occurs first. Both melting and condensing the Ti_5Si_3 powder are promoted by the heat and the pinch force especially in the center of the powder column, respectively. And then rapid cooling occurred, resulting in the formation of nanostructured Ti_5Si_3 compact.

Conflict of Interests

The authors declare that there is no conflict of interests regarding the publication of this paper.

Acknowledgment

This research was supported by the Basic Science Research Program through the National Research Foundation of Korea (NRF) funded by the Ministry of Education, Science and Technology (2013R1A1A2010207).

References

- [1] K. Kasraee, A. Tayebifard, and E. Salahi, "Investigation of pre-milling effect on synthesis of Ti_5Si_3 prepared by MASHS, SHS, MA," *Journal of Materials Engineering and Performance*, vol. 22, no. 12, pp. 3742–3748, 2013.
- [2] S. Sabooni, F. Karimzadeh, and M. H. Abbasi, "Thermodynamic aspects of nanostructured Ti_5Si_3 formation during mechanical alloying and its characterization," *Bulletin of Materials Science*, vol. 35, no. 3, pp. 439–447, 2012.
- [3] I.-J. Shon, "Synthesis of $\text{Ti}_5\text{Si}_{3-x}\text{Nb}$ composites by the field-activated combustion method," *Metals and Materials International*, vol. 3, no. 3, pp. 199–202, 1997.
- [4] A. K. Vasudevan and J. J. Petrovic, "A comparative overview of molybdenum silicide composites," *Materials Science and Engineering: A*, vol. 155, pp. 1–17, 1992.
- [5] R. Rosenkranz, G. Frommeyer, and W. Smarsly, "Microstructures and properties of high melting point intermetallic Ti_5Si_3 and TiSi_2 compounds," *Materials Science and Engineering A*, vol. 152, no. 1-2, pp. 288–294, 1992.
- [6] M. Naka, T. Matsui, M. Maeda, and H. Mori, "Formation and thermal stability of amorphous Ti-Si alloys," *Materials Transactions*, vol. 36, no. 7, pp. 797–801, 1995.
- [7] H.-Y. Wang, M. Zha, S.-J. Lü, C. Wang, and Q.-C. Jiang, "Reaction pathway and phase transitions in Al-Ti-Si system during differential thermal analysis," *Solid State Sciences*, vol. 12, no. 8, pp. 1347–1351, 2010.
- [8] R. Mitra, "Microstructure and mechanical behavior of reaction hot-pressed titanium silicide and titanium silicide-based alloys and composites," *Metallurgical and Materials Transactions A: Physical Metallurgy and Materials Science*, vol. 29, no. 6, pp. 1629–1641, 1998.
- [9] M. Zha, H. Y. Wang, S. T. Li, S. L. Li, Q. L. Guan, and Q. C. Jiang, "Influence of Al addition on the products of self-propagating high-temperature synthesis of Al-Ti-Si system," *Materials Chemistry and Physics*, vol. 114, no. 2-3, pp. 709–715, 2009.
- [10] B. R. Krueger, A. H. Mutz, and T. Vreeland, "Shock-induced and self-propagating high-temperature synthesis reactions in two powder mixtures: 5:3 Atomic ratio Ti/Si and 1:1 Atomic ratio Ni/Si," *Metallurgical Transactions A*, vol. 23, no. 1, pp. 55–58, 1992.
- [11] S. C. Deevi and N. N. Thadhani, "Reaction synthesis of high-temperature silicides," *Materials Science and Engineering A*, vol. 192-193, no. 2, pp. 604–611, 1995.
- [12] W. H. Lee and C. Y. Hyun, "Fabrication of fully porous and porous-surfaced Ti-6Al-4V implants by electro-discharge-sintering of spherical Ti-6Al-4V powders in an one-step process," *Journal of Materials Processing Technology*, vol. 189, no. 1–3, pp. 219–223, 2007.
- [13] Y. W. Cheon, Y. J. Jo, C. M. Lee, H. S. Jang, K. B. Kim, and W. H. Lee, "Consolidation of mechanical alloyed Ti-37.5 at.% Si powder mixture using an electro-discharge technique," *Materials Science and Engineering A*, vol. 467, no. 1-2, pp. 89–92, 2007.
- [14] H. S. Jang, Y. J. Cho, T. J. Kang, K. B. Kim, and W. H. Lee, "A study on the synthesis and consolidation of Ti_3Al by electro-discharge," *Journal of Korean Institute of Metals and Materials*, vol. 47, no. 8, pp. 488–493, 2009.
- [15] Y.-W. Cheon, Y.-J. Cho, T.-J. Kang et al., "Characteristic studies on electro-discharge-sintering of Ti_5Si_3 powder synthesized by mechanical alloying," *Journal of Korean Institute of Metals and Materials*, vol. 47, no. 10, pp. 660–666, 2009.
- [16] C. Xu and W.-F. Zhu, "Transformation mechanism and mechanical properties of commercially pure titanium," *Transactions of Nonferrous Metals Society of China*, vol. 20, no. 11, pp. 2162–2167, 2010.
- [17] M. Rahman, I. Reid, P. Duggan, D. P. Dowling, G. Hughes, and M. S. J. Hashmi, "Structural and tribological properties of the plasma nitrided Ti-alloy biomaterials: influence of the treatment temperature," *Surface and Coatings Technology*, vol. 201, no. 9–11, pp. 4865–4872, 2007.
- [18] O. Park, J.-I. Lee, M.-J. Chun et al., "High-performance Si anodes with a highly conductive and thermally stable titanium silicide coating layer," *RSC Advances*, vol. 3, no. 8, pp. 2538–2542, 2013.
- [19] W. Kim, S.-H. Kwak, C.-Y. Suh, J.-W. Lim, S.-W. Cho, and I.-J. Shon, "Mechanochemical synthesis and high-frequency induction heated consolidation of nanostructured Ti_5Si_3 and its mechanical properties," *Research on Chemical Intermediates*, vol. 39, no. 6, pp. 2339–2349, 2013.
- [20] S. Clyens, S. T. S. Al-Hassani, and W. Johnson, "The compaction of powder metallurgy bars using high voltage electrical discharges," *International Journal of Mechanical Sciences*, vol. 18, no. 1, pp. 37–40, 1976.
- [21] T. H. Wu, *Solid Mechanics*, Allyn and Bacon, Boston, Mass, USA, 1976.

Research Article

Vacuum Ultraviolet Field Emission Lamp Consisting of Neodymium Ion Doped Lutetium Fluoride Thin Film as Phosphor

Masahiro Yanagihara,¹ Takayuki Tsuji,¹ Mohd Zamri Yusop,^{1,2} Masaki Tanemura,¹ Shingo Ono,¹ Tomohito Nagami,³ Kentaro Fukuda,³ Toshihisa Suyama,³ Yuui Yokota,⁴ Takayuki Yanagida,⁵ and Akira Yoshikawa⁴

¹ Nagoya Institute of Technology, Gokiso-cho, Showa-ku, Nagoya, Aichi 466-8555, Japan

² Department of Materials, Manufacturing & Industrial, Faculty of Mechanical Engineering, Universiti Teknologi Malaysia (UTM), 81310 Skudai, Johor, Malaysia

³ Tokuyama Corporation, Kasumigaseki Common Gate West Tower 2-1, Kasumigaseki 3-chome, Chiyoda-ku, Tokyo 100-8983, Japan

⁴ Institute for Materials Research, Tohoku University, 2-1-1 Katahira, Aoba-ku, Sendai 980-8577, Japan

⁵ Kyushu Institute of Technology, 2-4 Hibikino, Wakamatsu-ku, Kitakyushu 808-0196, Japan

Correspondence should be addressed to Shingo Ono; ono.shingo@nitech.ac.jp

Received 16 July 2014; Accepted 24 August 2014; Published 11 September 2014

Academic Editor: Xiao-Feng Zhao

Copyright © 2014 Masahiro Yanagihara et al. This is an open access article distributed under the Creative Commons Attribution License, which permits unrestricted use, distribution, and reproduction in any medium, provided the original work is properly cited.

A vacuum ultraviolet (VUV) field emission lamp was developed by using a neodymium ion doped lutetium fluoride ($\text{Nd}^{3+} : \text{LuF}_3$) thin film as solid-state phosphor and carbon nanofiber field electron emitters. The thin film was synthesized by pulsed laser deposition and incorporated into the lamp. The cathodoluminescence spectra of the lamp showed multiple emission peaks at 180, 225, and 255 nm. These emission spectra were in good agreement with the spectra reported for the $\text{Nd}^{3+} : \text{LuF}_3$ crystal. Moreover, application of an acceleration voltage effectively increased the emission intensity. These results contribute to the performance enhancement of the lamp operating in the VUV region.

1. Introduction

Vacuum ultraviolet (VUV) light has been used in numerous fields, such as cleaning, surface modification, and sterilization, because short wavelength light with high photon energy is capable of breaking strong chemical bonds [1–3]. Therefore, performance improvements of VUV lamps contribute to the progress of these applications. The VUV gas lamp has widely been used [4–6] but presents limited stability, lifetime, and size. VUV lamps using a solid-state phosphor have attracted considerable attention as alternate light sources because they exhibit less deterioration, less fluctuation, and higher density than gas lamps [7, 8]. These lamps require wide band gap materials but few solid-state phosphors have substantial band gaps. Group III nitrides are suitable because they present a direct transition type band structure with a wide band gap

[9, 10]. However, even when using AlN, which emits light at a relatively short wavelength, the operating wavelength was limited to deep UV region [9, 11–13]. The wide band gap of diamond can be applied to UV but not to VUV lamps [14]. On the other hand, some fluorides have band gaps that are sufficiently wide to enable light emission in the VUV region [15, 16]. Fluoride composite materials have been widely studied as laser materials, scintillation materials, and optical materials because of their extremely wide band gap [17–24]. Specifically, a KMgF_3 thin film acting as a solid-state phosphor and carbon nanofiber (CNF) field electron emitter has previously been incorporated into a VUV lamp [25]. The emission spectra from the lamp showed two emission peaks at 155 and 180 nm in the 140–200 nm wavelength range, showing that solid-state phosphors can be exploited in VUV lamps.

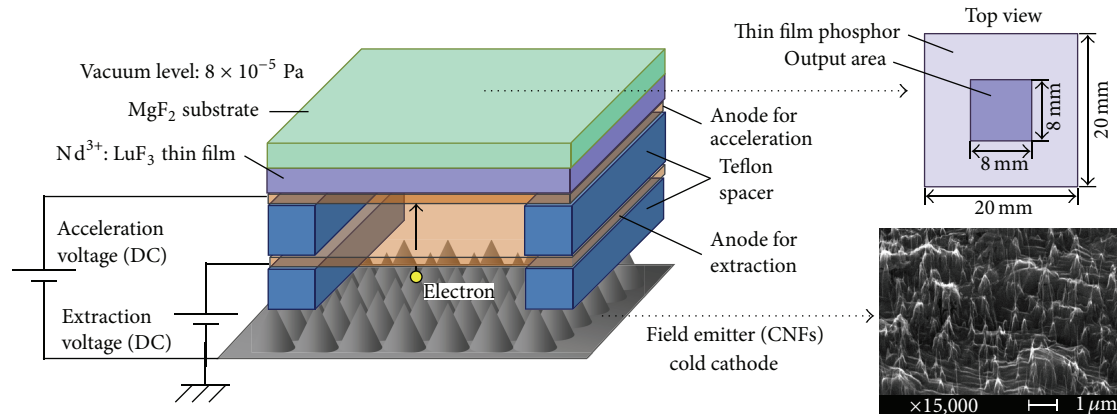


FIGURE 1: Schematic diagram of VUV field emission lamp. SEM image of CNFs is shown in the insert.

Neodymium ion doped lutetium fluoride ($\text{Nd}^{3+}:\text{LuF}_3$), whose cathodoluminescence (CL) efficiency is almost equivalent to KMgF_3 , was selected as a phosphor to develop a new VUV lamp. This lamp also consisted of CNFs field electron emitters. Among Nd^{3+} ion doped fluoride materials that emit VUV light, such as $\text{Nd}^{3+}:\text{LuF}_3$, $\text{Nd}^{3+}:\text{LaF}_3$, and $\text{Nd}^{3+}:\text{LuLiF}_4$ [26–28], $\text{Nd}^{3+}:\text{LuF}_3$ single crystals have reported the highest X-ray excited luminescence conversion efficiency [26]. However, large $\text{Nd}^{3+}:\text{LuF}_3$ single crystals have proven difficult to grow because of the occurrence of a hexagonal to orthorhombic phase transition (ca. 950°C) during the crystal growth process [26]. The stress caused by this structural reconfiguration results in crack formation in $\text{Nd}^{3+}:\text{LuF}_3$ single crystals. In contrast, growth of thin film suppresses these cracks owing to reducing stress by depositing small particles. For this reason, we fabricated $\text{Nd}^{3+}:\text{LuF}_3$ thin film by pulsed laser deposition (PLD) to deposit small particles. In addition, PLD has produced fewer chemical composition discrepancies between source targets and deposited thin films. Consequently, the fabrication of fluoride thin films by PLD does not require the utilization of the toxic fluorine gas [29].

2. Experimental Methods

2.1. Thin Film Fabrication. The target was prepared by pressing a 1:9 NdF_3 - LuF_3 powder mixture. A (001)-oriented MgF_2 crystal ($20\text{ mm} \times 20\text{ mm} \times 0.5\text{ mm}$) mounted on a rotating holder was used as a substrate and was maintained at 400°C during PLD. This substrate temperature was chosen because previous experiments on the growth of $\text{Nd}^{3+}:\text{LaF}_3$ thin films showed that substrate heating improved crystalline quality and VUV luminescence quantum efficiency and resulted in optimal performance at 400°C [27]. The thin film was deposited by irradiating the $\text{Nd}^{3+}:\text{LuF}_3$ target with the third harmonics of a Nd:YAG laser (355 nm in wavelength). The 2 mm diameter laser spot was focused on the target at a fluence of $2.5\text{ J}/\text{cm}^2$ and a repetition rate of 10 Hz. The deposition was carried out for 8 h at an average pressure of $3 \times 10^{-4}\text{ Pa}$ without atmosphere control.

2.2. Field Emission Lamp Construction. CNFs were grown by bombarding a grassy carbon substrate with Ar^+ at room temperature [30–32]. The ion beam, which had a diameter of 6 cm, was set at an incident angle of 45° and energy of 1 keV, respectively. The length and diameter of CNFs were 0.3–2 and 20 mm, respectively, with an approximate density of $5 \times 10^8\text{ cm}^{-2}$. Figure 1 shows the schematic of the lamp. In addition to the CNFs and the thin film, the lamp contained two copper mesh electrodes with a mesh width of 0.1 mm. Two teflon spacer plates were used to prevent short circuits and provide space for electron acceleration. A $200\text{ }\mu\text{m}$ thick spacer was placed between CNFs and a copper electrode and a 5 mm thick spacer was placed between the two copper electrodes. In this lamp, electrons were emitted from CNFs using the extraction voltage and accelerated toward the thin film using the acceleration voltage. VUV CL from the $\text{Nd}^{3+}:\text{LuF}_3$ thin film was emitted through the substrate. A substrate with high transmittance in the VUV region was needed to output light efficiently and MgF_2 , which exhibited 94% transmittance at 180 nm, satisfied this condition. The lamp benefited from a low power consumption and reduced thermal effects when the field electron emitters were used as cold cathodes [33, 34]. The lamp was operated in the vacuum chamber at an average pressure of $8 \times 10^{-5}\text{ Pa}$.

3. Results and Discussion

The thickness and surface morphology of the $\text{Nd}^{3+}:\text{LuF}_3$ thin film was investigated by using scanning electron microscopy (SEM). The thin film contained some droplets with cracks that originate from structural phase transitions. In contrast, the uniform layer was about 15 nm thick without any cracks. The crystallographic properties were also evaluated by using X-ray diffraction. The high and sharp diffraction patterns indicated the well crystallization of the thin film. The detailed data of these evaluations are described in [29].

Figure 2 shows the CL spectra of the $\text{Nd}^{3+}:\text{LuF}_3$ thin film at different acceleration voltages ranging from 1 to 20 kV. The electron beam current was kept at 600 pA during the CL measurements. The spectra showed a dominant peak in the VUV region at 179 nm and two additional emission peaks at

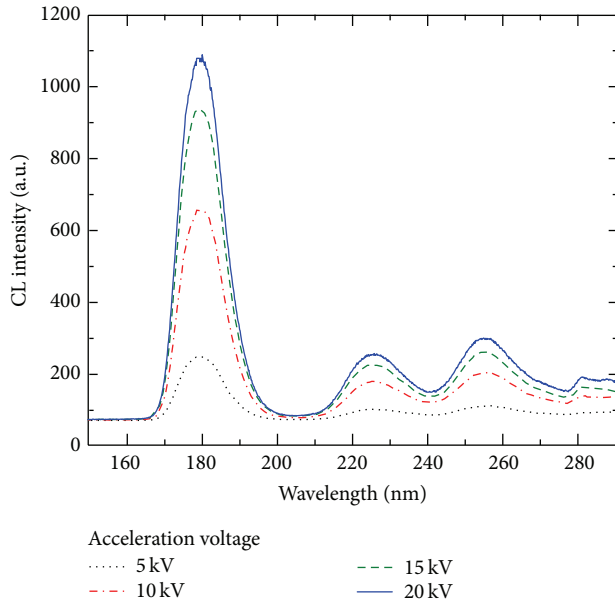


FIGURE 2: CL spectra of the $\text{Nd}^{3+}:\text{LuF}_3$ thin film at acceleration voltages ranging from 1 to 20 kV.

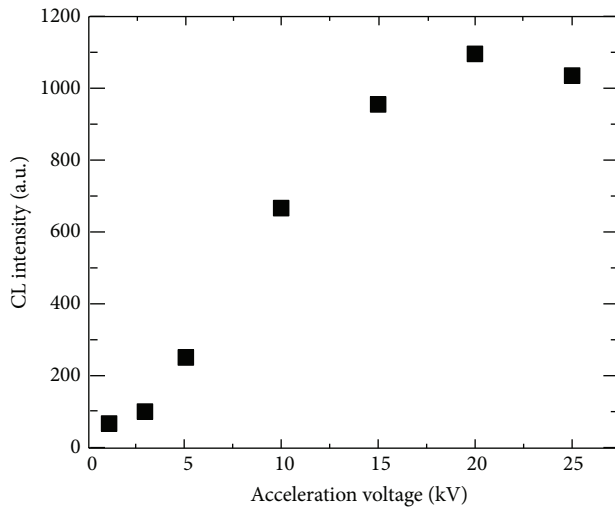


FIGURE 3: Output CL intensity of the $\text{Nd}^{3+}:\text{LuF}_3$ thin film at 179 nm for acceleration voltages ranging from 1 to 25 kV.

223 and 255 nm, which are consistent with the emission peaks observed for $\text{Nd}^{3+}:\text{LuF}_3$ single crystals [17]. These results show that although the PLD target was obtained by pressing NdF_3 and LuF_3 powders together (undoped material), Nd^{3+} acted as a dopant for LuF_3 and a luminescent center in the thin film.

The influence of the acceleration voltage on the CL intensity of the $\text{Nd}^{3+}:\text{LuF}_3$ thin film at 180 nm was also investigated as shown in Figure 3. The CL intensity increased with increasing acceleration voltage before saturation at 25 kV. This result suggests that incident electrons passed through the thin film before giving all their energy to the thin film at 25 kV.

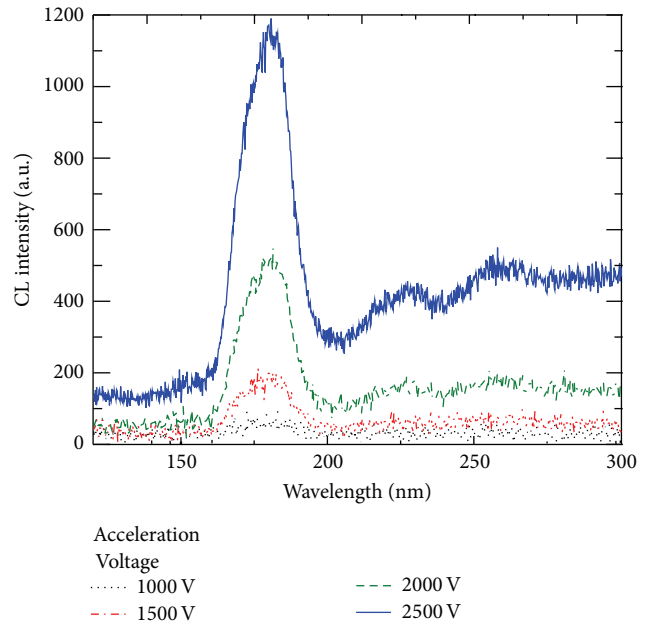


FIGURE 4: Emission spectra of the lamp at acceleration voltages ranging from 1 to 2.5 kV.

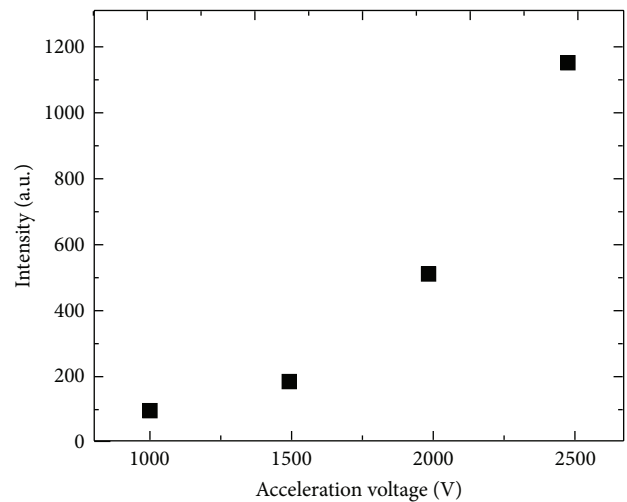


FIGURE 5: Output CL intensity of the lamp at 180 nm for acceleration voltages ranging from 1 to 2.5 kV.

The emission spectra of the lamp were measured at different acceleration voltages ranging from 1 to 2.5 kV. The extraction voltage was kept at 600 V during the measurements. The emission spectra (Figure 4) presented a dominant peak in the VUV region at 180 nm and two additional peaks at 225 and 255 nm. These spectra closely matched the emission spectra obtained for the $\text{Nd}^{3+}:\text{LuF}_3$ thin film.

The influence of the acceleration voltage on the CL intensity of the lamp at 180 nm was evaluated. The CL intensity (Figure 5) showed a nonlinear dependence on the acceleration voltage, which was attributed to an increase of the electron diffusion region in the thin film. The output

power of this lamp may amount to several microwatts because $\text{Nd}^{3+}:\text{LuF}_3$ and KMgF_3 show quasiequivalent conversion efficiencies [16]. An increase in acceleration voltage may therefore efficiently enhance the output power of this lamp.

The luminescence area of this VUV lamp can easily generate a large area with little thermal effect and low power consumption by employing a CNF field electron emitter. In addition a solid-state phosphor brings many benefits in the VUV lamp such as safety, longevity, stability, and downsizing.

4. Conclusions

In summary, a VUV field emission lamp consisting of a $\text{Nd}^{3+}:\text{LuF}_3$ thin film as a solid-state phosphor and CNF field electron emitter was fabricated. The CL spectra of the lamp showed multiple emission peaks at 180, 225, and 255 nm, which were in good agreement with emission spectra previously reported for the $\text{Nd}^{3+}:\text{LuF}_3$ crystal. This result suggested that Nd^{3+} ion acted as a luminescent center and doped LuF_3 in the synthesized thin film although the target used during PLD was obtained by pressing NdF_3 and LuF_3 powders into a pellet. Furthermore, the output emission intensity showed a nonlinear response to the acceleration voltage, indicating that an increase in acceleration voltage may significantly enhance this output emission intensity. Although recent gas lamps are improving their performances, this lamp may soon become one of the candidates of VUV light sources. These techniques are essential to numerous applications, such as sterilization, surface cleaning, and synthesis and degradation of chemical material.

Conflict of Interests

The authors declare that there is no conflict of interests regarding the publication of this paper.

Acknowledgments

This research was partially supported by a Grant-in-Aid for Scientific Research C (40370126), from the Japan Society for the Promotion of Science (JSPS), Nippon Sheet Glass Foundation, and Nanotechnology Platform Program (Molecule and Material Synthesis) of the Ministry of Education, Culture, Sports, Science and Technology (MEXT), Japan. The authors would like to thank Professor Y. Ichikawa of the Nagoya Institute of Technology (NIT) for invaluable discussions. The authors are grateful to Dr. S. Nakao of the Institute for Molecular Science (IMS) for important technical support in this research. The authors would like to thank Enago (<http://www.enago.jp/>) for the English Language review.

References

- [1] J. R. Vig, "UV/ozone cleaning of surfaces," *Journal of Vacuum Science & Technology A*, vol. 3, p. 1027, 1985.
- [2] L. J. Matienzo, J. A. Zimmerman, and F. D. Egitto, "Surface modification of fluoropolymers with vacuum ultraviolet irradiation," *Journal of Vacuum Science & Technology A*, vol. 12, p. 2662, 1994.
- [3] S. Lerouge, A. C. Fozza, M. R. Wertheimer, R. Marchand, and L. Yahia, "Sterilization by low-pressure plasma: the role of vacuum-ultraviolet radiation," *Plasmas and Polymers*, vol. 5, no. 1, pp. 31–46, 2000.
- [4] J. Wieser, D. E. Murnick, A. Ulrich, H. A. Huggins, A. Liddle, and W. L. Brown, "Vacuum ultraviolet rare gas excimer light source," *Review of Scientific Instruments*, vol. 68, no. 3, pp. 1360–1364, 1997.
- [5] J. Y. Zhang and I. W. Boyd, "Efficient excimer ultraviolet sources from a dielectric barrier discharge in rare-gas/halogen mixtures," *Journal of Applied Physics*, vol. 80, p. 633, 1996.
- [6] A. C. Fozza, A. Kruse, A. Holländer, A. Ricard, and M. R. Wertheimer, "Vacuum ultraviolet to visible emission of some pure gases and their mixtures used for plasma processing," *Journal of Vacuum Science and Technology A: Vacuum, Surfaces and Films*, vol. 16, no. 1, pp. 72–77, 1998.
- [7] K. Watanabe, T. Taniguchi, T. Niiyama, K. Miya, and M. Taniguchi, "Far-ultraviolet plane-emission handheld device based on hexagonal boron nitride," *Nature Photonics*, vol. 3, no. 10, pp. 591–594, 2009.
- [8] A. Bergh, G. Craford, A. Duggal, and R. Haitz, "The promise and challenge of solid-state lighting," *Physics Today*, vol. 54, no. 12, pp. 42–47, 2001.
- [9] I. Akasaki, H. Amano, H. Murakami, M. Sassa, H. Kato, and K. Manabe, "Growth of GaN and AlGaN for UV/blue p-n junction diodes," *Journal of Crystal Growth*, vol. 128, no. 1-4, pp. 379–383, 1993.
- [10] I. Akasaki and H. Amano, "Crystal growth and conductivity control of group III nitride semiconductors and their application to short wavelength light emitters," *Japanese Journal of Applied Physics*, vol. 36, no. 9A, p. 5393, 1997.
- [11] W. M. Yim, E. J. Stofko, P. J. Zanzucchi, J. I. Pankove, M. Ettenberg, and S. L. Gilbert, "Epitaxially grown AlN and its optical band gap," *Journal of Applied Physics*, vol. 44, no. 1, pp. 292–296, 1973.
- [12] E. Silveira, J. A. Freitas, S. B. Schujman, and L. J. Schowalter, "AlN bandgap temperature dependence from its optical properties," *Journal of Crystal Growth*, vol. 310, no. 17, pp. 4007–4010, 2008.
- [13] T. Oto, R. G. Banal, K. Kataoka, M. Funato, and Y. Kawakami, "100 mW deep-ultraviolet emission from aluminium-nitride-based quantum wells pumped by an electron beam," *Nature Photonics*, vol. 4, no. 11, pp. 767–771, 2010.
- [14] S. Koizumi, K. Watanabe, M. Hasegawa, and H. Kanda, "Ultraviolet emission from a diamond pn junction," *Science*, vol. 292, no. 5523, pp. 1899–1901, 2001.
- [15] T. Nishimatsu, N. Terakubo, H. Mizuseki et al., "Band structures of perovskite-like fluorides for vacuum-ultraviolet-transparent lens materials," *Japanese Journal of Applied Physics 2: Letters*, vol. 41, no. 4, pp. L365–L367, 2002.
- [16] S. Ono, R. El Ouenzerfi, A. Quema et al., "Band-structure design of fluoride complex materials for deep-ultraviolet light-emitting diodes," *Japanese Journal of Applied Physics*, vol. 44, no. 10, pp. 7285–7290, 2005.
- [17] P. J. Key and R. C. Preston, "Magnesium fluoride windowed deuterium lamps as radiance transfer standards between 115 and 370 nm," *Journal of Physics E: Scientific Instruments*, vol. 13, no. 8, p. 866, 1980.
- [18] Y. Hatanaka, H. Yanagi, T. Nawata et al., "Properties of ultra-large CaF_2 crystals for the high NA optics," in *Optical Microlithography XVIII*, vol. 5754 of *Proceedings of SPIE*, 2005.

- [19] T. Kozeki, Y. Suzuki, M. Sakai et al., "Observation of new excitation channel of cerium ion through highly vacuum ultraviolet transparent LiCAF host crystal," *Journal of Crystal Growth*, vol. 229, no. 1, pp. 501–504, 2001.
- [20] A. Yoshikawa, T. Yanagida, Y. Yokota et al., "Single crystal growth, optical properties and neutron response of Ce³⁺ doped LiCaAlF₆," *IEEE Transactions on Nuclear Science*, vol. 56, no. 6, pp. 3796–3799, 2009.
- [21] N. Kawaguchi, T. Yanagida, A. Novoselov et al., "Neutron responses of Eu²⁺ activated LiCaAlF₆ scintillator," in *Proceedings of the IEEE Nuclear Science Symposium Conference Record (NSS/MIC '08)*, pp. 1174–1176, Dresden, Germany, October 2008.
- [22] R. Visser, P. Dorenbos, C. W. E. van Eijk, A. Meijerink, and H. W. den Hartog, "The scintillation intensity and decay from Nd³⁺ 4f²5d and 4f³ excited states in several fluoride crystals," *Journal of Physics: Condensed Matter*, vol. 5, article 8437, 1993.
- [23] S. Ono, Y. Suzuki, T. Kozeki et al., "High-energy, all-solid-state, ultraviolet laser power-amplifier module design and its output-energy scaling principle," *Applied Optics*, vol. 41, no. 36, pp. 7556–7560, 2002.
- [24] R. W. Waynant and P. H. Klein, "Vacuum ultraviolet laser emission from Nd³⁺:LaF₃," *Applied Physics Letters*, vol. 46, p. 14, 1985.
- [25] M. Yanagihara, M. Z. Yusop, M. Tanemura et al., "Vacuum ultraviolet field emission lamp utilizing KMgF₃ thin film phosphor," *APL Materials*, vol. 2, no. 4, Article ID 046110, 2014.
- [26] K. Fukuda, S. Ishizu, N. Kawaguchi et al., "Crystal growth and optical properties of the Nd³⁺ doped LuF₃ single crystals," *Optical Materials*, vol. 33, no. 8, pp. 1143–1146, 2011.
- [27] M. Ieda, T. Ishimaru, S. Ono et al., "Optical characteristic improvement of neodymium-doped lanthanum fluoride thin films grown by pulsed laser deposition for vacuum ultraviolet application," *Japanese Journal of Applied Physics*, vol. 51, no. 2, Article ID 022603, 2012.
- [28] A. F. H. Librantz, L. Gomes, S. L. Baldochi, I. M. Ranieri, and G. E. Brito, "Luminescence study of the 4f²5d configuration of Nd³⁺ in LiYF₄, LiLuF₄ and BaY₂F₈ crystals," *Journal of Luminescence*, vol. 121, no. 1, pp. 137–148, 2006.
- [29] M. Ieda, T. Ishimaru, S. Ono et al., "Structural and optical properties of neodymium-doped lutetium fluoride thin films grown by pulsed laser deposition," *Optical Materials*, vol. 35, no. 12, pp. 2329–2331, 2013.
- [30] M. Tanemura, T. Okita, H. Yamauchi, S. Tanemura, and R. Morishima, "Room-temperature growth of a carbon nanofiber on the tip of conical carbon protrusions," *Applied Physics Letters*, vol. 84, no. 19, pp. 3831–3833, 2004.
- [31] M. Tanemura, J. Tanaka, K. Itoh et al., "Field electron emission from sputter-induced carbon nanofibers grown at room temperature," *Applied Physics Letters*, vol. 86, no. 11, Article ID 113107, pp. 1–3, 2005.
- [32] M. Tanemura, T. Okita, J. Tanaka et al., "Room-temperature growth and applications of carbon nanofibers: A review," *IEEE Transactions on Nanotechnology*, vol. 5, no. 5, pp. 587–593, 2006.
- [33] R. C. Che, L.-M. Peng, and M. S. Wang, "Electron side-emission from corrugated nanotubes," *Applied Physics Letters*, vol. 85, no. 20, pp. 4753–4755, 2004.
- [34] Y. Saito, S. Uemura, and K. Hamaguchi, "Cathode ray tube lighting elements with carbon nanotube field emitters," *Japanese Journal of Applied Physics*, vol. 37, no. 3, pp. L346–L348, 1998.

Research Article

Synthesis of Silver Nanoparticles Dispersed in Various Aqueous Media Using Laser Ablation

**M. Tajdidzadeh,¹ B. Z. Azmi,^{1,2} W. Mahmood M. Yunus,¹ Z. Abidin Talib,¹
A. R. Sadrolhosseini,³ K. Karimzadeh,⁴ S. A. Gene,¹ and M. Dorraj²**

¹ Department of Physics, Faculty of Science, Universiti Putra Malaysia (UPM), 43400 Serdang, Malaysia

² Materials Synthesis and Characterization Laboratory, Advanced Institute of Technology, Universiti Putra Malaysia (UPM), 43400 Serdang, Malaysia

³ Wireless and Photonics Network Research (WIPNET), Faculty of Engineering, Universiti Putra Malaysia (UPM), 43400 Serdang, Malaysia

⁴ Department of Civil Engineering, Universiti Putra Malaysia (UPM), Malaysia, 43400 Serdang, Malaysia

Correspondence should be addressed to B. Z. Azmi; azmizak@gmail.com

Received 17 June 2014; Revised 2 August 2014; Accepted 10 August 2014; Published 8 September 2014

Academic Editor: Xiao-Feng Zhao

Copyright © 2014 M. Tajdidzadeh et al. This is an open access article distributed under the Creative Commons Attribution License, which permits unrestricted use, distribution, and reproduction in any medium, provided the original work is properly cited.

The particle size, morphology, and stability of Ag-NPs were investigated in the present study. A Q-Switched Nd:YAG pulsed laser ($\lambda = 532$ nm, 360 mJ/pulse) was used for ablation of a pure Ag plate for 30 min to prepare Ag-NPs in the organic compound such as ethylene glycol (EG) and biopolymer such as chitosan. The media (EG, chitosan) permitted the making of NPs with well dispersed and average size of Ag-NPs in EG is about 22 nm and in chitosan is about 10 nm in spherical form. Particle size, morphology, and stability of NPs were compared with distilled water as a reference. The stability of the samples was studied by measuring UV-visible absorption spectra of samples after one month. The result indicated that the formation efficiency of NPs in chitosan was higher than other media and NPs in chitosan solution were more stable than other media during one month storage. This method for synthesis of silver NPs could be as a green method due to its environmentally friendly nature.

1. Introduction

Recently, a lot of researches interested in metallic nanostructure materials have come up due to their unusual properties which are different from their bulk materials such as their electronic, optical, magnetic, and chemical properties [1]. Due to these properties the main attraction for scientists is applications of these nanoparticles (NPs) in technology. For instance antibacterial and nano-composite are numbers of the most crucial applications of silver nano particles (Ag-NPs) [2–4]. Hence, various NPs or nanocomposite materials have been investigated for their antimicrobial activity as growth inhibitors [5]. A lot of methods such as chemical methods, sol gel, sonochemical method, and laser ablation (LA) were used to prepare the Ag-NPs [6–9].

Nevertheless, such chemical reduction method is not recommended since the chemicals are highly reactive and

known to pose a potential environmental hazard and biological risks. Instead, a variety of green technologies for the preparation of Ag-NPs have been developed [10]. Newly, plasma assisted methods based in LA. The advantage of LA compared to chemical synthesis is the simplicity of the procedure and also absence of chemical reagents in solution. Furthermore, the laser pulse has appeared to be more flexible and promising technique for the reason that it is proficient to ablate different type of materials such as metals, ceramic and polymer considers the ultra-high energy density. In LA, the control over the growth process was provided by manipulating the process parameters like irradiation time, duration, energy density, wavelength, and so forth [11]. LA technique is based on ablating a solid target in a gas or a liquid environment. The more effective collection of synthesized NPs can be achieved by LA in a liquid phase. The most important features of the LA technique have been studied by

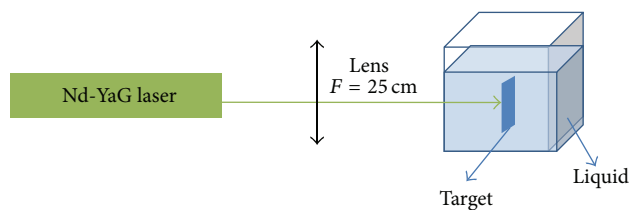


FIGURE 1: The LA setup for the colloidal NPs production.

many researchers [12, 13], due to the aqueous media which is highly effective on the particle size and stability. Recently, using an organic solvent as a stabilizer for synthesis of NPs has been investigated [14, 15]. Among all organic solvents, ethylene glycol (EG) ($\text{HOCH}_2\text{CH}_2\text{OH}$) got more attraction due to widespread chemical and physical properties and applications. EG is a colorless, practically odorless, with relatively low-volatility, and is hygroscopic liquid with low viscosity. Indeed, it is completely miscible with water, many organic liquids, and many polar solvents (e.g., alcohols, glycol, ethers, and acetone) and vaguely soluble in nonpolar solvent such as toluene, benzene, and chloroform [16–19].

On the other hand, among the natural polymers, chitosan is the second most naturally abundant polysaccharide that can be easily isolated from crustacean shell. Since chitosan is nontoxic and has been approved by Food and Drug Administration [20], in this case, the dispersed Ag-NPs in chitosan solution does not necessarily need to be separated and purified [21].

In this work, we performed LA silver plate in EG and chitosan to prepare Ag-NPs. In the LA process, we hypothesized that the Ag-NPs size decreases. Conversely, the stability of NPs increases in these media to compare with in distilled water (DW).

2. Experiment

The schematic diagram of the LA experimental setup is indicated in Figure 1. A pulsed Q-Switched Nd: YAG laser (SL400/SL800 system) with pulse duration of 10 ns and 30 Hz repetition rate at a second harmonic wavelength (532 nm) was applied to prepare the Ag-NPs. A silver plate (99.99% purity; Sigma Aldrich) was located in cubic cell containing 10 mL of EG and chitosan that the appropriate amounts of 0.2 g chitosan were dissolved separately 100 mL in distilled water at 60°C and stirred for 1 hr. Prior to ablation, the silver plate was cleaned by using an ultrasonic bath for 30 min, and it was immersed in the solution. The solution was magnetically stirred at room temperature during the ablation process to disperse the produced NPs. The laser output power 35 mJ/pulse was measured by the optical power detector. The laser beam was focused on the silver target by a 25 cm focal length lens. The ablation was carried out at room temperature for 30 min. The same experiment has repeated for DW as the solvent as a making reference to measure. The prepared samples have been characterized using a UV-visible, double beam photospectrometer (UV-1650 PC, Shimadzu) with 1 cm optical path cell, transmission electron microscopy (TEM,

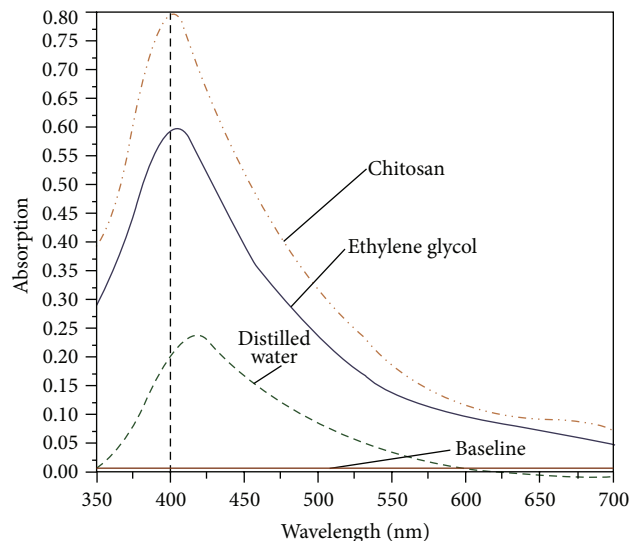


FIGURE 2: UV-visible absorption spectra of Ag-NPs prepared for 30 min ablation times in EG, chitosan, and DW.

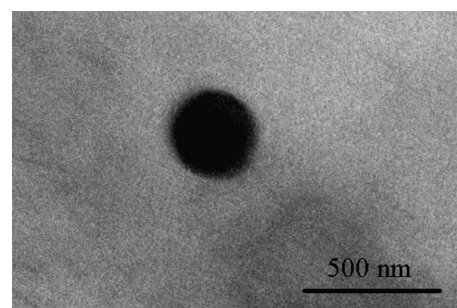


FIGURE 3: TEM images of Ag-NPs in ethylene glycol.

Hitachi H-7100; Hitachi) at 120 KV accelerating voltages, and Fourier transform infrared (FT-IR) spectrometer (1650; Perkin Elmer, Waltham, MA).

3. Results and Discussion

The solutions are observed to change color from its colorless and transparent form to slightly yellowish one after a few minutes during the ablation of the silver plate. The dark yellow will be achieved for higher concentration. This was also confirmed by UV-visible absorption spectra. Figure 2 indicates the optical absorption spectra of the solutions containing Ag-NPs. The peak at 400 nm is the signature of plasmon peak of Ag-NPs, which confirmed the Ag-NPs, and was formed inside the aqueous media. To compare with DW the peak intensity increase [22] and had a blue shift toward high energy, which shows an increase in the formation efficiency of the NPs and indicates a reduction of particle size following the Mie theory [23]. Furthermore, the spectrum peaks at this wavelength signify that the NPs in the solutions are spherical which is confirmed by TEM results shown in Figures 3 and 4 [24]. From Figure 2, the intensity of absorption peak at 400 nm was increased that can conclude

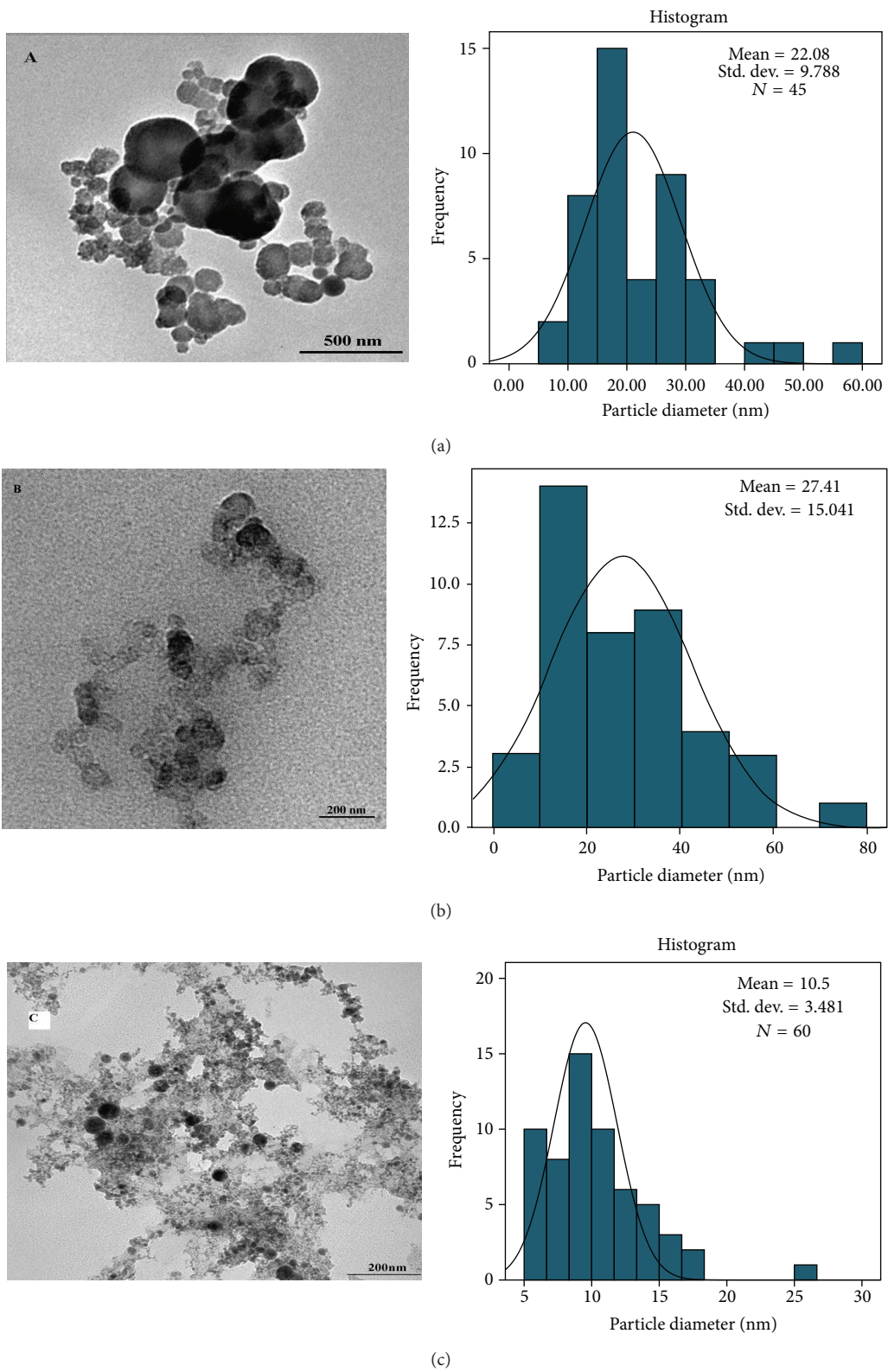


FIGURE 4: TEM image and typical of statistical graph for Ag-NPs produced in (a) EG, (b) in DW, and (c) in chitosan under 30 min ablation times in temperature room.

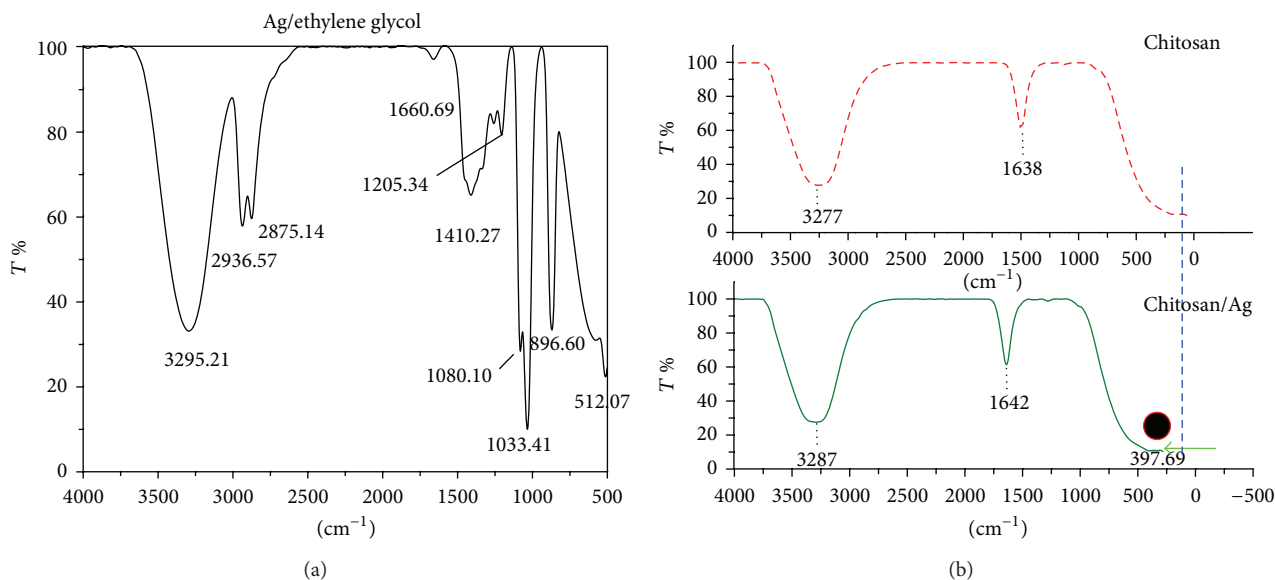


FIGURE 5: FT-IR spectra of Ag-NPs in (a) EG and (b) chitosan using LA.

the number of generated NPs was also increased. The increase of formation efficiency is due to the increment of the density and viscosity of solvent.

In contrast, in Figure 4(a) size reduction can be explained by the interaction between the EG molecules and laser products. In this step silver atoms interact with EG molecules; therefore the initial silver particles are formed because of this interatomic interaction. The mechanism of protecting particles from aggregation by EG can be explained by the hydroxyl group. In the fact of competition, the EG molecules now can absorb particles and prevent them from aggregation and growth [25]. On the other hand, Figure 4(c) shows Ag-NPs in chitosan and their corresponding size distribution that the obtained mean particle size is about 10.5 nm. Referring to Figure 4(c), TEM analysis also indicates that Ag-NPs are well dispersed with spherical morphology and there is no evidence of agglomeration.

Figures 3 and 4 depict the TEM images that Figure 3 indicates the spherical shape of Ag-NPs [26]. This type of NPs shape is suitable for drug loading and most biological applications, such as antibacterial properties [27]. Measurements of the mean size of Ag-NPs are 22.08 nm in EG and are about 10.5 nm in chitosan and the mean size of Ag-NPs is 27.41 nm in DW which ablation time for all cases completed in 30 min. Indeed, confirms the observation of particle size decrement with respect to the media as shown in Table 1. The formation efficiency of NPs in chitosan is higher than in EG and that in EG is higher than in DW (chitosan > EG > DW) due to the confinement on the Ag plate produced by ablation and it becomes stronger with the increase of solvent density and viscosity. In this case, chitosan has higher density and viscosity than other solutions; for these reasons the effect of size decrement for Ag-NPs is observed. The plasma is generated close to the plate with high pressure, which is confined surface, and it can etch the surface to make NPs [28, 29]. The procedure called secondary ablation [30] can

TABLE 1: Particle size of Ag-NPs with their standard deviation for particle of size (nm) in ethylene glycol and distilled water.

Ablation time (min)	Media	Particle size (nm)	Standard deviation (nm)
30	Ethylene glycol	22.08	9.788
30	Distilled water	27.41	15.041
30	Chitosan	10.50	3.481

improve efficiency of the formation of Ag-NPs. The other interesting point that can be observed from Figure 2 is that, by increasing the efficiency of formation of NPs due to increase of the density and viscosity of aqueous media, the plasmon peak also shifts toward higher energies. According to Mie's theory, the blue shift of spectra shows that the particle sizes were decreased.

Infrared spectroscopy, IR radiation is passed through a sample. Some of the infrared radiation is absorbed by the sample and some of it is passed through (transmitted). The resulting spectrum represents the molecular absorption and transmission, creating a molecular fingerprint of the sample. FT-IR spectra in Figure 5 confirm the formation of Ag NPs inside the solutions. The spectrum in Figure 5(a) indicates absorption peak at about 512.07 cm^{-1} which is a signature of Ag-NPs bonding with oxygen from hydroxyl groups [31] and Figure 6 shows the mechanism of protecting particles from aggregation by this stabilizer. The absorption peaks at about $3296.48, 1660.69\text{ cm}^{-1}$ which presented O-H groups. Furthermore, the peaks in $2936.57, 2875.14\text{ cm}^{-1}$ were assigned to symmetric and asymmetric of C-H₂ stretching [32] the band at 1410.27 cm^{-1} corresponds to C-H₂ bending. However, the peak at 1205.34 cm^{-1} corresponds to C-H stretching [31] and the peak at 1080.10 cm^{-1} indicates the bending of C-C-O [32].

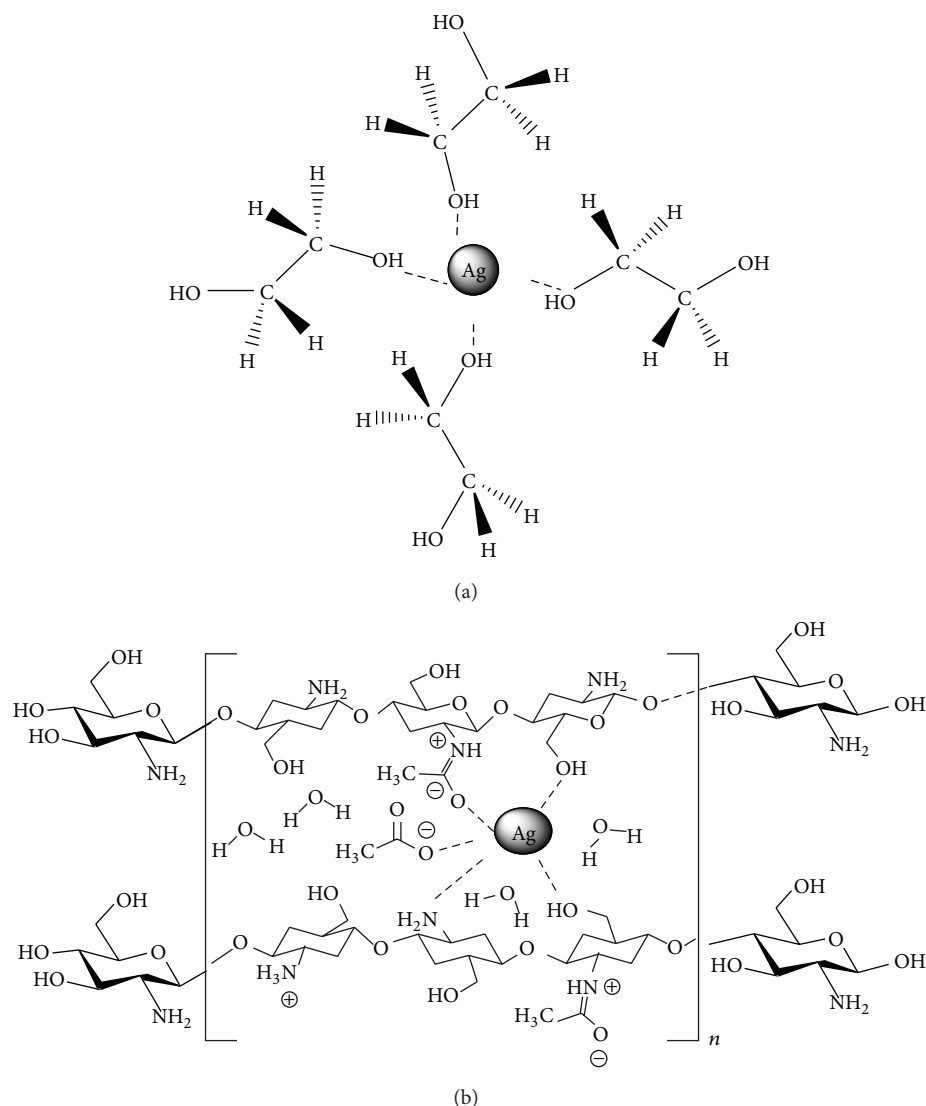


FIGURE 6: Mechanism of capping Ag-NPs by (a) ethylene glycol and (b) chitosan.

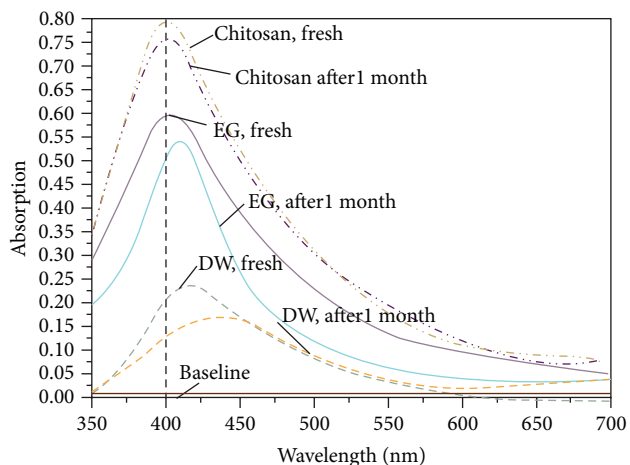


FIGURE 7: UV-visible absorption spectra of Ag-NPs in EG, DW, and chitosan for freshly prepared and after 1 month.

In competition, the chitosan molecules can absorb particles and prevent their aggregation and growth [33]. The mechanism of protecting particles from aggregation by chitosan can be explained by those nitrogen atoms of amino group in chitosan which hold a free electron doublet that is responsible for the uptake of NPs by chelating mechanism [34]. Some researchers have attributed a key role to the amine in the Ag⁺ reduction due to its decrease in the potential of Ag⁺/Ag (EAg⁺/Ag) promoting the reaction [32]. However, there is still no substantial evidence that confirms this assumption.

As well, the UV-visible spectra of the Ag-NPs in EG, chitosan, and the water were measured after 1 month to investigate the capability of fluids as a stabilizer. The absorption spectrum in Figure 7 does not show a significant change in the fresh sample compared to old sample in chitosan, but a large reduction can be seen in EG and water. It shows the

Ag-NPs in chitosan were stable. Moreover, there is a red shift which indicates some agglomeration of the Ag-NPs in EG and water; hence the vague descent in the absorption intensity is due to the slight sedimentation of the larger particles [35].

4. Conclusions

The synthesis of Ag-NPs in chitosan and EG using a LA technique was presented as a simple and green method. For a similar laser ablation time (30 min) the obtained particle size is smaller (10.5 nm) for chitosan than (22.08 nm) for EG and DW (27.41 nm). The particle size reduced with the effective solvent rather than with pure water. The obtained NPs are stable for quite a long time in chitosan because it controls the particle size and thus prevents agglomeration between the ablated NPs.

Conflict of Interests

The authors declare that there is no conflict of interests regarding the publication of this paper.

Acknowledgment

The authors gratefully acknowledged the financial support for this work from the Fundamental Research Grant Scheme (FRGS) of Project no. 01-02-13-1345FR.

References

- [1] J. Lin, S. F. Lim, S. Mahmood et al., *Synthesis and Characterization of FeCo Nanoparticle Colloid by Pulsed Laser Ablation in Distilled Water*, vol. 30, ECA, 2006.
- [2] C. Song, D. Wang, Y. Lin, Z. Hu, G. Gu, and X. Fu, "Formation of silver nanoshells on latex spheres," *Nanotechnology*, vol. 15, no. 8, pp. 962–965, 2004.
- [3] M. Kokkoris, C. C. Trapalis, S. Kossionides et al., "RBS and HIRBS studies of nanostructured AgSiO₂ sol-gel thin coatings," *Nuclear Instruments and Methods in Physics Research B: Beam Interactions with Materials and Atoms*, vol. 188, no. 1–4, pp. 67–72, 2002.
- [4] D. P. Dowling, A. J. Betts, C. Pope, M. L. McConnell, R. Eloy, and M. N. Arnaud, "Anti-bacterial silver coatings exhibiting enhanced activity through the addition of platinum," *Surface and Coatings Technology*, vol. 163–164, pp. 637–640, 2003.
- [5] J. W. Rhim, L. F. Wang, and S. I. Hong, "Preparation and characterization of agar/silver nanoparticles composite films with antimicrobial activity," *Food Hydrocolloids*, vol. 33, no. 2, pp. 327–335, 2013.
- [6] Z. S. Pillai and P. V. Kamat, "What factors control the size and shape of silver nanoparticles in the citrate ion reduction method?" *The Journal of Physical Chemistry B*, vol. 108, no. 3, pp. 945–951, 2004.
- [7] M. Brust, M. Walker, D. Bethell, D. J. Schiffrin, and R. Whyman, "Synthesis of thiol-derivatised gold nanoparticles in a two-phase liquid-liquid system," *Journal of the Chemical Society, Chemical Communications*, no. 7, pp. 801–802, 1994.
- [8] I. Pastoriza-Santos and L. M. Liz-Marzán, "Formation and stabilization of silver nanoparticles through reduction by *N,N*-dimethylformamide," *Langmuir*, vol. 15, no. 4, pp. 948–951, 1999.
- [9] F. Bonet, V. Delmas, S. Grugeon, R. H. Urbina, P.-Y. Silvert, and K. Tekaia-Elhsissen, "Synthesis of monodisperse Au, Pt, Pd, Ru and Ir nanoparticles in ethylene glycol," *Nanostructured Materials*, vol. 11, no. 8, pp. 1277–1284, 1999.
- [10] D. Habbalalu, J. Lalley, M. N. Nadagouda, and R. S. Varma, "Green techniques for the synthesis of silver nanoparticles using plant extracts, enzymes, bacteria, biodegradable polymers, and microwaves," *Sustainable Chemistry & Engineering*, vol. 1, pp. 703–712, 2013.
- [11] M. Yamamoto and M. Nakamoto, "Novel preparation of monodispersed silver nanoparticles via amine adducts derived from insoluble silver myristate in tertiary alkylamine," *Journal of Materials Chemistry*, vol. 13, no. 9, pp. 2064–2065, 2003.
- [12] V. Amendola, S. Polizzi, and M. Meneghetti, "Free silver nanoparticles synthesized by laser ablation in organic solvents and their easy functionalization," *Langmuir*, vol. 23, no. 12, pp. 6766–6770, 2007.
- [13] V. Amendola and M. Meneghetti, "Laser ablation synthesis in solution and size manipulation of noble metal nanoparticles," *Physical Chemistry Chemical Physics*, vol. 11, no. 20, pp. 3805–3821, 2009.
- [14] N. Wu, L. Fu, M. Su, M. Aslam, K. C. Wong, and V. P. Dravid, "Interaction of fatty acid monolayers with cobalt nanoparticles," *Nano Letters*, vol. 4, no. 2, pp. 383–386, 2004.
- [15] H.-T. Song, J.-S. Choi, Y.-M. Huh et al., "Surface modulation of magnetic nanocrystals in the development of highly efficient magnetic resonance probes for intracellular labeling," *Journal of the American Chemical Society*, vol. 127, no. 28, pp. 9992–9993, 2005.
- [16] E. Canada and H. Canada, Canadian Environmental Protection Act, 2000.
- [17] M. W. Forkner, J. H. Robson, W. M. Snelling, A. E. Martin, F. H. Murphy, and T. E. Parsons, *Glycols–Ethylene Glycols*, SIAM, 2004.
- [18] R. Gomes, R. Liteplo, and M. E. Meek, CICADS 45, World Health Organization, Geneva, Switzerland, 2002.
- [19] R. A. Ganeev, M. Baba, A. I. Rysanyansky, M. Suzuki, and H. Kuroda, "Characterization of optical and nonlinear optical properties of silver nanoparticles prepared by laser ablation in various liquids," *Optics Communications*, vol. 240, no. 4–6, pp. 437–448, 2004.
- [20] P. K. Dutta, J. D. Duta, and V. S. Tripathi, "Chitin and chitosan: chemistry, properties and applications," *Journal of Scientific & Industrial Research*, vol. 63, no. 1, pp. 20–31, 2004.
- [21] R. Yoksan and S. Chirachanchai, "Silver nanoparticles dispersing in chitosan solution: preparation by γ -ray irradiation and their antimicrobial activities," *Materials Chemistry and Physics*, vol. 115, no. 1, pp. 296–302, 2009.
- [22] M. Kerker, "The optics of colloidal silver: something old and something new," *Journal of Colloid And Interface Science*, vol. 105, no. 2, pp. 297–314, 1985.
- [23] R. Zamiri, B. Z. Azmi, A. R. Sadrolhosseini, H. A. Ahangar, A. W. Zaidan, and M. A. Mahdi, "Preparation of silver nanoparticles in virgin coconut oil using laser ablation," *International Journal of Nanomedicine*, vol. 6, no. 1, pp. 71–75, 2011.
- [24] T. Tsuji, K. Iryo, N. Watanabe, and M. Tsuji, "Preparation of silver nanoparticles by laser ablation in solution: influence of laser wavelength on particle size," *Applied Surface Science*, vol. 202, no. 1–2, pp. 80–85, 2002.
- [25] F. Mafuné, J.-Y. Kohno, Y. Takeda, T. Kondow, and H. Sawabe, "Formation and size control of silver nanoparticles by laser

- ablation in aqueous solution,” *Journal of Physical Chemistry B*, vol. 104, no. 39, pp. 9111–9117, 2000.
- [26] F. Hajiesmaeilbaigi, A. Mohammadalipour, J. Sabbaghzadeh, S. Hoseinkhani, and H. R. Fallah, “Preparation of silver nanoparticles by laser ablation and fragmentation in pure water,” *Laser Physics Letters*, vol. 3, no. 5, pp. 252–256, 2006.
- [27] P. K. Khanna and C. K. K. Nair, “Synthesis of silver nanoparticles using cod liver oil (fish oil): green approach to nanotechnology,” *International Journal of Green Nanotechnology: Physics and Chemistry*, vol. 1, pp. 3–9, 2009.
- [28] Y. Kawaguchi, X. Ding, A. Narazaki, T. Sato, and H. Niino, “Transient pressure induced by laser ablation of toluene, a highly laser-absorbing liquid,” *Applied Physics A*, vol. 80, no. 2, pp. 275–281, 2005.
- [29] Y. Tomita, P. B. Robinson, R. P. Tong, and J. R. Blake, “Growth and collapse of cavitation bubbles near a curved rigid boundary,” *Journal of Fluid Mechanics*, vol. 466, pp. 259–283, 2002.
- [30] A. V. Kabashin and M. Meunier, “Synthesis of colloidal nanoparticles during femtosecond laser ablation of gold in water,” *Journal of Applied Physics*, vol. 94, no. 12, pp. 7941–7943, 2003.
- [31] K. Shameli, M. B. Ahmad, S. D. Jazayeri et al., “Synthesis and characterization of polyethylene glycol mediated silver nanoparticles by the green method,” *International Journal of Molecular Sciences*, vol. 13, no. 6, pp. 6639–6650, 2012.
- [32] L. Ramajo, R. Parra, M. Reboredo, and M. Castro, “Preparation of amine coated silver nanoparticles using triethylenetetramine,” *Journal of Chemical Sciences*, vol. 121, no. 1, pp. 83–87, 2009.
- [33] F. Mafuné, J.-Y. Kohno, Y. Takeda, and T. Kondow, “Formation and size control of silver nanoparticles by laser ablation in aqueous solution,” *The Journal of Physical Chemistry B*, vol. 104, no. 39, pp. 9111–9117, 2000.
- [34] S. S. Silva, R. A. S. Ferreira, L. Fu et al., “Functional nanostructured chitosan-siloxane hybrids,” *Journal of Materials Chemistry*, vol. 15, no. 35–36, pp. 3952–3961, 2005.
- [35] R. Zamiri, A. Zakaria, H. Abbastabar, M. Darroudi, M. S. Husin, and M. A. Mahdi, “Laser-fabricated castor oil-capped silver nanoparticles,” *International Journal of Nanomedicine*, vol. 6, no. 1, pp. 565–568, 2011.

Research Article

Green Nanoparticles for Mosquito Control

Namita Soni and Soam Prakash

Advance and Environmental Parasitology, Vector Control Biotechnology and Biomedical Laboratories, Department of Zoology, Faculty of Science, Dayalbagh Educational Institute, Dayalbagh, Agra 282 110, India

Correspondence should be addressed to Soam Prakash; soamprakashdayalbagh@gmail.com

Received 18 June 2014; Revised 7 July 2014; Accepted 7 July 2014; Published 27 August 2014

Academic Editor: Xiao-Feng Zhao

Copyright © 2014 N. Soni and S. Prakash. This is an open access article distributed under the Creative Commons Attribution License, which permits unrestricted use, distribution, and reproduction in any medium, provided the original work is properly cited.

Here, we have used the green method for synthesis of silver and gold nanoparticles. In the present study the silver (Ag) and gold (Au) nanoparticles (NPs) were synthesized by using the aqueous bark extract of Indian spice dachshin (*Cinnamomum zeylanicum*) (*C. zeylanicum* or *C. verum* J. Presl). Additionally, we have used these synthesized nanoparticles for mosquito control. The larvicidal activity has been tested against the malaria vector *Anopheles stephensi* and filariasis vector *Culex quinquefasciatus*. The results were obtained using UV-visible spectrophotometer and the images were recorded with a transmission electron microscope (TEM). The efficacy tests were then performed at different concentrations and varying numbers of hours by probit analysis. The synthesized AgNPs were in spherical shape and average sizes (11.77 nm AgNPs and 46.48 nm AuNPs). The larvae of *An. stephensi* were found highly susceptible to the synthesized AgNPs and AuNPs than the *Cx. quinquefasciatus*. These results suggest that the *C. zeylanicum* synthesized silver and gold nanoparticles have the potential to be used as an ideal ecofriendly approach for the control of mosquito.

1. Introduction

Cinnamon is a small evergreen tree, which belongs to family Lauraceae. It is the native of Sri Lanka and Southern India. It has antioxidant, antimicrobials, mosquito control, and other properties [1]. Mosquitoes are vectors of many diseases, including malaria, filariasis, dengue, and Japanese encephalitis. Among these kinds of malaria, spread by the bite of female *Anopheles* mosquito, and filariasis, spread by *Culex* mosquito, are the two vector borne diseases of the tropical region and are considered major public health concerns.

According to WHO, there were about 219 million cases of malaria in 2010 (with an uncertainty range of 154 million to 289 million) and an estimated 660,000 deaths (with an uncertainty range of 490,000 to 836,000). Malaria mortality rate has fallen by more than 25% globally since 2000 and by 33% in the WHO African region. Most deaths occur among children living in Africa, where malaria claims the life of a child every minute. Country-level burden estimates available for 2010 show that an estimated 80% of malaria deaths occur in just 14 countries and about 80% of cases occur in 17 countries. Together, the Democratic Republic of the Congo

and Nigeria account for over 40% of the total estimated malaria deaths globally [2].

On the other hand, nearly, 1.4 billion people in 73 countries worldwide are threatened by lymphatic filariasis, commonly known as elephantiasis. Over 120 million people are currently infected, with about 40 million disfigured and incapacitated by the disease [3]. Control or eradication of the mosquito population could significantly restrict the spread of disease.

Synthesizing nanoparticles using plants and microorganisms can eliminate this problem by making the nanoparticles more biocompatible. The synthesis of silver nanoparticles from silver precursor using the bark extract and powder of novel *Cinnamomum zeylanicum* has been reported [4]. The potential of nanocrystalline palladium particle production using *Cinnamomum zeylanicum* (*C. zeylanicum* or *C. verum* J. Presl) bark extract has been studied [5].

The silver and gold nanoparticles using *A. calamus* [6], *E. sativa* and *S. oleracea* [7], *T. conoides* [8], and *A. nilotica* [9] have been synthesized.

The larvicidal activity of biosynthesized silver nanoparticles using the leaf extracts of *P. pinnata* [10] and *L. aspera* [11]

has been tested against the dengue vector *Ae. albopictus* and *Ae. aegypti*.

In the present investigation we have synthesized the AgNPs and AuNPs nanoparticles by using the bark extract of *C. zeylanicum*. Further, the synthesized nanoparticles have also been tested against the larvae of *Anopheles stephensi* and *Culex quinquefasciatus*. The *C. zeylanicum* synthesized AgNPs and AuNPs have the potential to be used as an ideal ecofriendly approach for the control of mosquito.

2. Materials and Methods

2.1. Material. The bark of *Cinnamomum zeylanicum* (*C. zeylanicum* or *C. verum* J. Presl) was collected from the local market of Agra, India. The voucher specimen is maintained in our laboratory for future use.

2.2. Extract Preparation. The bark of *Cinnamomum zeylanicum* (*C. zeylanicum* or *C. verum* J. Presl) was washed with distilled water for removing the dust particles. The bark was air-dried and converted into powder and a bark broth was prepared by placing 10 g of bark powder in a 250 mL of deionized water. This mixture was boiled at 60°C, for 5 min, decanted, or filtered through Whatman-1 filter paper.

2.3. Nanoparticles Synthesis. After obtaining the aqueous extract of bark, the filtrates were treated with aqueous 1 mM AgNO₃ and HAuCl₄ solutions in an Erlenmeyer flask and incubated at room temperature. Formation of AgNPs and AuNPs was indicated by the dark brown and purple coloration of the solutions.

2.4. Characterization of Nanoparticles. Synthesis of AgNPs and AuNPs was confirmed by sampling the reaction mixture at regular intervals, and the absorption maxima were scanned by UV-Vis spectra, at the wavelength of 350–750 nm in a UV-3600 Shimadzu spectrophotometer at 1 nm resolution. The micrographs of AgNPs and AuNPs were obtained by TECHNAI 200 Kv TEM (Fei, Electron Optics) transmission electron microscope. For transmission electron microscopy analysis, samples were prepared on carbon coated copper TEM grids.

2.5. Rearing of Mosquito Larvae. The larvae of *Cx. quinquefasciatus* and *An. stephensi* were collected from various localities including urban, rural, and semiurban regions of Agra (27°, 10'N, 78°05'E), India. The larvae were reared in deionized water containing glucose and yeast powder. The colonies of *Cx. quinquefasciatus* and *An. stephensi* were maintained in the laboratory at a temperature of 25°C with a relative humidity of 75 ± 5% and 14 h of photoperiod. The larvae of *Cx. quinquefasciatus* and *An. stephensi* were maintained in separate enamel containers as per the standard method [12].

2.6. Bioassays, Data Management, and Statistical Analysis. AgNPs and AuNPs synthesized from *Cinnamomum zeylanicum* (*C. zeylanicum* or *C. verum* J. Presl) were tested for their

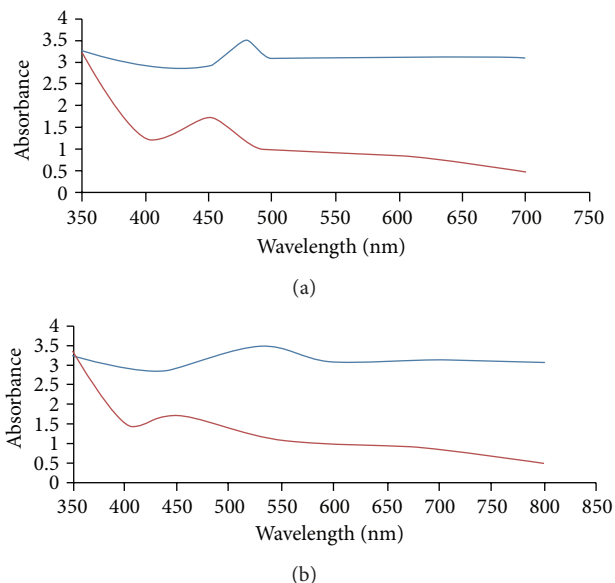


FIGURE 1: UV-Vis spectra of (a) silver nanoparticles and (b) gold nanoparticles synthesized by using the bark extract of *Cinnamomum zeylanicum* recorded from reaction medium before (1) and after immersion of AgNO₃ (2) after 24 h.

killing activities against the larvae of *Cx. quinquefasciatus* and *An. stephensi* and were assessed by using the standard method [13]. All larvae of *Cx. quinquefasciatus* and *An. stephensi* were separated and placed in a container in microbe-free deionized water. After that, different test concentrations of AgNPs and AuNPs in 100 mL deionized water were prepared in 250 mL beakers. Bioassays were conducted separately for each instar at five different concentrations of aqueous AgNPs and AuNPs (2, 4, 6, 8, 10 ppm). To test the larvicidal activity of our AgNPs and AuNPs, 20 larvae of each stage were separately exposed to 100 mL of test concentrations. Thereafter, we examined their mortality after different time of treatment during the experimental periods.

The data on the efficacy were subjected to probit analysis [14]. The control mortality was corrected by Abbott's formula [15].

3. Results

3.1. Analysis of UV-Vis Spectra. The aqueous extracts of bark of *C. zeylanicum* (*C. zeylanicum* or *C. verum* J. Presl) were light yellow and brown in colour before immersion in AgNO₃ and HAuCl₄ solutions. The colour of bark aqueous extract changed into dark red and purple colour after immersing in AgNO₃ and HAuCl₄ solutions after 72 h of incubation. The change in colour is a signal for the formation of AgNPs and AuNPs. Figures 1(a) and 1(b) show the UV-Vis spectra of synthesized AgNPs and AuNPs using the bark of *C. zeylanicum* (*C. zeylanicum* or *C. verum* J. Presl) recorded from reaction medium before (1) and after immersion of AgNO₃ and HAuCl₄ (2) after 72 h. Absorption spectra of AgNPs

TABLE 1: Efficacy of silver nanoparticles and gold nanoparticles synthesized by bark extract of *Cinnamomum zeylanicum* against the larvae of *Anopheles stephensi* with their LC values, 95% confidential limits (CL), and χ^2 and r values after different time of exposure.

NPs	Instar	Time	LC ₅₀ (95% CL)	LC ₉₀ (95% CL)	LC ₉₉ (95% CL)	χ^2	r
AgNPs	1st	4 h	2 (0.86–3.14)	11 (9.77–12.23)	12 (10.54–13.46)	50.29	0.82
	2nd	4 h	10 (8.86–11.14)	15 (13.77–16.23)	17 (15.54–18.46)	39.43	0.95
	3rd	22 h	6 (4.86–7.16)	11 (9.77–12.23)	13 (11.54–14.46)	43.83	0.95
	4th	22 h	10 (8.86–11.14)	15 (13.83–16.17)	17 (15.77–18.77)	37.66	0.89
AuNPs	1st	24 h	**	**	**	**	**
	2nd	24 h	1 (0.86–2.14)	8 (6.83–9.17)	10.5 (9.27–11.73)	61.61	0.91
	3rd	72 h	1 (0.86–2.14)	8 (6.83–9.17)	10.5 (9.27–11.73)	61.61	0.91
	4th	72 h	2 (0.88–3.12)	10 (8.86–11.14)	11 (9.87–12.13)	54.93	0.89

**100% mortality.

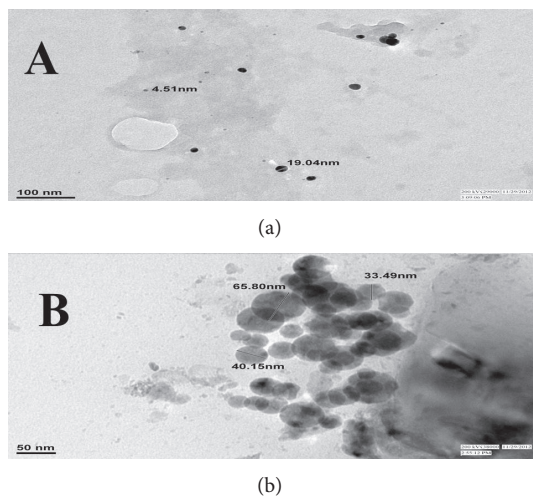


FIGURE 2: TEM micrographs of *Cinnamomum zeylanicum* synthesized (a) silver nanoparticles and (b) gold nanoparticles.

and AuNPs formed in the reaction medium have a broad absorption band centred at 480 nm and 530 nm c.a.

3.2. TEM Analysis. Figures 2(a) and 2(b) show the TEM micrographs of synthesized AgNPs and AuNPs. The average size of AgNPs is 11.77 nm and AuNPs 46.48 nm and they were spherical-shaped.

3.3. Efficacy of Synthesized AgNPs and AuNPs against *An. stephensi* Larvae. The efficacy of the synthesized AgNPs and AuNPs was tested against the larvae of *An. stephensi*. Different concentrations of aqueous AgNPs and AuNPs (2, 4, 6, 8, 10 ppm) were tested against the larvae of *An. stephensi*.

The larvae of *An. stephensi* were found highly susceptible to the synthesized AgNPs. First instar larvae (LC₅₀ 2, LC₉₀ 11, and LC₉₉ 12 ppm), second instar larvae (LC₅₀ 10, LC₉₀ 15, and LC₉₉ 17 ppm) after 4 h, third instar larvae (LC₅₀ 6, LC₉₀ 11, and LC₉₉ 13 ppm), and fourth instar larvae (LC₅₀ 10, LC₉₀ 15, and LC₉₉ 17 ppm) after 22 h of exposure were obtained with their confidence limits and χ^2 and r values (Table 1).

The larvae of *An. stephensi* were found susceptible to the synthesized AuNPs. The first instar larvae have shown

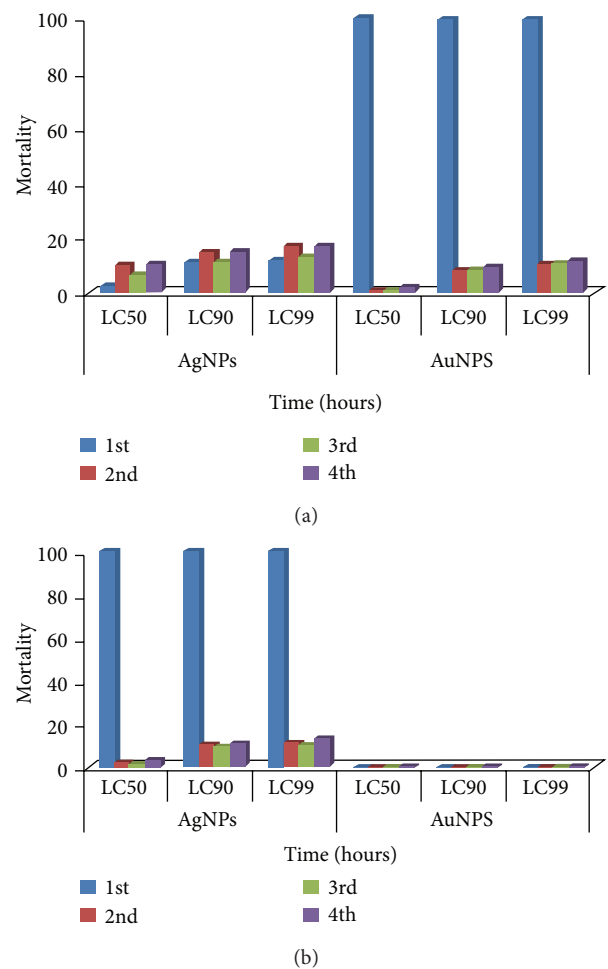


FIGURE 3: Efficacy of silver and gold nanoparticles against the larvae of *Anopheles stephensi* at different hours of exposure.

the 100% mortality after 24 h of exposure. The second instar larvae (LC₅₀ 1, LC₉₀ 8, and LC₉₉ 10.5 ppm) after 24 h, third instar larvae (LC₅₀ 1, LC₉₀ 8, and LC₉₉ 10.5 ppm), and fourth instar larvae (LC₅₀ 2, LC₉₀ 10, and LC₉₉ 11 ppm) after 72 h of exposure were obtained with their confidence limits and χ^2 and r values (Table 1, Figure 3(a)).

TABLE 2: Efficacy of silver nanoparticles and gold nanoparticles synthesized by bark extract of *Cinnamomum zeylanicum* against the larvae of *Culex quinquefasciatus* with their LC values, 95% confidential limits (CL), and χ^2 and r values after different time of exposure.

NPs	Instar	Time	LC ₅₀ (95% CL)	LC ₉₀ (95% CL)	LC ₉₉ (95% CL)	χ^2	r
	1st	24 h	**	**	**	**	**
AgNPs	2nd	24 h	2 (0.88–3.12)	10 (8.86–11.14)	11 (9.87–12.13)	54.93	0.89
	3rd	24 h	1.5 (1.36–2.64)	9 (7.77–10.23)	10.5 (9.17–11.83)	58.85	0.85
	4th	24 h	4 (2.86–5.14)	11 (9.77–12.23)	13 (11.54–14.46)	49.41	0.87
AuNPs	Larvae	24 h	—	—	—	—	—

**100% mortality.

—no mortality.

3.4. Efficacy of Synthesized AgNPs and AuNPs against *Cx. quinquefasciatus* Larvae. The efficacy of the synthesized AgNPs and AuNPs was tested against the larvae of *Cx. quinquefasciatus*. Different concentrations of aqueous AgNPs and AuNPs (2, 4, 6, 8, 10 ppm) were tested against the larvae of *Cx. quinquefasciatus*.

The larvae of *Cx. quinquefasciatus* were found highly susceptible to the synthesized AgNPs. The first instar larvae have shown the 100% mortality after 24 h of exposure. The second instar larvae (LC₅₀ 2, LC₉₀ 10, and LC₉₉ 11 ppm), third instar larvae (LC₅₀ 1.5, LC₉₀ 9, and LC₉₉ 10.5 ppm), and fourth instar larvae (LC₅₀ 4, LC₉₀ 11, and LC₉₉ 13 ppm) after 24 h of exposure were obtained with their confidence limits and χ^2 and r values (Table 2).

The larvae of *Cx. quinquefasciatus* were found less susceptible to the synthesized AuNPs. No mortality was observed after 24 h of exposure (Table 2, Figure 3(b)).

4. Discussion

In the present investigation we have synthesized the AgNPs and AuNPs by using the bark of *C. zeylanicum* (*C. zeylanicum* or *C. verum* J. Presl). The efficacy of synthesized NPs has been tested against the larvae of malaria vector *An. stephensi* and filariasis vector *Cx. quinquefasciatus*.

An economically viable and “green chemistry” approach for biological synthesis of silver nanoparticles using aqueous leaf extract of *P. dulce* has been reported as larvicidal activity against the *Cx. quinquefasciatus* previously [16]. The larvicidal activity of biogenic nanoparticles against filariasis causing *Culex* mosquito vector has also been evaluated before [17].

Larvicidal activity of silver nanoparticles (AgNPs) using leaf extract of *N. oleander* (Apocynaceae) against the first to the fourth instar larvae and pupae of malaria vector, *An. stephensi* (Diptera: Culicidae), was carried out in an earlier study [18]. The fabrication, characterization, and mosquito larvicidal bioassay of silver nanoparticles synthesized from aqueous fruit extract of *Putranjiva* and *D. roxburghii* were observed [19]. Moreover, the activity of silver nanoparticles (AgNPs) synthesized using *M. koenigii* plant leaf extract against the first to the fourth instars larvae and pupae of *An. stephensi* and *Ae. aegypti* was determined, too [20]. Among these previous studies, the silver nanoparticles were synthesized by using the aqueous extract of leaf and other parts of plant extract and nanoparticles were tested against

the first and the fourth instar larvae and pupae of mosquitoes. However, in the present study we have synthesized silver and gold nanoparticles by using aqueous extracts of bark of *C. zeylanicum* (*C. zeylanicum* or *C. verum* J. Presl). These nanoparticles were tested as larvicide against *An. stephensi* and *Cx. quinquefasciatus*.

Recently, the larvicidal activity of silver nanoparticles synthesized by leaf extract of *P. pinnata* has been tested against the larvae of dengue vector *Ae. albopictus* [10]. Further, the larvicidal potential of silver nanoparticles synthesized from *L. aspera* leaf extract has been tested against the dengue vector *Ae. aegypti* [11]. However, the larvicidal activity of silver nanoparticles (AgNPs) synthesized using *F. elephantum* plant leaf extract against late third instar larvae of *An. stephensi*, *Ae. aegypti*, and *Cx. quinquefasciatus* has been determined [21]. Furthermore, activity of aqueous leaf extract and silver nanoparticles (AgNPs) synthesized using *H. indicum* plant leaves against late third instar larvae of *Ae. aegypti*, *An. Stephensi*, and *Cx. quinquefasciatus* has been studied [22]. Larvicidal activity of silver nanoparticles synthesized from aqueous leaf extract of *C. collinus* against the larvae of *Ae. aegypti* has now been determined [23], while in our study we have synthesized silver nanoparticles by using aqueous extracts of bark of *C. zeylanicum* (*C. zeylanicum* or *C. verum* J. Presl). These nanoparticles were tested as larvicide against *An. stephensi* and *Cx. quinquefasciatus*.

The larvicidal activities of synthesized cobalt nanoparticles using the biocontrol agent, *B. thuringiensis*, have been investigated against the malaria vector *An. subpictus* and dengue vector, *Ae. aegypti* [24]. Furthermore, the larvicidal activity of silver nanoparticles synthesized by using *B. thuringiensis* has been revealed against the *Ae. aegypti* [25], whereas in the present study we have tested the larvicidal activity of silver and gold nanoparticles synthesized by using aqueous extracts of bark of *C. zeylanicum* (*C. zeylanicum* or *C. verum* J. Presl). These nanoparticles were tested as larvicide against *An. stephensi* and *Cx. quinquefasciatus*.

Efficacy of fungus mediated silver and gold nanoparticles has been tested against the larvae of *An. stephensi*, *Cx. Quinquefasciatus*, and *Ae. aegypti* [26–28]. Furthermore, the larvicidal and pupicidal activities of silver and gold nanoparticles synthesized by fungi have also been investigated against *An. stephensi*, *Cx. Quinquefasciatus*, and *Ae. aegypti* [29–31]. Recently the silver nanoparticles have been synthesized by using the leaf and stem of *Piper nigrum* for their antibacterial activity against agriculture plant pathogens [32]. The silver

nanoparticles have synthesized by using the leaf of *Pimenta dioica* [33]. However, in the present study the silver and gold nanoparticles have been synthesized by bark of *C. zeylanicum* against the larvae of *An. stephensi* and *Cx. quinquefasciatus*.

5. Conclusion

In this study we have synthesized the silver and gold nanoparticles by using the bark of *Cinnamomum zeylanicum* (*C. zeylanicum* or *C. verum* J. Presl). The larvicidal activity of the synthesized nanoparticles has been tested against the larvae of malaria vector *Anopheles stephensi* and filariasis vector *Culex quinquefasciatus*. The synthesized AgNPs were in spherical shape and average sizes (11.77 nm AgNPs, 46.48 nm AuNPs). The synthesized nanoparticles were found effective against the larvae of mosquito species. The results suggest that the *C. zeylanicum* (*C. zeylanicum* or *C. verum* J. Presl) synthesized silver and gold nanoparticles have the potential to be used as an ideal ecofriendly approach for the control of mosquito.

Conflict of Interests

The authors declare that there is no conflict of interests regarding the publication of this paper.

Acknowledgments

The authors sincerely thank Professor P. S. Satsangi Sahab, Chairman, of Advisory Committee on Education, Dayalbagh Educational Institute, and Professor P. K. Kalra, Director, Dayalbagh Educational Institute, for providing support and encouragements for the work. They also thank to UGC, New Delhi, Major Research Project (39-599/2010), for financial support.

References

- [1] S. S. Lal and P. L. Nayak, "Green synthesis of gold nanoparticles using various extract of plants and species," *International Journal of Science Innovations and Discoveries*, vol. 2, no. 23, pp. 325–350, 2012.
- [2] World Health Organization, "Malaria," 2013, <http://www.who.int/mediacentre/factsheets/fs094/en/index.html>.
- [3] World Health Organization, "Lymphatic filariasis," 2013, <http://www.who.int/mediacentre/factsheets/fs102/en/>.
- [4] M. Sathishkumar, K. Sneha, S. W. Won, C.-W. Cho, S. Kim, and Y.-S. Yun, "Cinnamon zeylanicum bark extract and powder mediated green synthesis of nano-crystalline silver particles and its bactericidal activity," *Colloids and Surfaces B: Biointerfaces*, vol. 73, no. 2, pp. 332–338, 2009.
- [5] M. Sathishkumar, K. Sneha, I. S. Kwak, J. Mao, S. J. Tripathy, and Y.-S. Yun, "Phyto-crystallization of palladium through reduction process using *Cinnamom zeylanicum* bark extract," *Journal of Hazardous Materials*, vol. 171, no. 1–3, pp. 400–404, 2009.
- [6] S. Dhanashekar, S. Karunakaran, R. Amutha, S. Suruthipariyadarshini, and K. Jayalakshmi, "Biosynthesis of silver nanoparticles using *Aroclus calamus* and its antibacterial activity," *International Journal of Nanomaterials and Biostructures*, vol. 4, no. 1, pp. 16–20, 2014.
- [7] I. A. Alaraidh, M. M. Ibrahim, and G. A. El-Gaaly, "Evaluation of green synthesis of Ag nanoparticles using *Eruca sativa* and *Spinacia oleracea* leaf extracts and their antimicrobial activity," *Iranian Journal of Biotechnology*, vol. 12, no. 1, Article ID e12392, 2014.
- [8] S. R. Vijayan, P. Santhiyagu, M. Singamuthu, N. K. Ahila, R. Jayaraman, and K. Ehiraj, "Synthesis and characterization of silver and gold nanoparticles using aqueous extract of seaweed, *Turbinaria conoides*, and their antimicrofouling activity," *The Scientific World Journal*, vol. 2014, Article ID 938272, 10 pages, 2014.
- [9] C. H. Prasad, S. Gangadhara, S. Venkateswarlu, N. V. V. Jyothi, and P. Venkateswarlu, "Green synthesis of silver nanoparticles/microparticles using extract of *Acacia nilotica* seeds and their characterization," *International Journal of Nanomaterials and Biostructures*, vol. 4, no. 1, pp. 1–4, 2014.
- [10] B. R. Naik, G. S. Gowreeswari, Y. Singh, R. Satyavathi, R. R. Daravath, and P. R. Reddy, "Bio-synthesis of silver nanoparticles from leaf extract of *Pongamia pinnata* as an effective larvicide on dengue vector *Aedes albopictus* (Skuse) (Diptera: Culicidae)," *Advances in Entomology*, vol. 2, pp. 93–101, 2014.
- [11] G. Suganya, S. Karthi, and M. S. Shivakumar, "Larvicidal potential of silver nanoparticles synthesized from *Lucas aspera* leaf extracts against dengue vector *Aedes aegypti*," *Parasitology Research*, vol. 113, no. 5, pp. 1673–1679, 2014.
- [12] E. J. Gerberg, D. R. Barnard, and R. A. Ward, "Manual for mosquito rearing and experimental techniques," *Journal of American Mosquito Control Association*, vol. 5, p. 98, 1994.
- [13] World Health Organization, *Guidelines for Laboratory and Field Testing of Mosquito Larvicides*, WHO/CDS/WHOPES/GCDPP/13, 2005.
- [14] D. J. Finney, *Probit Analysis*, Cambridge University Press, Cambridge, UK, 3rd edition, 1971.
- [15] W. S. Abbott, "A method of computing the effectiveness of an insecticide," *Journal of Economic Entomology*, vol. 18, no. 2, pp. 265–267, 1925.
- [16] N. Raman, S. Sudharsan, V. Veerakumar, N. Pravin, and K. Vithiya, "*Pithecellobium dulce* mediated extra-cellular green synthesis of larvicidal silver nanoparticles," *Spectrochimica Acta A: Molecular and Biomolecular Spectroscopy*, vol. 96, pp. 1031–1037, 2012.
- [17] D. Dhanasekaran and R. Thangaraj, "Evaluation of larvicidal activity of biogenic nanoparticles against filariasis causing *Culex* mosquito vector," *Asian Pacific Journal of Tropical Disease*, vol. 3, no. 3, pp. 174–179, 2013.
- [18] M. Roni, K. Murugan, C. Panneerselvam, J. Subramaniam, and J.-S. Hwang, "Evaluation of leaf aqueous extract and synthesized silver nanoparticles using *Nerium oleander* against *Anopheles stephensi* (Diptera: Culicidae)," *Parasitology Research*, vol. 112, no. 3, pp. 981–990, 2013.
- [19] K. M. Haldar, B. Haldar, and G. Chandra, "Fabrication, characterization and mosquito larvicidal bioassay of silver nanoparticles synthesized from aqueous fruit extract of putranjiva, *Drypetes roxburghii* (Wall.)," *Parasitology Research*, vol. 112, no. 4, pp. 1451–1459, 2013.
- [20] A. Suganya, K. Murugan, K. Kovendan, P. Mahesh Kumar, and J.-S. Hwang, "Green synthesis of silver nanoparticles using *Murraya koenigii* leaf extract against *Anopheles stephensi* and

- Aedes aegypti*," *Parasitology Research*, vol. 112, no. 4, pp. 1385–1397, 2013.
- [21] K. Veerakumar, M. Govindrajan, M. Rajeswary, and U. Muthukumaran, "Low-cost and eco-friendly green synthesis of silver nanoparticles using *Feronia elephantum* (Rutaceae) against *Culex quinquefasciatus*, *Anopheles stephensi*, and *Aedes aegypti* (Diptera: Culicidae)," *Parasitology Research*, vol. 113, pp. 1775–1785, 2014.
- [22] K. Veerakumar, M. Govindrajan, M. Rajeswary, and U. Muthukumaran, "Mosquito larvicidal properties of silver nanoparticles synthesized using *Heliotropium indicum* (Boraginaceae) against *Aedes aegypti*, *Anopheles stephensi*, and *Culex quinquefasciatus* (Diptera: Culicidae)," *Parasitology Research*, vol. 113, no. 6, pp. 2363–2373, 2014.
- [23] G. Ramar, T. Suman, R. Elangomathavan, and A. Jeyasankar, "Larvicidal activity of biologically synthesised silver nanoparticles against dengue vector *Aedes Aegypti* (Culicidae)," *Discovery*, vol. 9, pp. 65–68, 2014.
- [24] S. Marimuthu, A. A. Rahuman, A. V. Kirthi, T. Santhoshkumar, C. Jayaseelan, and G. Rajakumar, "Eco-friendly microbial route to synthesize cobalt nanoparticles using *Bacillus thuringiensis* against malaria and dengue vectors," *Parasitology Research*, vol. 112, no. 12, pp. 4105–4112, 2013.
- [25] A. N. Banu, C. Balasubramanian, and P. V. Moorthi, "Biosynthesis of silver nanoparticles using *Bacillus thuringiensis* against dengue vector, *Aedes aegypti* (Diptera: Culicidae)," *Parasitology Research*, vol. 113, no. 1, pp. 311–316, 2014.
- [26] N. Soni and S. Prakash, "Efficacy of fungus mediated silver and gold nanoparticles against *Aedes aegypti* larvae," *Parasitology Research*, vol. 110, no. 1, pp. 175–184, 2012.
- [27] N. Soni and S. Prakash, "Synthesis of gold nanoparticles by the fungus *Aspergillus niger* and its efficacy against mosquito larvae," *Reports in Parasitology*, vol. 2, pp. 1–7, 2012.
- [28] N. Soni and S. Prakash, "Entomopathogenic fungus generated Nanoparticles for enhancement of efficacy in *Culex quinquefasciatus* and *Anopheles stephensi*," *Asian Pacific Journal of Tropical Disease*, vol. 2, no. 1, pp. S356–S361, 2012.
- [29] N. Soni and S. Prakash, "Possible mosquito control by silver nanoparticles synthesized by soil fungus (*Aspergillus niger* 2587)," *Advances in Nanoparticles*, vol. 2, pp. 125–132, 2013.
- [30] N. Soni and S. Prakash, "Fungus generated novel nanoparticles: a new prospective for mosquito control," *International Journal of Recent Scientific Research*, vol. 4, pp. 1481–1487, 2013.
- [31] N. Soni and S. Prakash, "Microbial synthesis of spherical nanosilver and nanogold for mosquito control," *Annals of Microbiology*, vol. 64, no. 3, pp. 1099–1111, 2014.
- [32] K. Paulkumar, G. Gnanajobitha, M. Vanaja et al., "*Piper nigrum* leaf and stem assisted green synthesis of silver nanoparticles and evaluation of its antibacterial activity against agricultural plant pathogens," *The Scientific World Journal*, vol. 2014, Article ID 829894, 9 pages, 2014.
- [33] A. R. Geetha, E. George, A. Srinivasan, and J. Shaik, "Optimization of green synthesis of silver nanoparticles from leaf of *Pimenta dioica* (Allspice)," *The Scientific World Journal*, vol. 2013, Article ID 362890, 5 pages, 2013.

Research Article

Development of a Highly Biocompatible Antituberculosis Nanodelivery Formulation Based on Para-Aminosalicylic Acid—Zinc Layered Hydroxide Nanocomposites

Bullo Saifullah,¹ Palanisamy Arulselvan,² Mohamed Ezzat El Zowalaty,^{2,3} Sharida Fakurazi,^{2,4} Thomas J. Webster,^{5,6} Benjamin Geilich,⁵ and Mohd Zobir Hussein¹

¹ Materials Synthesis and Characterization Laboratory, Institute of Advanced Technology (ITMA), Universiti Putra Malaysia, 43400 Serdang, Selangor, Malaysia

² Laboratory of Vaccines and Immunotherapeutics, Institute of Bioscience, Universiti Putra Malaysia, 43400 Serdang, Selangor, Malaysia

³ Department of Environmental Health, Faculty of Public Health and Tropical Medicine, Jazan University, Jazan, Saudi Arabia

⁴ Department of Human Anatomy, Faculty of Medicine and Health Science, Universiti Putra Malaysia, 43400 Serdang, Selangor, Malaysia

⁵ Department of Chemical Engineering and Program in Bioengineering, Northeastern University, Boston, MA 02115, USA

⁶ Center of Excellence for Advanced Materials Research, King Abdulaziz University, Jeddah 21589, Saudi Arabia

Correspondence should be addressed to Mohd Zobir Hussein; mzobir@upm.edu.my

Received 26 March 2014; Accepted 13 May 2014; Published 23 June 2014

Academic Editor: You Qiang

Copyright © 2014 Bullo Saifullah et al. This is an open access article distributed under the Creative Commons Attribution License, which permits unrestricted use, distribution, and reproduction in any medium, provided the original work is properly cited.

Tuberculosis is a lethal epidemic, difficult to control disease, claiming thousands of lives every year. We have developed a nanodelivery formulation based on para-aminosalicylic acid (PAS) and zinc layered hydroxide using zinc nitrate salt as a precursor. The developed formulation has a fourfold higher efficacy of PAS against mycobacterium tuberculosis with a minimum inhibitory concentration (MIC) found to be at 1.40 $\mu\text{g}/\text{mL}$ compared to the free drug PAS with a MIC of 5.0 $\mu\text{g}/\text{mL}$. The newly developed formulation was also found active against Gram-positive bacteria, Gram-negative bacteria, and *Candida albicans*. The formulation was also found to be biocompatible with human normal lung cells MRC-5 and mouse fibroblast cells-3T3. The *in vitro* release of PAS from the formulation was found to be sustained in a human body simulated phosphate buffer saline (PBS) solution at pH values of 7.4 and 4.8. Most importantly the nanocomposite prepared using zinc nitrate salt was advantageous in terms of yield and free from toxic zinc oxide contamination and had higher biocompatibility compared to one prepared using a zinc oxide precursor. In summary, these promising *in vitro* results are highly encouraging for the continued investigation of para-aminosalicylic acid and zinc layered hydroxide nanocomposites *in vivo* and eventual preclinical studies.

1. Introduction

Tuberculosis (TB) has remained lethal to humans for centuries and is of great public health concern. There were about 1.4 million human deaths from TB and about 8.7 million people infected in 2012 [1, 2]. TB is also the second greatest killer of humans in the world by a single infectious agent after HIV/AIDS [1]. The situation has become even more dire by the reemergence of multidrug resistant TB (MDR-TB) and in

2012, approximately 450,000 people developed MDR-TB and there was about 37% deaths of MDR-TB [1].

Chemotherapy of TB has been complicated by multidrug prescriptions, dosing frequency, longer treatment duration, and adverse side effects associated with anti-TB drugs [3, 4]. Since the drug development is lengthy, costly, and time consuming, it should not be surprising that no new anti-TB drug has reached the market in over 5 decades with the last anti-TB drug approved (rifampicin) in 1963 [3–5]. To cope

with the TB epidemic, there is an urgency to develop new anti-TB formulations which can decrease dosing frequency, shorten treatment time (with little to no side effects), and maintain therapeutic concentrations in the human body for longer periods of time [3–6].

Improved drug delivery systems (DDS) are possibly the best solution for treating TB as they can improve drug bioavailability for longer time periods and release the drug in a sustained local manner to avoid toxicity [4, 7, 8]. DDS could protect the drug from physical, chemical, and enzymatic degradation inside the body and not let the drugs become exposed to the healthy tissues; therefore, they could decrease the side effects associated with the free drug [4, 9]. The DDS can target the diseased site and this can lead to better therapeutic results [8, 9].

Different drug delivery systems have been designed and developed for anti-TB drugs, namely, mesoporous silica nanoparticles, polymeric nanoparticles like poly-n-butyl cyanoacrylate, polyisobutyrylcyanoacrylate, poly(DL-lactide-co-glycolide) inhalable microparticles, large porous microspheres, and so forth [9–14]. But there are certain issues associated with each of these new material systems; some of them are not fully biocompatible, have poor serum solubility, and cause inflammation, cytokine release, cell damage, and so forth [4, 15]. In this manner, we propose a new formulation which should not possess such disadvantages. The layered double hydroxides (LDHs) are inorganic nanolayers with numerous nonbiological applications (such as serving as catalysts, flame retardants, and chiral separation materials) and have also been applied as a safe material for the removal of toxic waste from water [16–19].

Layered double hydroxides (LDHs) have emerged as excellent biocompatible nanocarriers for the sustained release and targeted transport of different pharmaceutical agents [8, 20–23]. LDHs have a structure similar to hydrotalcite with some of the divalent cations replaced with trivalent cations resulting in a positively charged material with brucite-like (magnesium layered hydroxides) sheets stacked over one another layer by layer [24–26]. The positive charge of the LDHs sheets is neutralized by counter anions [25, 27]. Zinc layered hydroxides (ZLH) also have similar characteristics although they do not possess any trivalent cations and anionic intercalation which may possibly be due to the hydrogen bonding between the anions and ZLH. ZLH have been widely applied for the delivery of different pharmaceutical drugs, namely, ellagic acid, hippuric acid, cetirizine, cinnamic acid, *m*-aminobenzoate, 2,4-dichlorophenoxy acetate, and so forth [20, 28–31]. Previously we have developed a sustained release formulation of anti-TB drugs based on para-aminosalicylic acid (PAS) with zinc layered hydroxides using zinc oxide as a starting material [7]. In this effort, we present the development of PAS-ZLH (termed nanocomposite A) using ZnNO_3 salt as the starting material and compare the physicochemical as well as biological properties of such materials to the previously developed formulation using ZnO as the starting material (nanocomposite B) [7].

The nanocomposite-A is free from toxic zinc oxide contamination which is very difficult to avoid using a zinc oxide precursor. The nanocomposite-A (prepared using zinc

nitrate salt) was found to be highly biocompatible compared to the nanocomposite-B (prepared using ZnO). In addition, the yield of the nanocomposite-A was also much higher compared to nanocomposite-B.

2. Materials and Methods

2.1. Materials. Para-aminosalicylic acid, 99% purity, and zinc nitrate hexahydrate were purchased from Sigma-Aldrich. Dimethyl sulfoxide (DMSO) was purchased from Ajax Fine Chem (Sydney, Australia). All of these chemicals were of analytical grade and were used without any further purification. Deionized water was used for all the experimental studies.

2.2. Preparation of Zinc Layer Hydroxides. Zinc nitrate hexahydrate was directly dissolved in 50 mL deionized water and the solution was stirred for 15 minutes under a nitrogen atmosphere. Then, the pH of the solution was increased by the slow addition of a 1 molar sodium hydroxide solution with constant stirring under a nitrogen atmosphere.

2.3. Preparation PAS-ZLH (Termed Nanocomposite-A). A 0.4 mol/L solution (50 mL) of PAS was prepared at a 1 : 1 ratio of DMSO and deionized water and was stirred for 15 minutes. Zinc nitrate hexahydrate, 1 gram dissolved in 50 mL of water, was stirred for another 5 minutes and after that the PAS solution was directly added to this solution. The sample was further stirred for 20 minutes. The pH of the final solution was raised to 7.9 by the dropwise addition of a 1 molar sodium hydroxide solution and then the solution was further stirred for 1 hour. The whole experiment was conducted under continuous nitrogen flow. Finally, the sample was subjected to an oil bath agitation at 70°C for 18 hours. The sample was centrifuged, washed three times, dried at 70°C, and ground to fine powder for further characterization as described below.

2.4. Material Characterization. X-ray diffraction (XRD) analysis was carried out on a Shimadzu (Kyoto, Japan) XRD-6000 Diffractometer. XRD patterns were recorded in the range of $2\theta = 2-60^\circ$, at the $\text{CuK}\alpha$ radiation at 30 kV and 30 mA. Fourier-transform infrared (FTIR) spectra of samples were recorded in the range of 4000–499 cm^{-1} by the direct sample method with a PerkinElmer (Waltham, MA, USA) 100 series spectrophotometer. For the elemental analyses of carbon, hydrogen, nitrogen, and sulfur (CHNS), a LECO (St Joseph, MI, USA) CHNS-932 instrument was utilized. For the thermogravimetric and differential thermogravimetric analyses, a Mettler-Toledo (Greifensee, Switzerland) instrument was used. The sample surface morphology was captured with a JEOL (Tokyo, Japan) JSM-6400 scanning electron microscope (SEM). For optical properties and controlled-release studies, a Shimadzu 1650 series (Japan) UV-Vis spectrophotometer was utilized. The percentage of the PAS loading was determined using a Sykam HPLC system with a Sykam S3250 UV/Vis detector, an auto injector Sykam 5300, and Sykam quaternary pump system 5300 made in Germany, with a column Zorbax Rx-Sil 4.6 × 150 mm, with

5 μm particle sizes (Agilent). For the quantification of the metallic element zinc, an inductively plasma (ICP) optical emission spectrometer (an Optima 2000 DV, Perkin Elmer) was used. Particle size of the nanocomposite was determined with a dynamic light scattering (DLS) technique by using a Zeta sizer nanoseries—NANO-S Malvern instrument.

2.5. Controlled-Release Study. The release behavior of PAS from nanocomposite-A was studied in a human body simulated phosphate buffer solution (0.1 mol/L) at a pH of 7.4 and a pH of 4.8. About 0.3 mg of the nanocomposite was placed in a 3 mL quartz cell and then was placed in a UV/Visible spectrophotometer. The lambda max of PAS (268 nm) was selected for the UV/Vis spectroscopic studies [2].

2.6. Bacteria Studies

2.6.1. Antimicrobial Sensitivity Test. The drug susceptibility test (DST) of nanocomposite-A was determined using a non-radiometric fluorescence-based method of MGIT 960 against *Mycobacterium tuberculosis* (ATCC 25618). The mycobacteria growth indicator tube (MGIT) with a BACTEC MGIT 960 growth supplement for drug susceptibility testing (DST) was used in the MGIT 960 instrument (Becton Dickinson Diagnostic Systems, Sparks, MD, USA) as described previously [32, 33]. The standard protocol for DST in MGIT 960 was strictly followed as recommended for primary drugs. Culture suspensions for inoculation were well dispersed with no large clumps to avoid false-resistant results.

After thorough mixing and homogenization of the culture suspensions, the tubes were allowed to rest for at least 15 min, and the supernatant was used to inoculate the drug-containing media and the control according to the manufacturer's instructions for DST of first-line drugs. All inoculated drug-containing MGIT 960 tubes were placed in the DST set carrier and entered into the MGIT 960 instrument as "unknown drugs" using the DST entry feature. For the DST set containing "unknown drugs," the instrument flagged the DST set "complete" when the growth control reached a growth unit (GU) value of 400. At that point, the GU values of drug-containing tubes were retrieved from the instrument by printing out a DST set report, and results were interpreted manually. If the GU of the drug-containing tube was more than 100 when the GU of the growth control was 400, the results were defined as resistant. If the GU values of the drug-containing tubes were equal to or less than 100, the results were considered susceptible. Experiments were repeated with various concentrations of PAS nanocomposite suspensions until the respective MIC values were determined.

(1) Nonmycobacterium Antimicrobial Susceptibility Testing. The PAS-ZLH (nanocomposite-A) was tested for its antimicrobial activity against different microorganisms including *Staphylococcus aureus* (ATCC 43300), *Pseudomonas aeruginosa* (ATCC 27853), *Escherichia coli* (ATCC 25922), and *Candida albicans* (ATCC 20408) and were purchased from the American Type Culture Collection [ATCC], Manassas,

VA, USA using the standard plate colony counting method. Percentage inhibition of the nanocomposite was plotted as previously described [34].

2.7. Cell Studies

2.7.1. Cell Culture. Human normal lung MRC-5 and mouse fibroblast 3T3 cells were bought from the American Type Culture Collection (ATCC; Manassas, VA, USA), and the cells were cultured in Dulbecco's modified Eagle's medium (DMEM) and RPMI 1640 media containing 10% fetal bovine serum (add the manufacturer information). Growth media contained 100 units/mL of penicillin and 50 $\mu\text{g}/\text{mL}$ of streptomycin. Fibroblasts were maintained at 37°C in a humidified atmosphere in the presence of 5% CO₂.

2.7.2. Assessment of Cytotoxicity by the MTT Assay. Healthy cells were seeded onto 96-well culture plates at 1×10^4 cells per well and were allowed to adhere overnight at 37°C. Then, the cells were incubated with the above medium (100 μL) containing dispersed LDH nanocomposites in various concentration ranges from 0.781 $\mu\text{g}/\text{mL}$ to 50 $\mu\text{g}/\text{mL}$. The control cells were not exposed to the nanocomposites. At specific time points of 24, 48, and 72 hours of incubation, the growth medium was removed from the 96-well plates and incubated with 100 μL of the MTT (3-(4,5-dimethylthiazol-2-yl)-2,5-diphenyltetrazolium bromide) reagent in DMEM for another 3-4 hours at 37°C. The number of viable cells was analyzed by the uptake of MTT and read at 570 nm by an enzyme-linked immunosorbent assay plate reader. Cell viability results were presented as the mean \pm standard deviation.

2.8. Statistical Analysis. Unpaired *t*-tests were used to compare the MICs of PAS and nanocomposite-A against *Mycobacterium tuberculosis*. Statistical analysis was used to compare the percentage inhibition of PAS and nanocomposite-A against different microorganisms using two way-ANOVA tests. The Prism V6.01 statistical software (GraphPad, San Diego, CA, USA) was used for data management and statistical analysis. ANOVA followed by student *t*-tests were used to determine the differences between the means of cell viability (%). All data are shown as the mean \pm standard deviation unless indicated differently.

3. Results and Discussion

3.1. X-Ray Diffraction (XRD) Analysis. Figure 1 shows XRD patterns of the zinc layered hydroxide (ZLH) and PAS-ZLH (nanocomposite-A) materials. In the XRD pattern of the ZLH, there are many small peaks with a first major peak with high intensity at about $2\theta = 9.0^\circ$ with basal spacing of about $d = 10 \text{ \AA}$ (Figure 1), corresponding to nitrate counter anions as due to the reflection of the 200 planes of the monoclinic structure and is also consistent with a previous report [35]. In the XRD pattern of PAS-ZLH (nanocomposite-A), the increase in basal spacing from 10.0 \AA to 26.0 \AA is strong evidence for the successful intercalation of PAS into the interlayer galleries of ZLH (Figure 1).

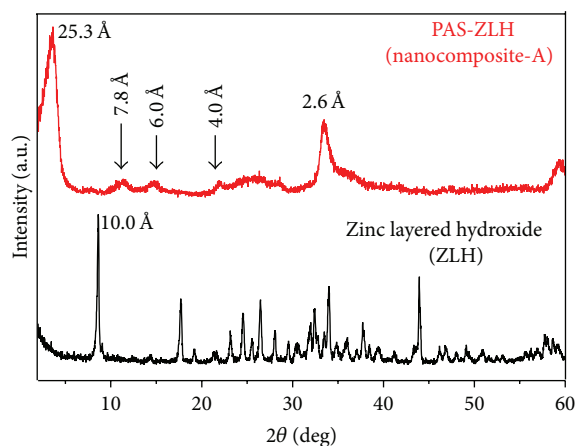


FIGURE 1: X-ray diffraction pattern of zinc layered hydroxide (ZLH) and PAS-ZLH (nanocomposite-A).

In addition to the first reflection (with a d -spacing of 26 Å), PAS-ZLH also showed four more reflections with d -spacing values 7.8 Å, 6.0 Å, and 4.0 Å which indicates the high crystallinity of the nanocomposite. There is a small hump from $2\theta = 22^\circ$ to 28° which can be ascribed to the adsorption of PAS on the ZLH surface, as the area coinciding with XRD peaks of free PAS has prominent peaks in that region, as reported previously [7]. The nanocomposite-B prepared using zinc oxide (ZnO) as a starting material showed five characteristic peaks of ZnO, due to the 100, 002, 101, 102, and 110 planes between 2θ of 30–60, which indicates the presence of unreacted ZnO [7]. However, the current formulation prepared using ZnNO_3 as the starting material did not contain any ZnO. In addition, the yield of the nanocomposite-A was much higher compared to the one using ZnO as the precursor (nanocomposite-B).

3.2. Spatial Orientation of PAS in the Interlayer of ZLH for Nanocomposite A. Based on the 3-D molecular size of PAS, the x , y , and z axes of PAS have been reported to be 9.4 Å, 7.1 Å, and 2.9 Å, respectively [7], and the thickness of the ZLH layer has been reported to be 4.8 Å [35]. The average basal spacing for the nanocomposite-A was found to be 23.6 Å; by subtracting the layer thickness ZLH (4.8 Å), a value of 18.80 Å was obtained. This value of 18.8 Å strongly suggests that PAS has been oriented in a bimolecular vertical form (x -axis) as shown in Figure 2. The PAS-ZLH prepared using ZnO has been reported to have a bimolecular horizontal (y -axis) orientation of PAS into the interlayers of ZLH along with water molecules [7].

3.3. Infrared Spectroscopy. Fourier transform infrared (FTIR) spectroscopy gives information about the presence, absence, and shifting of bands of functional groups and can be very useful in supporting other analytical results. FTIR spectrum of pure PAS showed the characteristic bands for its functional groups at specified positions as carbonyl at 1609 cm^{-1} and symmetric and asymmetric N–H bands at 3381 and 3490 cm^{-1} , respectively; others are given in Table 1 [7]. In

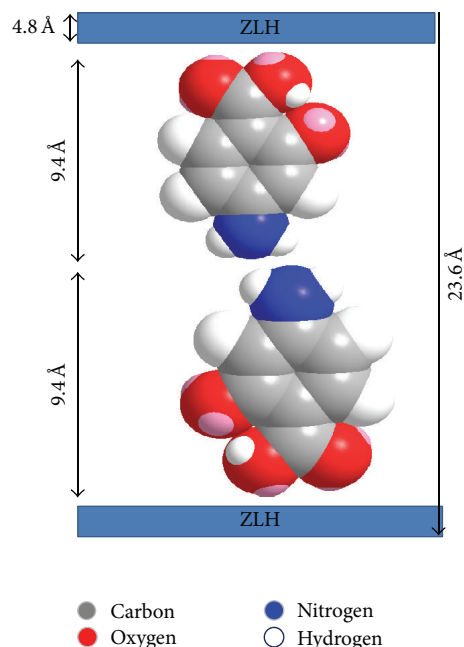


FIGURE 2: Spatial orientation of PAS in interlayers of ZLH (nanocomposite-A).

TABLE 1: FTIR functional group absorption bands of free PAS and its PAS-ZLH (nanocomposite-A).

Assignments	Free PAS	PAS-ZLH
Vas(N–H)	3490	
Vs(N–H)	3381	Overlapped by O–H stretching 3358
V(O–H) in the inter ZnLH, H ₂ O	—	
V(C=O) in COOH	1609, 764	—
VAS(COO–)	—	1551
Vs(COO–)	—	1339
Stretching (C–H)	813, 717	821

Unit for given numbers is wave number (cm^{-1}).

the spectrum of PAS-ZLH (Figure 3), N–H symmetric and asymmetric bands have been overlapped by the O–H band of the interlayer ZLH. In addition, the C=O band of PAS also disappeared instead of the two new bands which appeared at 1551 and 1339 cm^{-1} due to the symmetric and asymmetric bands of carboxylate (COO–), respectively. Most of the other FTIR bands of PAS are present in the nanocomposite-A with slight shifts in wavenumbers and are given in Table 1. The presence of characteristic bands of pure PAS and ZLH in the nanocomposite-A further confirms the XRD result of successful PAS intercalation into ZLH. The FTIR spectrum of the PAS-ZLH nanocomposite-A is similar to the one prepared using the ZnO nanocomposite-B [7].

3.4. HPLC Analysis. HPLC analysis of the active drug PAS in the nanocomposites was carried out by the methods reported by Hong et al. (2011) and Vasbinder et al. (2004) [36, 37]. In

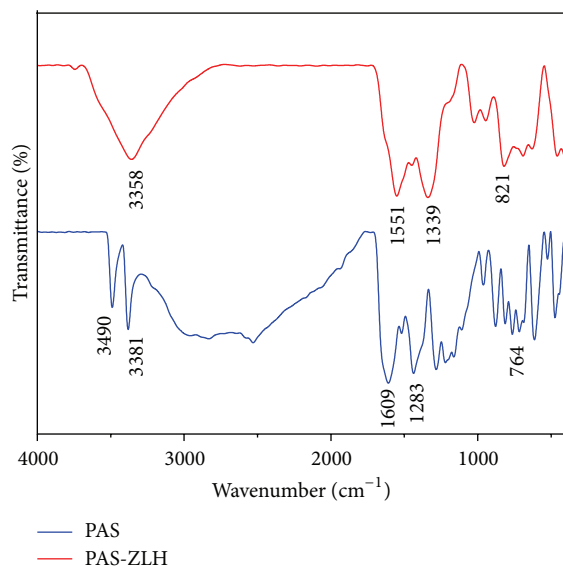


FIGURE 3: FTIR spectrum of PAS-ZLH (nanocomposite-A).

brief, the mobile phase of methanol as solvent A and solvent B phosphate buffer is composed of a 17.5 mM equal amount of monobasic and dibasic potassium phosphate of pH 3.5. The isocratic mobile phase of solvent A and solvent B at a ratio of 60:40 was used with a flow rate of 1 mL/minute. The wavelength of 233 nm was selected for detection using the UV/Vis detector. A calibration curve was obtained by running standards at different concentrations in parts per million (ppm) of PAS (i.e., 0.0 ppm, 20 ppm, 40 ppm, 60 ppm, and 80 ppm) with a good R^2 value of 0.98. Approximately, 10 mg of the nanocomposite was dissolved in 50 mL (5 mL of 1 molar HCl and the remaining volume was composed of the mobile phase) and the standard PAS solutions were also prepared in the same way. The retention time of PAS was found to be 1.8 minutes. The percent loading of PAS in the nanocomposite-A was found to be 22.24%. The loading in the nanocomposite-A (22.42%) was higher as compared to the nanocomposite-B (14.60%) reported previously [7].

3.5. Elemental Analysis. The presence of carbon and nitrogen was determined by CHNS analysis and the metal element zinc was determined by an inductively coupled plasma spectrometer. Elemental analysis of PAS and PAS-ZLH (nanocomposite-B) was taken from our previous report [7]. The presence of organic elements in the samples like carbon, nitrogen (N), and zinc further supported the XRD results for the successful intercalation of PAS into ZLH. The percentage of the each element is given in Table 2.

3.6. Thermogravimetric Analysis. The free drug, PAS, was thermally decomposed at 221°C with a percent mass loss of 67.7%, as reported previously by our group [7]. In the nanocomposite-B, PAS was stabilized and thermal decomposition shifted to 248°C [7]. Figure 4 shows the TGA analysis of the nanocomposite-A prepared by using $ZnNO_3$ instead of ZnO as the starting material. There are three

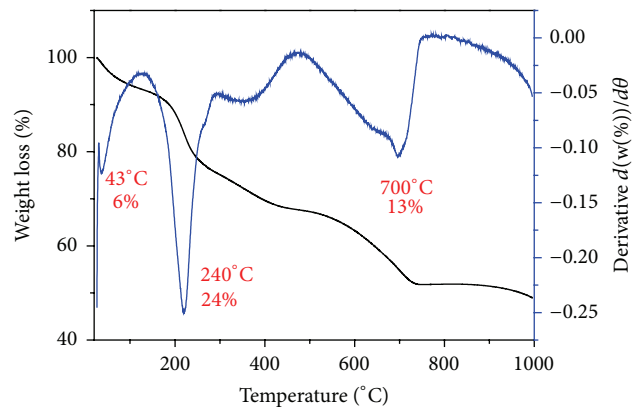


FIGURE 4: Thermogravimetric analysis-differential thermogravimetric thermograms of PAS-ZLH (nanocomposite-A).

main mass loss events that took place for nanocomposite-A. The first event of mass loss of about 6% at 43°C can be attributed to the physically adsorbed water. The second event is the weight loss of 24% at about 240°C, which is due to the thermal decomposition of PAS. PAS has been thermally stabilized from 221°C to about 240°C; the increase in stability can be attributed to the electrostatic interaction between PAS and ZLH. The 3rd event occurred at about 700°C with 13% mass loss, and this can be attributed to the dehydroxylation of ZLH interlayers [20, 29]. The TGA analysis results of nanocomposite-A are almost comparable to the nanocomposite-B reported previously with only slight shifts in temperature and percentage mass loss [7].

3.7. Surface Morphology. Figures 5(a) and 5(b) show the surface morphology of the carrier zinc layered hydroxide (ZLH) with zinc nitrate intercalated. The morphology of ZLH is a 2-dimensional layer type as shown in Figures 5(a) and 5(b). The morphology of the nanocomposite PAS-ZLH is of honey comb type and the sample looks more compact (Figures 5(c) and 5(d)) unlike ZLH alone. The general ZLH have been reported to have plate-like, compact nonuniform agglomerate and rod-like agglomerate like morphology [7, 20, 28]. But for the ZLH nanocomposite this honeycomb morphology is rare; however, it has been reported previously for LDHs nanocomposites by Chen et al. (2012) [38].

3.8. In Vitro Release. Figures 6(a) and 6(b) show the *in vitro* release of PAS from nanocomposite-A in human body simulated phosphate buffer solution (PBS) at pH values of 7.4 and 4.8, respectively. For the initial first 30 minutes, there is faster release of PAS followed by a much more sustained release up to 7000 minutes in PBS at pH 7.4 as shown in Figure 6(a), with an overall release of 94%. Similar trends in release were observed in PBS at pH 4.8, with an overall release of 99%. However, the overall release time was much shorter at pH 4.8 (i.e., 1500 minutes) as compared to PBS at pH 7.4 (i.e., 7000 minutes). The small inset on Figures 6(a) and 6(b) shows the initial release of PAS from the nanocomposite-A. The faster release at pH 4.8 can be ascribed to the different release mechanisms. At lower pH

TABLE 2: Elemental analysis of organic and inorganic elements (nanocomposite-A).

Sample	C (% w/w)	N (% w/w)	C/N	Zn (% w/w)	% Loading of PAS by HPLC
PAS (pure drug)	59.00 ^a	10.00 ^a	6.02 ^a	—	—
PAS-ZLH Nanocomposite-A	16.00 ^a	2.30 ^a	8.20 ^a	44.62 ^b	22.24 ^c
PAS-ZLH Nanocomposite-B	10.54 ^a	1.54 ^a	6.8 ^a	52.7 ^b	14.60 ^c

^a Determined by CHNS analysis; ^b Determined by ICP analysis; ^c Determined by HPLC analysis.

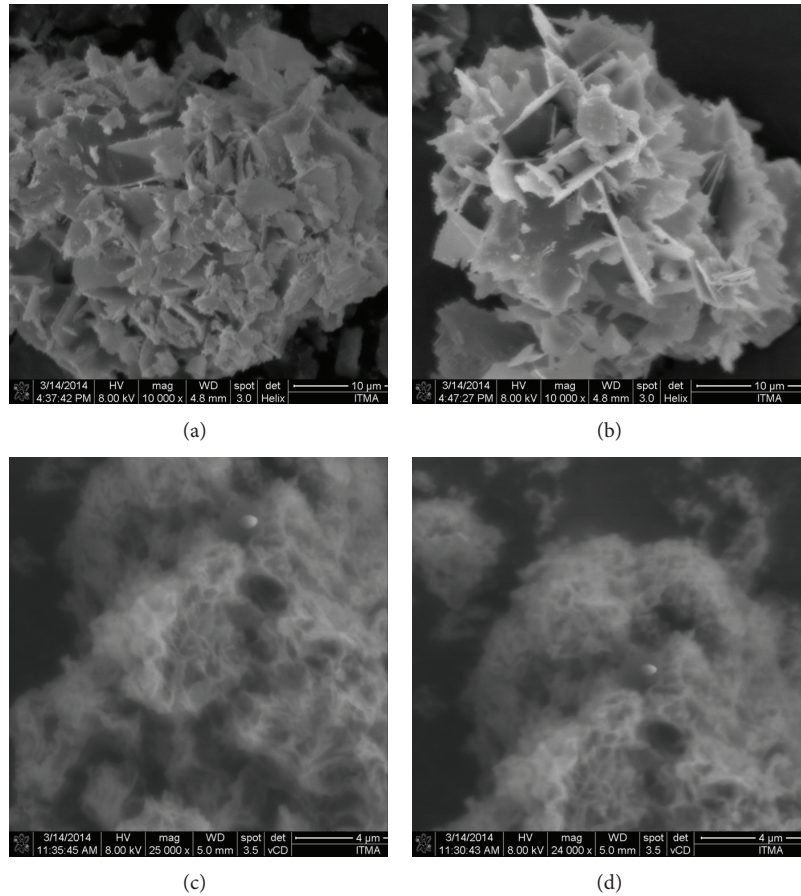


FIGURE 5: FESEM micrographs of ZLH ((a) and (b)) and PAS-ZLH (nanocomposite-A) ((c) and (d)).

values, LDH released the drug by two phenomena, namely, (a) ion exchange and (b) weathering/degradation of the LDH inorganic layers by protonation [8, 39]. At the higher pH 7.4, the drug was released by ion exchange mechanisms only and not by weathering [8, 39]. These release trends of nanocomposite-A are similar to the nanocomposite-B as reported previously by us [7].

3.9. Release Kinetics of PAS from Nanocomposite-A. Three different kinetic models, namely, pseudo-first order, pseudo-second order, and parabolic diffusion kinetic equations, were applied to analyze the release kinetics of PAS. The model equations applied are described in standard form as below.

The pseudo-first order kinetic equation in the linear form can be described as

$$\ln q_e - q_t = \ln q_e - K_1 t, \quad (1)$$

where q_e is the amount released in equilibrium and q_t is amount released at time (t). K_1 is the constant whose value can be determined from the slope by plotting $\ln(q_e - q_t)$ against t [40, 41].

The pseudo-second order equation is given below in its linear form [26, 42]:

$$\frac{t}{q_t} = \frac{1}{K_2 q_e^2} + \frac{t}{q_e}. \quad (2)$$

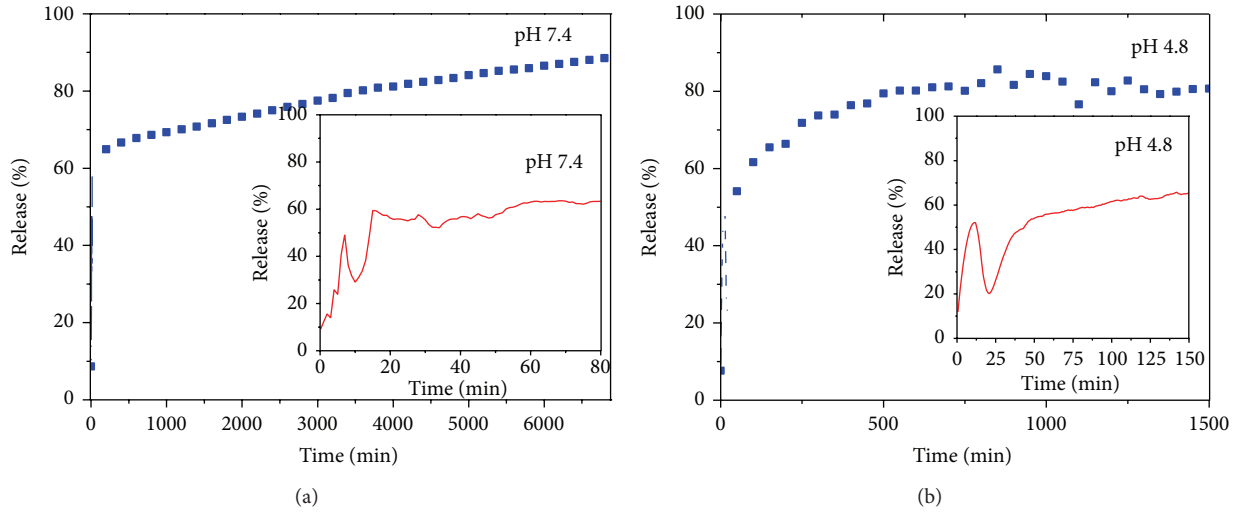


FIGURE 6: (a) *In vitro* release of PAS from PAS-ZLH (nanocomposite-A) in human body simulated phosphate buffer solutions of pH 7.4. (b) *In vitro* release of PAS from PAS-ZLH (nanocomposite A) in human body simulated phosphate buffer solutions of pH 4.8.

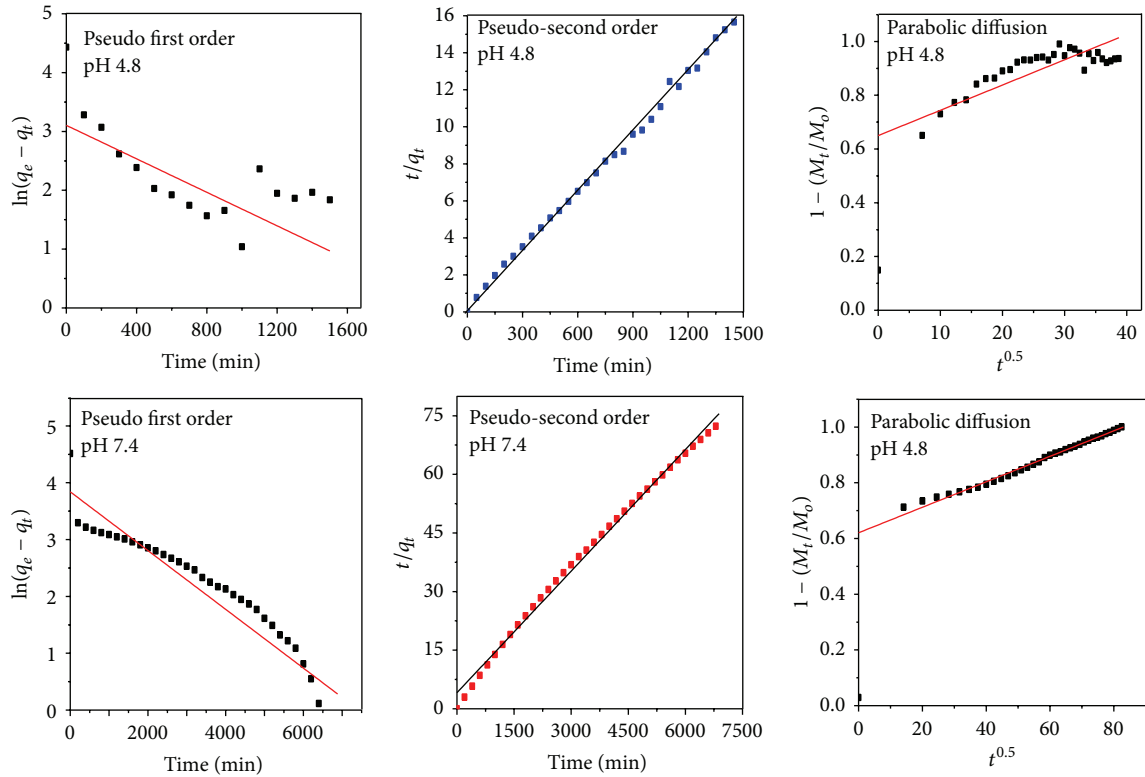


FIGURE 7: Kinetic fitting data for PAS *in vitro* release from PAS-ZLH (nanocomposite A) into PBS solutions at pH 7.4 and 4.8 by applying the pseudo-first and pseudo-second-order kinetics and parabolic diffusion model.

The standard parabolic equation can be described as follows:

$$\left(\frac{1 - (M/M_o)}{t} \right) = k_t^{-0.5} + b, \quad (3)$$

where M_o and M_t represent the amount of drug that remained in ZLH at release time 0 and at time t , respectively, and b is a constant [26, 43].

By applying the above three kinetic equations, we found that the release kinetics of PAS followed the pseudo-second order as the value of the correlation coefficient R^2 was greater than that for the other two equations both at pH 4.8 and pH

TABLE 3: Rate constant (k) and correlation coefficient R^2 determined from the release kinetics of PAS from PAS-ZLH (nanocomposite-A) into PBS solutions of pH 7.4 and pH 4.8.

Samples	pH	Release/%	R^2			Pseudo-second order
			Pseudo-first order	Pseudo-second order	Parabolic diffusion model	Rate constant K_2 (mg/min)
Nanocomposite-A						
PAS-ZLLH	4.8	99	0.56	0.99	0.66	2.85×10^{-4}
PAS-ZLLH	7.4	94	0.81	0.99	0.95	2.70×10^{-5}

Of PAS are similar to the nanocomposite-B as reported previously by us [7].

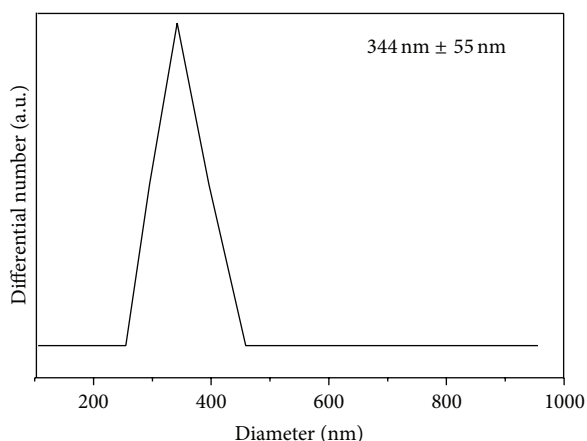


FIGURE 8: Hydrodynamic size of the PAS-ZLH nanocomposite-A.

7.4, as given in Table 3. Table 3 also contains the rate constant value for the pseudo second-order model PAS release kinetics at pH 4.8 and 7.4. Figure 7 represents fitting plots for the release kinetics of PAS released from nanocomposite-A at pH 4.8 and 7.4 obtained by applying all these three different kinetic models. We can clearly observe a straight line that is only obtained in the pseudo-second order model, which further suggests that the release kinetics follow the pseudo-second order route.

The pseudo-second-order release kinetics is actually a third order reaction which means the PAS release depends on the three things. Here, it can possibly be the concentration of the nanocomposite, the concentration anions present in PBS (i.e., HPO_4^{-2}), and the PBS medium environment.

3.10. Particle Size Analysis. The average hydrodynamic size of the PAS-ZLH (nanocomposite A) was determined by using dynamic light scattering (DLS) by using a zeta sizer. The sample was dispersed in deionized water and sonicated for 15 minutes. In order to get more accurate results, samples were measured three times. The average diameter of the nanocomposite-A was found to be $344 \text{ nm} \pm 55 \text{ nm}$ as the DLS graph shows in Figure 8.

3.11. Antimycobacterial and Antimicrobial Assays. The MIC of the PAS-ZLH (nanocomposite A) against *Mycobacterium tuberculosis* was found to be $6.1 \mu\text{g/mL}$ as compared to that of the free drug (PAS) which was $5.0 \mu\text{g/mL}$ as shown in Figure 9. The effective MIC concentration of the drug PAS

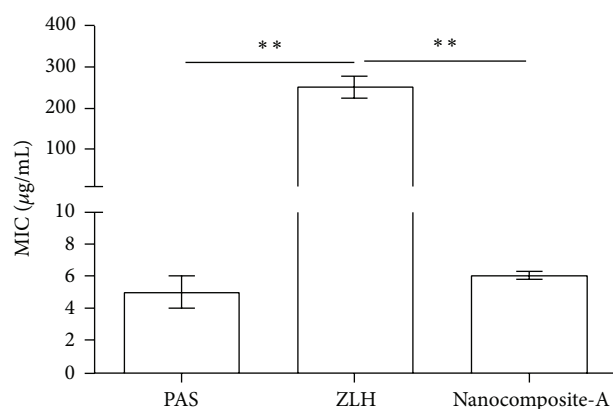


FIGURE 9: Minimum inhibitory concentrations ($\mu\text{g/mL}$) (MICs) of PAS-ZLH (Nanocomposite A) as compared to PAS against *Mycobacterium tuberculosis* determined by the mycobacteria growth indicator tube (MGIT) with BACTEC MGIT 960 growth supplement for drug susceptibility testing (DST) and measured by the MGIT 960 instrument (Becton Dickinson Diagnostic Systems, Sparks, MD, USA).

in nanocomposite-A based on loading 22.42% is $1.40 \mu\text{g/mL}$ which is about 4 times less than free drug PAS with an MIC of $5.0 \mu\text{g/mL}$. Based on this effective MIC concentration we can see the efficacy of PAS is fourfold higher when given in nanocomposite form compared to that given as free PAS. This improved efficacy of PAS in PAS-ZLH (nanocomposite A) can be attributed the nanoscale size and sustained release of PAS for longer periods time. The results of the antimicrobial testing found that the nanocomposite-A showed antibacterial activity against Gram-positive and Gram-negative bacteria and *Candida* as shown in Figures 10(a) and 10(b) from the percentage inhibition of each compound against different organisms. It was found that the nanocomposite was more active against Gram-positive (*Staphylococcus aureus*) and Gram-negative (*E. coli*) bacteria than *Pseudomonas aeruginosa* and *Candida albicans*.

3.12. Cytotoxic Study

3.12.1. Cytotoxic Study of the Nanocomposite-A against Mouse Fibroblast Cells 3T3. Cytocompatibility of the nanocomposites was determined using a colorimetric method by the MTT assay. Figure 11 shows the MTT assay results obtained using various concentrations ($0.78 \mu\text{g/mL}$ to $50 \mu\text{g/mL}$ of the nanocomposite-A) against mouse fibroblast 3T3 cells for different period of times, that is, 24, 48, and 72 hours.

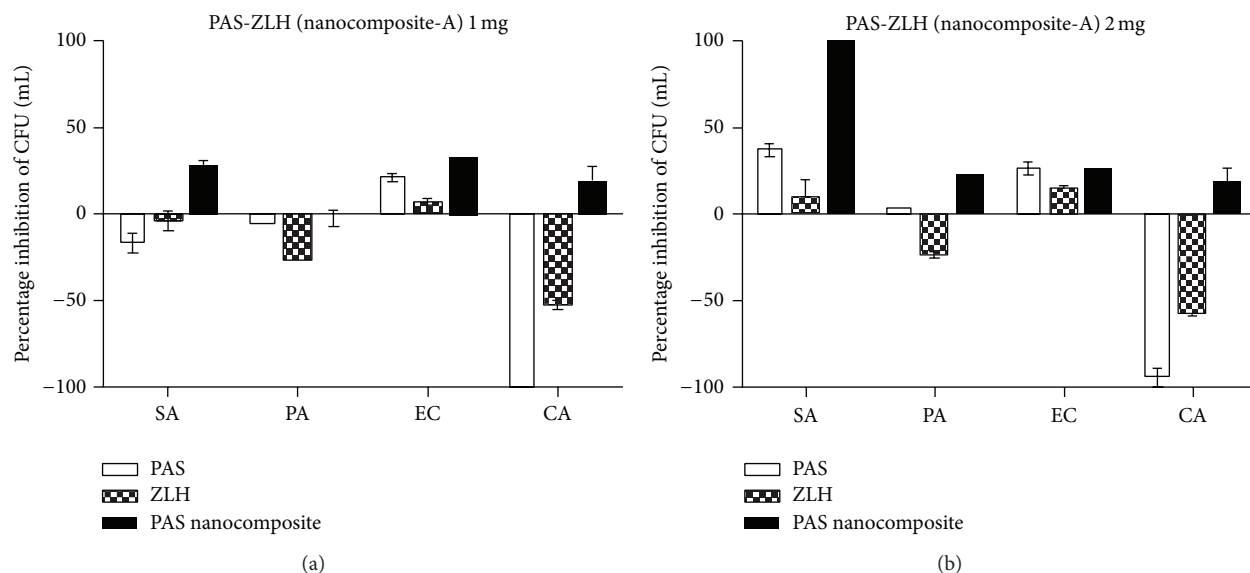


FIGURE 10: Effect of PAS-ZLH (nanocomposite-A) on the inhibition of microbial growth using the plate colony counting method at two concentrations ((a): 1 mg) and ((b): 2 mg). CFU: colony-forming units; SA: *Staphylococcus aureus*; PA: *Pseudomonas aeruginosa*; EC: *E. coli*; CA: *Candida albicans*.

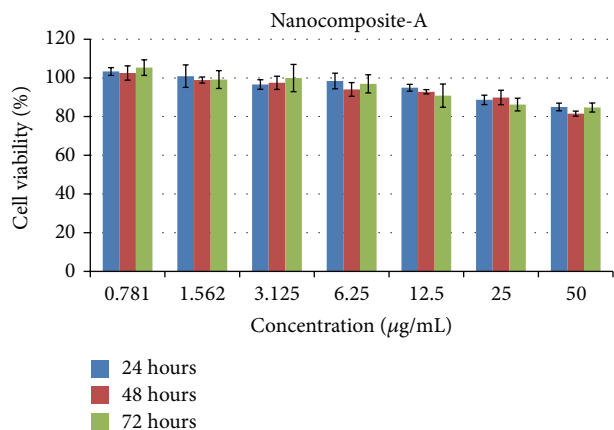


FIGURE 11: PAS-ZLH (nanocomposite-A) against mouse fibroblast cells 3T3.

The percent cell viability of nanocomposite-A was found to be very high, about 85% even at the highest concentration 50 µg/mL for the longest duration of 72 hours. In comparison to nanocomposite-A, nanocomposite-B was reported to be biocompatible until 25 µg/mL was added only for 24 hours and for 48 and 72 hours, 25 µg/mL was biocompatible with about 80% cell viability [7]. However, at higher concentrations of 50 µg/mL, nanocomposite-B was found to be cytotoxic as reported earlier [7]. Thus, we conclude that nanocomposite-A has higher biocompatibility compared to nanocomposite-B, even at higher concentrations for 72 hours using mouse fibroblast cells.

3.12.2. Cytotoxic Study of Nanocomposite-A and Carrier Zinc Layered Hydroxide (ZLH) against Human Normal Lung Cells

MRC-5. The most common form of TB is called pulmonary TB, where the bacteria reside in the lungs [44]. It is highly advisable for any new anti-TB formulation that its biocompatibility should be assayed against human lung cells. We conducted a cytotoxic study of the developed nanocomposite-A and the carrier ZLH against human normal lung cells, MRC-5. In order to check the biocompatibility, the MTT assay protocol was followed and different concentrations of the nanocomposites-A and ZLH ranging from 0.78 µg/mL to 50 µg/mL were treated against human normal lung cells MRC-5 for 24, 48, and 72 hours as shown in Figures 12(a)–12(c). The carrier, ZLH, itself was found to be toxic which may be due the presence of nitrate anions which are present as counter anions. However, nanocomposite-A was found to be highly biocompatible with cell viability at about 80% at the highest concentration of 50 µg/mL for the longest treatment duration of 72 hours.

4. Conclusions

The present study describes the development of an antituberculosis nanodelivery formulation based on para-amino salicylic acid with zinc layered hydroxides using ZnNO₃ salt as a precursor.

The PAS *in vitro* efficacy was found to be fourfold better when used in the developed formulation compared to the free drug PAS. The formulation was also found active against Gram-positive bacteria, Gram-negative bacteria, and *Candida*. The PAS-ZLH showed very good biocompatibility with human normal lung cells and MRC-5 as well as with mouse fibroblast 3T3 cells. Furthermore, the *in vitro* release study of PAS from the interlayer galleries ZLH was found to be sustained in human body simulated phosphate buffer saline solutions of pH 7.4 and 4.8. In comparison to the

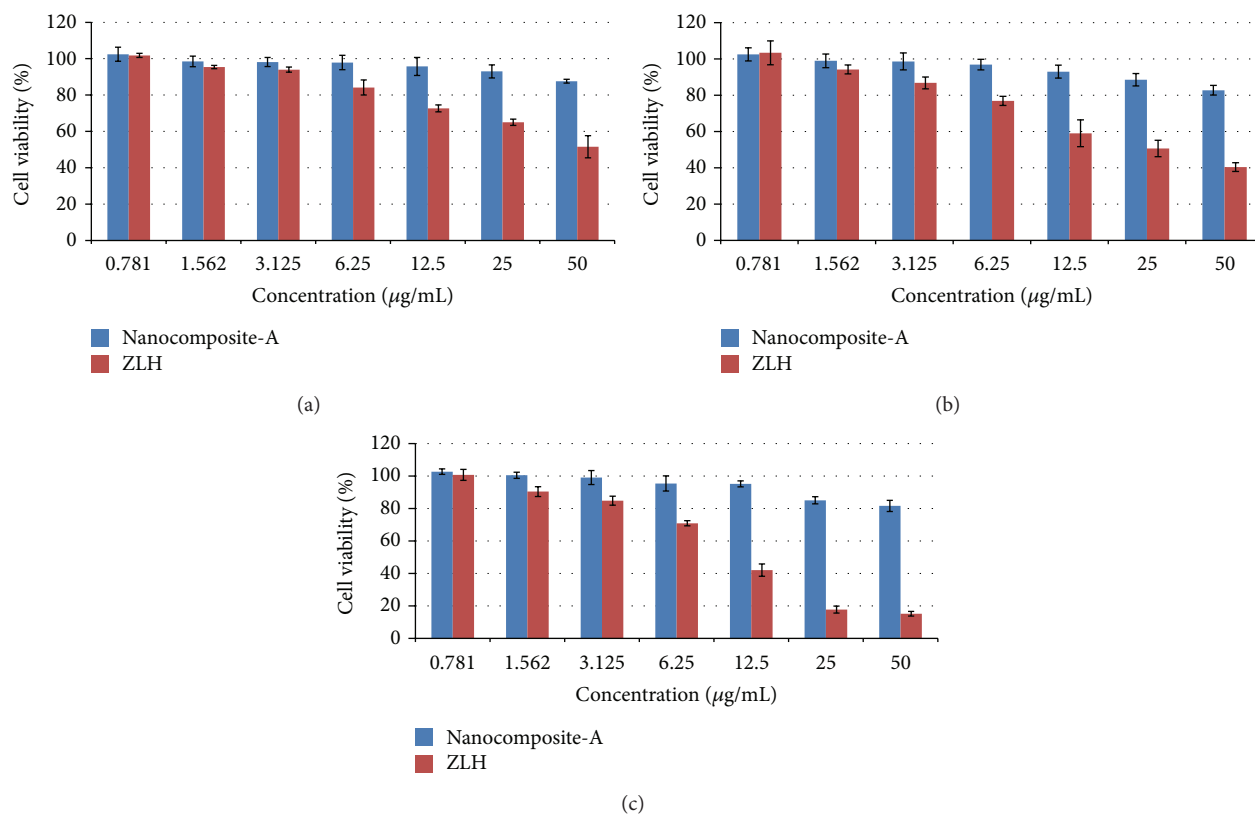


FIGURE 12: (a) 24-hour lung cells MRC-5 PAS-ZLH (nanocomposite A) and the carrier ZLH. (b) 48-hour lung cells MRC-5 PAS-ZLH (nanocomposite-A) and the carrier ZLH. (c) 72-hour lung cells MRC-5 PAS-ZLH (nanocomposite-A) and the carrier ZLH.

previous PAS-ZLH, prepared using ZnO as the starting material, the current formulation gave better yield, loading, and biocompatibility properties. In summary, these promising *in vitro* results are highly encouraging for the continued investigation of para-aminosalicylic acid and zinc layered hydroxide nanocomposites *in vivo* and eventual preclinical studies.

Conflict of Interests

The authors declare that there is no conflict of interest regarding the publication of this paper.

Acknowledgments

The authors would like to thank the Ministry of Education (MOE) for Fundamental Research Grant Scheme and for the scholarship to Bullo Saifullah and Northeastern University, Boston, Massachusetts, USA, for anti-TB testing. Funding for this research was provided by the Higher Education Commission of Malaysia under the Commonwealth Scholarship and Fellowship Plan (Ref: KPT.B.600-6/3, Vol. 68), to Bullo Saifullah; Fundamental Research Grant Scheme (FRGS), FRGS/2/2013/SG06/UPM/01/1 with vote number 5524467, to Mohd Zobir Hussein; Northeastern University, Boston, MA, USA, for funding the anti-TB experiments for Thomas J. Webster.

References

- [1] World Health Organization, Global Tuberculosis Report, 2013, http://apps.who.int/iris/bitstream/10665/91355/1/9789241564656_eng.pdf.
- [2] E. Vasbinder, G. van der Weken, Y. Vander Heyden et al., "Quantitative determination of para-aminosalicylic acid and its degradation product meta-aminophenol in pellets by ion-pair high-performance liquid chromatography applying the monolithic Chromolith Speedrod RP-18e column," *Biomedical Chromatography*, vol. 18, no. 1, pp. 55–63, 2004.
- [3] A. Koul, E. Arnoult, N. Lounis, J. Guillemont, and K. Andries, "The challenge of new drug discovery for tuberculosis," *Nature*, vol. 469, no. 7331, pp. 483–490, 2011.
- [4] B. Saifullah, M. Z. Hussein, and S. H. Hussein-Al-Ali, "Controlled-release approaches towards the chemotherapy of tuberculosis," *International Journal of Nanomedicine*, vol. 7, pp. 5451–5463, 2012.
- [5] B. Villemagne, C. Crauste, M. Flipo, A. R. Baulard, B. Déprez, and N. Willand, "Tuberculosis: the drug development pipeline at a glance," *European Journal of Medicinal Chemistry*, vol. 51, pp. 1–16, 2012.
- [6] A. Shehzad, G. Rehman, M. Ul-Islam, W. A. Khattak, and Y. S. Lee, "Challenges in the development of drugs for the treatment of tuberculosis," *The Brazilian Journal of Infectious Diseases*, vol. 17, no. 1, pp. 74–81, 2013.

- [7] B. Saifullah, M. Z. Hussein, S. H. Hussein-Al-Ali, P. Arulselvan, and S. Fakurazi, "Sustained release formulation of an anti-tuberculosis drug based on para-aminosalicylic acid-zinc layered hydroxide nanocomposite," *Chemistry Central Journal*, vol. 7, no. 1, article 72, 2013.
- [8] A. U. Kura, S. H. Hussein-Al-Ali, M. Z. Hussein, S. Fakurazi, and P. Arulselvan, "Development of a controlled-release anti-parkinsonian nanodelivery system using levodopa as the active agent," *International Journal of Nanomedicine*, vol. 8, pp. 1103–1110, 2013.
- [9] D. L. Clemens, B. Y. Lee, M. Xue et al., "Targeted intracellular delivery of antituberculosis drugs to *Mycobacterium tuberculosis*-infected macrophages via functionalized mesoporous silica nanoparticles," *Antimicrobial Agents and Chemotherapy*, vol. 56, no. 5, pp. 2535–2545, 2012.
- [10] Y. V. Anisimova, S. I. Gelperina, C. A. Peloquin, and L. B. Heifets, "Nanoparticles as antituberculosis drugs carriers: effect on activity against *Mycobacterium tuberculosis* in human monocyte-derived macrophages," *Journal of Nanoparticle Research*, vol. 2, no. 2, pp. 165–171, 2000.
- [11] M. J. Alonso, C. Losa, P. Calvo, and J. L. Vila-Jato, "Approaches to improve the association of amikacin sulphate to poly (alkylcyanoacrylate) nanoparticles," *International Journal of Pharmaceutics*, vol. 68, no. 1–3, pp. 69–76, 1991.
- [12] R. Sharma, D. Saxena, A. K. Dwivedi, and A. Misra, "Inhalable microparticles containing drug combinations to target alveolar macrophages for treatment of pulmonary tuberculosis," *Pharmaceutical Research*, vol. 18, no. 10, pp. 1405–1410, 2001.
- [13] S. Giovagnoli, P. Blasi, A. Schoubben, C. Rossi, and M. Ricci, "Preparation of large porous biodegradable microspheres by using a simple double-emulsion method for capreomycin sulfate pulmonary delivery," *International Journal of Pharmaceutics*, vol. 333, no. 1–2, pp. 103–111, 2007.
- [14] M. Dutt and G. K. Khuller, "Sustained release of isoniazid from a single injectable dose of poly (DL-lactide-co-glycolide) microparticles as a therapeutic approach towards tuberculosis," *International Journal of Antimicrobial Agents*, vol. 17, no. 2, pp. 115–122, 2001.
- [15] B. Saifullah, M. Z. Hussein, S. H. Hussein-Al-Ali, P. Arulselvan, and S. Fakurazi, "Antituberculosis nanodelivery system with controlled-release properties based on para-amino salicylate-zinc aluminum-layered double-hydroxide nanocomposites," *Drug Design, Development and Therapy*, vol. 7, pp. 1365–1375, 2013.
- [16] P. Koilraj, R. S. Thakur, and K. Srinivasan, "Solid state structural transformation of tetraborate into monoborate in the interlayer galleries of reconstructed ZnAl layered double hydroxide," *Journal of Physical Chemistry C*, vol. 117, no. 13, pp. 6578–6586, 2013.
- [17] S. Kuhl, M. Friedrich, M. Armbruster, and M. Behrens, "Cu,Zn,Al layered double hydroxides as precursors for copper catalysts in methanol steam reforming—PH-controlled synthesis by microemulsion technique," *Journal of Materials Chemistry*, vol. 22, no. 19, pp. 9632–9638, 2012.
- [18] D. Y. Wang, A. Das, A. Leuteritz et al., "Structural characteristics and flammability of fire retarding EPDM/layered double hydroxide (LDH) nanocomposites," *RSC Advances*, vol. 2, no. 9, pp. 3927–3933, 2012.
- [19] Z. Fu, Y. Xie, X. Chen, F. Jiao, and L. Liu, "Preparation and characteristic of chiral separation reagent pillared Zn-Al hydrotalcite-like compound," *Materials Review*, vol. S2, 2010.
- [20] S. M. N. Mohsin, M. Z. Hussein, S. H. Sarijo, S. Fakurazi, P. Arulselvan, and T. Y. Hin, "Synthesis of (cinnamate-zinc layered hydroxide) intercalation compound for sunscreen application," *Chemistry Central Journal*, vol. 7, no. 1, article 26, 2013.
- [21] F. Barahuie, M. Z. Hussein, S. H. Hussein-Al-Ali, P. Arulselvan, S. Fakurazi, and Z. Zainal, "Preparation and controlled-release studies of a protocatechuic acid-magnesium/aluminum layered double hydroxide nanocomposite," *International Journal of Nanomedicine*, vol. 8, pp. 1975–1987, 2013.
- [22] C. Del Hoyo, "Layered double hydroxides and human health: an overview," *Applied Clay Science*, vol. 36, no. 1–3, pp. 103–121, 2007.
- [23] S. H. Hussein-Al-Ali, M. Al-Qubaisi, M. Z. Hussein, M. Ismail, Z. Zainal, and M. N. Hakim, "In vitro inhibition of histamine release behavior of cetirizine intercalated into zn/al- and mg/al-layered double hydroxides," *International Journal of Molecular Sciences*, vol. 13, no. 5, pp. 5899–5916, 2012.
- [24] X. E. Duan and D. G. Evans, Eds., *Layered Double Hydroxides*, vol. 119 of *Structure and Bonding*, Springer, Berlin, Germany, 2006.
- [25] V. Angelo, "Layered double hydroxides: present and future: V. Rives (Ed.), Nova Science Publishers, Inc., New York, 2001, IX+439 pp., ISBN 1-59033-060-9," *Applied Clay Science*, vol. 22, no. 1–2, pp. 75–76, 2002.
- [26] V. Rives, M. del Arco, and C. Martin, "Intercalation of drugs in layered double hydroxides and their controlled release: a review," *Applied Clay Science*, vol. 88–89, pp. 239–269, 2014.
- [27] V. Rives, *Layered Double Hydroxides: Present and Future*, Nova Science, 2001.
- [28] M. Z. Hussein, S. H. Hussein-Al-Ali, Z. Zainal, and M. N. Hakim, "Development of antiproliferative nanohybrid compound with controlled release property using ellagic acid as the active agent," *International Journal of Nanomedicine*, vol. 6, no. 1, pp. 1373–1383, 2011.
- [29] S. H. Hussein-Al-Ali, M. Al-Qubaisi, M. Z. Hussein, Z. Zainal, and M. N. Hakim, "Preparation of hippurate-zinc layered hydroxide nanohybrid and its synergistic effect with tamoxifen on HepG2 cell lines," *International Journal of Nanomedicine*, vol. 6, no. 1, pp. 3099–3111, 2011.
- [30] L. Zhao, H. Wang, Y. Wang, J. Miao, and Q. Feng, "Synthesis of layered hydroxide zinc m-aminobenzoate compounds and their exfoliation reactions," *Chinese Journal of Chemistry*, vol. 29, no. 9, pp. 1837–1845, 2011.
- [31] A. M. Bashi, M. Z. Hussein, Z. Zainal, and D. Tichit, "Synthesis and controlled release properties of 2,4-dichlorophenoxy acetate-zinc layered hydroxide nanohybrid," *Journal of Solid State Chemistry*, vol. 203, pp. 19–24, 2013.
- [32] S. B. Walters and B. A. Hanna, "Testing of susceptibility of *Mycobacterium tuberculosis* to isoniazid and rifampin by mycobacterium growth indicator tube method," *Journal of Clinical Microbiology*, vol. 34, no. 6, pp. 1565–1567, 1996.
- [33] M. Palaci, S. Y. Ueki, D. N. Sato, M. A. da Silva Telles, M. Curcio, and E. A. Silva, "Evaluation of mycobacteria growth indicator tube for recovery and drug susceptibility testing of *Mycobacterium tuberculosis* isolates from respiratory specimens," *Journal of Clinical Microbiology*, vol. 34, no. 3, pp. 762–764, 1996.
- [34] M. S. Usman, M. E. El Zowalaty, K. Shamel, N. Zainuddin, M. Salama, and N. A. Ibrahim, "Synthesis, characterization, and antimicrobial properties of copper nanoparticles," *International Journal of Nanomedicine*, vol. 8, pp. 4467–4479, 2013.

- [35] S. P. Newman and W. Jones, "Comparative study of some layered hydroxide salts containing exchangeable interlayer anions," *Journal of Solid State Chemistry*, vol. 148, no. 1, pp. 26–40, 1999.
- [36] L. Hong, W. Jiang, W. Zheng, and S. Zeng, "HPLC analysis of para-aminosalicylic acid and its metabolite in plasma, cerebrospinal fluid and brain tissues," *Journal of Pharmaceutical and Biomedical Analysis*, vol. 54, no. 5, pp. 1101–1109, 2011.
- [37] E. Vasbinder, G. van der Weken, Y. Vander Heyden et al., "Quantitative determination of p-aminosalicylic acid and its degradation product m-aminophenol in pellets by ion-pair high-performance liquid chromatography applying the monolithic Chromolith Speedrod RP-18e column," *Biomedical Chromatography*, vol. 18, no. 1, pp. 55–63, 2004.
- [38] X. T. Chen, F. Mi, H. Zhang, and H. Q. Zhang, "Facile synthesis of a novel magnetic core-shell hierarchical composite submicrospheres $\text{Fe}_3\text{O}_4@\text{CuNiAl-LDH}$ under ambient conditions," *Materials Letters*, vol. 69, pp. 48–51, 2012.
- [39] M. L. Parelo, R. Rojas, and C. E. Giacomelli, "Dissolution kinetics and mechanism of Mg-Al layered double hydroxides: a simple approach to describe drug release in acid media," *Journal of Colloid and Interface Science*, vol. 351, no. 1, pp. 134–139, 2010.
- [40] L. Dong, L. Yan, W. G. Hou, and S. Liu, "Synthesis and release behavior of composites of camptothecin and layered double hydroxide," *Journal of Solid State Chemistry*, vol. 183, no. 8, pp. 1811–1816, 2010.
- [41] M. Wang, Q. Hu, D. Liang et al., "Intercalation of Galicylidene-amino acid Schiff base complexes into layered double hydroxides: synthesis, characterization, acid resistant property, *in vitro* release kinetics and antimicrobial activity," *Applied Clay Science*, vol. 83-84, pp. 182–190, 2013.
- [42] Y. S. Ho and A. E. Ofomaja, "Pseudo-second-order model for lead ion sorption from aqueous solutions onto palm kernel fiber," *Journal of Hazardous Materials*, vol. 129, no. 1–3, pp. 137–142, 2006.
- [43] X. Kong, S. Shi, J. Han, F. Zhu, M. Wei, and X. Duan, "Preparation of Glycy-l-Tyrosine intercalated layered double hydroxide film and its *in vitro* release behavior," *Chemical Engineering Journal*, vol. 157, no. 2-3, pp. 598–604, 2010.
- [44] A. I. Yousef, M. F. Ismael, A. E. Elshora, and H. E. Abdou, "Pulmonary tuberculosis in patients with chronic renal failure at Zagazig University Hospitals," *Egyptian Journal of Chest Diseases and Tuberculosis*, vol. 63, no. 1, pp. 187–192, 2014.